Magnetic nanoparticles as potential contrast agents in Magnetic Resonance Imaging

Sofia Caspani
Medical Physics
Department of Physics and Astronomy
2019

Supervisor
Prof. Dra. Célia Sousa, Faculdade de Ciências

Co-supervisor
Prof. Dr. João Pedro Esteves de Araújo, Faculdade de Ciências

Todas as correções determinadas pelo júri, e só essas, foram efetuadas.

O Presidente do Júri,

Porto, _____/_____/_____

''A man must cling to the belief that the incomprehensible is comprehensible; otherwise he would not try to fathom it.''

JOHANN WOLFGANG VON GOETHE

Acknowledgments

This work would have been much harder without the support of all the beautiful people that have accompanied me towards another finishing line. Firstly, I would like to thank my Supervisor, professor Célia Sousa, for all the guiding lines, inspiration, trust, continuous support and help provided along this year. Likewise, a special thanks to Suellen Moraes to have kept an eye on me along this way, from the beginning to the end, and enriched me with her precious advises.

In the same way, I would like to thank Dra. Diana Leitão and hers phD students, and Dra. Ana Silva, from INESC-MN for all the kindness, given opportunities and support.

I am grateful to everyone that have helped me at IFIMUP and provided to put a smile on my face even in the most difficult times.

On a more personal note, an enormous thanks to my family that, even if not physically present, have always gave me the strength to be positive and to follow my dreams. To my portuguese family, especially Flávia, Tomás and Pedro, to the already existing friendships and to the ones built up along this way, I am grateful.

A special thanks to my mom, for everything.

UNIVERSIDADE DO PORTO

Abstract

Faculdade de Ciências
Departamento de Física e Astronomia

Master of Science

Magnetic nanoparticles as potential contrast agents in Magnetic Resonance Imaging

by Sofia CASPANI

The advance in synthesis methods and the research of new magnetic effects have been the driving forces that propel magnetic nanostructures to be used in several biotechnological fields. Magnetic Resonance Imaging (MRI) is a powerful, non-invasive and non-destructive imaging tool, capable of providing 3D internal images of living organisms. Magnetic contrast agents have allowed clinical researchers and analysts to enormously increase the sensitivity levels within tissues in a living body. Recently, it has been presented, in literature, an alternative approach to overcome the main limitations of currently used Superparamagnetic Nanoparticles (SP-NPs), restricted to the superparamagnetic regime, based on Synthetic Antiferromagnetic Nanoparticles (SAF-NPs). SAF-NPs, due to their low coercivity and remanence values and higher saturation field when compared to SP-NPs, have been considered good candidates as contrast enhancing agents for MRI. The potential biomedical applications of SAFs are here reviewed, from the antiferromagnetic coupling phenomena to the main used materials and nanoarchitetures.

SAF nanostructures have been fabricated by using two different experimental routes: ‘top-down’ and ‘bottom-up’, for nanodiscs and segmented nanowires (NWs), respectively.

Through the top-down approach, batches of stacks with different materials have been fabricated either by ion beam deposition (IBD) and magnetron sputtering, exploring, for

each ensemble of samples, a wide range of spacer thicknesses. The batches have been magnetically characterized by using a vibrating sample magnetometer (VSM) to achieve the desired magnetic behaviour. The antiferromagnetic coupling has been found either between two CoFe ferromagnetic layers or CoFeB ones, for a specific Ru thickness. Thus, CoFe-based nanodiscs with dimensions of about 600 nm have been fabricated by magnetron sputtering deposition on a Si pre-patterned substrate by Interference Lithography. The discs have been fully characterized with scanning electron microscopy (SEM), X-ray diffraction (XRD), VSM and MOKE. SAF nanodiscs have been obtained with potential application in MRI.

Magnetic nanowires (NWs) of 130 nm-diameter and different lengths have been then electrodeposited in porous anodic alumina (PAA) templates, as can also be used as contrast agents in MRI. The obtained segmented Au/Fe NWs have been characterized by SEM and XRD, and the behaviour of the current density during electrodeposition process have been analysed to understand their morphology. The magnetic properties have been accessed by using a superconductive quantum interference device (SQUID). Ferromagnetic nanowires have been obtained with tuneable magnetic response depending on the Fe and Ay interlayer thickness.

Key words: magnetic nanostructures, superparamagnetic nanoparticles, synthetic antiferromagnetic nanoparticles, vortex-state nanodiscs, magnetic nanowires, tuneable magnetic properties, zero remanence field, coercivity, nanomedicine, biomedicine, magnetic resonance imaging, contrast enhancing agents, relaxivity, magnetic fluid hyperthermia, cell separation, laser interference lithography, physical vapour deposition, ion beam deposition, magnetron sputtering, porous anodic alumina templates, electropolish, anodization, electrodeposition, scanning electron microscopy, x-ray diffraction, vibrating sample magnetometer, superconductive quantum interference device, magneto optic kerr effect.

Contents

Acknowledgments **v**

Abstract **vii**

Contents **ix**

List of tables **xi**

List of figures **xiii**

Abbreviations **xvii**

1. Introduction **1**

1.1 Magnetic nanoparticles and their biomedical applications 1
1.1.1 Special features 5
1.1.1.1 Finite-size effects 5
1.1.1.2 Surface effects 8
1.1.2 Biomedical applications 9
1.1.2.1 Magneto-mechanically induced cellular damage 9
1.1.2.2 Cell manipulation and separation 11

1.2 Magnetic Resonance Imaging (MRI) 13
1.2.1 Basic principles of MRI 13
1.2.1.1 The source of the MR signal 14
1.2.1.2 Spatial encoding 16
1.2.1.3 Spin-Echo imaging 17
1.2.2 Contrast-enhancing agents 18
1.2.2.1 T1 contrast agents 19
1.2.2.2 T2 contrast agents 22

1.3 Magnetic nanostructures 24
1.3.1 Synthetic antiferromagnetic nanostructures 25
1.3.1.1 Fabrication methods and materials 26
1.3.1.2 Physical characterization 31
1.3.2 Magnetic nanowires 38
1.3.2.1 Fabrication methods and materials 39
1.3.2.2 Physical characterization 41

2. Experimental details **43**

2.1 Fabrication techniques 43
2.1.1 Top-down approach 43
2.1.1.1 Laser Interference Lithography 43
2.1.1.2 Ion Beam Deposition 44
2.1.1.3 Magnetron Sputtering 46
2.1.2 Bottom-up approach 47
2.1.2.1 Porous anodic alumina templates 48
Substrate cleaning 49
Electropolishing 49
Anodization 49
Aluminium removal and Pore widening 50
2.1.2.2 Electrodeposition 51

2.2 Characterization methods 51
2.2.1 Scanning Electron Microscopy 52
2.2.2 X-Ray Diffraction 53
2.2.3 Superconducting Quantum Interference Device 53
2.2.4 Vibrating Sample Magnetometer 54
2.2.5 Magneto Optic Kerr Effect 55

3. Magnetic nanostructures **57**

3.1 Synthetic antiferromagnetic nanoparticles grown through the top- down route 57
3.1.1 Morphological and Structural Characterization 58
3.1.1.1 Scanning Electron Microscope (SEM) 58
3.1.1.2 Energy-dispersive X-ray spectroscopy (EDS) 61
3.1.2 Magnetic characterization 62
3.1.2.4 VSM measurements on magnetron sputtered samples 62
3.1.2.2 VSM measurement on IBD samples 66
3.1.2.3 VSM measurement on magnetron sputtered discs 72
3.1.2.4 MOKE analysis on magnetron sputtered discs 72

3.2 Nanowires in Porous Anodic Alumina templates 73
3.2.1 Template fabrication by Al anodization 73
3.2.2 Morphological Characterization 74
3.2.2.1 Scanning Electron Microscope (SEM) 75
3.2.2.2 X-Ray Diffraction (XRD) 84
3.2.3 Magnetic characterization 85
3.2.3.1 Superconductive Quantum Interference Device (SQUID) 85

4. Final remarks and future work **89**

Bibliography **91**

List of tables

1.1: Fabrication techniques and materials reported in literature about SAF-NPs. (*) not specified. 26
1.2: Thicknesses and materials of the deposited stacks by A. L. Koh et. al [47]. 28
1.3: Thicknesses and materials of the deposited stacks by Hu et. al [49, 50]. 28
1.4: Thicknesses and materials of magnetic nanowires, adapted from literature. (*) not specified. 40
3.1: Thicknesses, coercivity and remanence of deposited layers of Batch 1. 63
3.2: Thicknesses, coercivity and remanence of deposited layers of Batch 2. 65
3.3: Tthicknesses, coercivity and remanence of deposited layers of Batch 3. 66
3.4: Thicknesses, coercivity and remanence of deposited layers of Batch 4. (*) failed during deposition. 68
3.5: Thicknesses, coercivity and remanence of deposited layers of Batch 5. 69
3.6: Thicknesses, coercivity and remanence of deposited layers of Batch 6. 70
3.7: Electrodeposition parameters 77
3.8: Segments' lengths extracted from sem images where possible (S) and calculated through the deposition rates (DR). The total length of the nanowires (NW) is also reported. 81
3.9: Current density and charge values for each deposited layer of each sample. 82
3.10: Calculated mass values for each deposited layer of each sample. 83
3.11: Calculated lengths values for each deposited layer of each sample. 83

List of figures

1.1: Magnetic nanoparticles as platform materials for the integration of various modalities. various imaging modalities and therapeutic drugs can be ligated onto magnetic nanoparticle. 4
1.2: Different magnetic effects in mnps. the spin arrangement in (a) ferromagnet (FM) (b) antiferromagnet (AFM); D=diameter, Dc=critical diameter. hysteresis loop of (c) hard magnet (d) superparamagnet (SPM), (e) exchange bias magnet, (f) pure antiferromagnet..... 6
1.3: (a) Schematic of the energy barrier (EB) required for the magnetic moment to flip between their easy axis. (b) Illustration of particles in a (i) quasi-stable blocked and (ii) an unblocked freely rotating state [19] 7
1.4: TEM micrographs of (a) APTES coated nws and (b) BSA coated NWs. the scale bars are 50 nm. 10
1.5: Mechanism of generation of the echo signal. 18
1.6: Breast cancer imaged with (left) mammogram, (centre) MRI without contrast (right) MRI with contrast. 18
1.7: T1 relaxation rate as a function of concentration measured for (a) Gd_2O_3 nanodiscs of different diameters and (b) GdIO NPs of spherical (9 nm and 6 nm) and cubic (4 nm) shapes [41]. 20
1.8: Echo Planar Image (EPI) of mouse brain (a) before and (b) after PSSS-Mag1(Fe/Polysodium-4-styrene sulfonate ratio 1:2) passes through; Fast Low Angle Shot (FLASH) image of mouse brain (c) before and (d) as PSSS-Mag1 passes through [42]. 21
1.9: (a) Phantom image acquired under both T1- and T2-weighted sequences at 3 T and 37 °C. (b) MRI signal intensity (%) relative to the water control. Dotted lines are a guide for the eye [1].....22
1.10: Theoretical (black lines) and measured (points) r2 values of [Au(10 nm)/NiFe(10 nm)/Au(2.5 nm)/NiFe(10 nm)/Au(10 nm)] SAF-NPs as function of Saf-Np diameter. the reference theoretical values for spherical NiFe particles [13].....24
1.11: Schematic representation of antiferromagnetic structure. 25
1.12: NIL process: (a) Template formation by nanoimprint lithography, (b) residue layer removal by O2 plasma, (c) undercut profile creation in the underlayer resist, (d) metal film deposition, and (e) lift-off followed by (f) chemical etching. ..27
1.13: Colloidal lithography schematics. (a) Blank wafer, (b) photoresist coating, (c) sputtered magnetic stack, (d) polystyrene beads drop casted, (d) ion milling, (e) SAF creation, (f) removal of beads. 29

1.14: (a-d) SEM-images of SAF-NPs fabricated using (a) 60 nm, (b) 110 nm, (c) 200 nm, and (d) 500 nm polystyrene bead masks. (e) haadf-stem-image of a 110 nm diameter SAF-NP. Two NiFe layers (dark), separated by a gold spacer (bright) [13]. 30
1.15: (a) Hysteresis loop of an ideal SAF particle. (b) Hysteresis loop of a superparamagnetic particle. (c) Hysteresis loop of a vortex-state particle..... 31
1.16: Typical hysteresis loop of a synthetic antiferromagnetic nanoparticle [47]..... 32
1.17: Magnetic hysteresis loops of substrate-bound SAF nanoparticles before ion mill (red), after ion mill (blue) and after release in aqueous solution (black) [47]. 33
1.18: (Colour online): Comparison of safs with different release layers (cu, cuox or none) with CoFe layers thicknesses of (a) 60 Å and (b) 120 Å [47]..... 34
1.19: (a) Hysteresis loops for different thickness of the magnetic layer. Circle, triangle, and square curves represent t=30, 60, and 120 Å respectively. (b) hysteresis loops for different thickness of the non-magnetic spacer. adapted from [49]..... 35
1.20: (Colour line) susceptibility normalized by the mass of Co+Fe vs in-plane applied field. Adapted from [50]. 36
1.21: (a) The single coupled bilayer motif. (b) Polar MOKE of the single bilayer (c) the multilayer stack, where the basic motif is stacked 12 times. (d) VSM easy axis hysteresis loop of the 12-repeat motif multilayer stack [6]. 36
1.22: (a) Magnetic saturation field of SAF-NPs in function of the spacer thickness. (b) magnetic hysteresis curves of 222 nm SAF-NPs [au(100)/nife(100)/au(x)/nife(100/au(100)] with thicknesses in Å. [13] 37
1.23: Nanoparticle size, shape and surface charge dictate biodistribution among the different organs including the lungs, liver, spleen and kidneys [63]..... 38
1.24: Magnetization hysteresis curves of 100 nm wires as a function of the wire length at 10 K, with the applied field perpendicular (open circles) and parallel (solid squares) to the wire axes [69]. 41
2.1: Interference lithography schematics. (a) experimental set-up adapted from [89], (b) cross exposure with resultant pattern. 44
2.2: Ion beam system schematic representation, Norkiko 3000 at INESC-MN..... 45
2.3: Nordiko2000 DC/RF magnetron sputtering system; (a) schematic representation, (b) picture. 47
2.4: Schematic representation of hexagonally arranged nanopores in anodic porous alumina (a) and cross-sectional view of anodized layer (b). Adapted from [90].... 48
2.5: Experimental set-up for (a) electropolish and (b) anodization. 49
2.6: General scheme describing the fabrication of nanorods/nanowires by electrodeposition into nanoporous templates. From [80]..... 51
2.7: VSM operation principle schematics. 54
3.1: SEM images of patterned discs previous deposition (SAF_Dots0). (a) magnification of 10 000x, (b) magnification of 100 000x 58

3.2: SEM images of the magnetron sputtered discs after resist development (SAF_Dots1). (a) Magnification of 2 000x, (b) magnification of 40 000x. 59
3.3: Analysis of discs diameter (SAF_Dots0). (a) Long axis' histogram, (b) short axis' histogram. 60
3.4: Analysis of discs diameter (SAF_Dots1). (a) long axis' histogram, (b) short axis' histogram. 60
3.5: EDS spectrum of sample SAF_Dots1. 61
3.6: Typical hysteresis loop characterized by diamagnetic contribution of glass thin film. Sample CoFeB_1, parallel direction. (a) Raw data, (b) processed data. 62
3.7: Schematic structure of the deposited stacks. 63
3.8: (a) In plane parallel hysteresis loops of batch 1 samples. (b) Coercivity and remanence as function of spacer thickness. 64
3.9: In plane parallel hysteresis loops of CoFe_3 and CoFe_4 samples. Zoom: detail around zero of CoFe_3. 65
3.10: In plane parallel hysteresis loops of Batch 3 samples. 67
3.11: In plane parallel hysteresis loops of Batch 4 samples. 68
3.12: In plane parallel hysteresis loops of Batch 5 samples. 69
3.13: Comparison between (a) coercivity and (b) remanence values of samples Au_1, Au_2, Au_3 and Au_8, Au_9, Au_10. 70
3.14: In plane parallel hysteresis loops of batch 6 samples. 71
3.15: In plane parallel (0deg) and perpendicular (90deg) hysteresis loops of sample J 72
3.16: MOKE measurement on sample SAF_Dots1 73
3.17: First anodization (24h) curves. 73
3.18: Second anodization curves. From left to right: pre-anodization, anodization and after-anodization. 74
3.19: SEM images of the paa templates after hard anodization with subsequent pore widening. (a) Top surface, (b) bottom surface. 75
3.20: Pore diameter distribution. 75
3.21: Comparison of intensity deposition curves; (a) layer Au1, (b) layer Fe2, (c) layer Au3, (d) layer Fe4, (e) layer Au5. 76
3.22: SEM images calibration samples. (a) HA_Calibration01, (b) HA_Calibration02. .77
3.23: SEM image of HA_03. 78
3.24: SEM images of (a) HA_05, (b) HA_06, (c) HA_07 and (d) HA_08. 79
3.25: SEM image of HA_12.2. 80
3.26: Comparison between calculated, extrapolated (SEM) and expected (DR) lengths of NWs. 84
3.27: X-ray diffraction analysis of sample C2. 84
3.28: In-plane hysteresis loops of samples HA_Calibration1 and HA_Calibration2 (C1 and C2, respectively). 85

3.29: In-plane hysteresis loops of samples HA_05, HA_06, HA_07 and HA_08 (05,06,07 and 08, respectively). 86
3.30: Comparison between (a) remanence as a function of total fe thickness and (b) remanence as a function of Au spacer length of samples HA_05,06,07,08. 87

Abbreviations

NPs	Nanoparticles
MNPs	Magnetic Nanoparticles
SP-NPs	Superparamagnetic Nanoparticles
SP	Superparamagnetism
SAF-NPs	Synthetic Antiferromagnetic Nanoparticles
SAFs	Synthetic Antiferromagnets
SAR	Specific Absorption Rate
M_s	Magnetic saturation
MFH	Magnetic Fluid Hyperthermia
MNS	Magnetic Nanostructures
MRI	Magnetic Resonance Imaging
FM	Ferromagnet
AFM	Antiferromagnet
SPM	Superparamagnet
RKKY	Ruderman-Kittel-Kasuya-Yosdida
AC	Alternating Current
NWs	Nanowires
TEM	Transmission Electron Microscopy
Py	Permalloy
NMR	Nuclear Magnetic Resonance
RF	Radiofrequency
FID	Free Induction Decay
TE	Echo Time
MR	Magnetic Resonance
PAA	Porous Anodic Alumina
ARC	Anti-reflective Coating
IBD	Ion beam Deposition
PVD	Physical Vapour Deposition
XRD	X-Rays Diffraction
SEM	Scanning Electron Microscopy
EDS	Energy-Dispersive X-Ray Spectroscopy

BSE	Backscattered Electrons
SQUID	Superconducting Quantum Interference Device
DC	Direct Current
VSM	Vibrating Sample Magnetometer
MOKE	Magneto Optic Kerr Effect

Chapter 1

Introduction

Nanoparticles (NPs) are particles having at least one dimension in the nano-meter size. Such nano-entities are categorized by high surface-area-to volume ratio and are therefore particularly strong, versatile, and reactive, when compared to the bulk state. These specific properties offer new and interesting possibilities of optimizing optical, mechanical, and magnetic properties of NPs, among others. Particularly, magnetic NPs are of large interest, having successfully demonstrated their utility in a widespread range of applications, namely magnetic fluids, magnetic energy storage, catalysis, environmental remediation, magnetic inks, and biotechnology/biomedicine such as contrast agents in Magnetic Resonance Imaging [1, 2].

1.1 Magnetic nanoparticles and their biomedical applications

Progress in nanotechnology in particularly in the NPs research field has allowed the synthesis of magnetic NPs with precise morphology, and to suitably modify particle surfaces, manipulating their characteristics for precise applications [3]. Extensive studies have been carried out, and protocols have been developed aiming the optimization of magnetic nanoparticle characteristics such as composition, surface charge, shape, size, size distribution, and magnetic properties.

With the latest evolution and demands in nanomedicine, magnetic NPs (MNPs) are attracting increasing attention due to their potential to improve conventional therapeutic procedures and traditional clinical diagnostic, as well as to introduce novel approaches in biomedicine and tissue engineering [4].

MNPs are typically classified in three major groups: Pure metals, metal oxides and magnetic nanocomposites. The most popular in the biomedical field are Co, Fe, Ni, iron oxides and some ferrites. Among them, iron oxide NPs (usually Fe_2O_3 or Fe_3O_4) are the most used due to their well-known lower toxicity. The key issues affecting the biocompatibility and toxicity of such materials are the characteristics of the components that are magnetically reactive, such as cobalt, iron and nickel, the size of the NPs, and their coating. Knowing that magnetic NPs can reveal novel phenomena, such as super-

paramagnetic behaviour, high magnetic field irreversibility, and additional anisotropic contribution, the specific biomedical application is determined by the distinct magnetic properties. These properties are, in turn, ruled by the type of magnetic nanoparticle, synthesis procedure, interaction between NPs, and the nanoparticles' size, shape and distribution. Considering this, an appropriate synthesis procedure must be selected to achieve specific and precise performance [5].

Among several magnetic NPs that have been developed, the ones that exhibit fast change of magnetic state with the application of an external magnetic field, negligible remanence (magnetization at zero field) and coercivity (the field required to bring the magnetization to zero) at room temperature, are usually desired; these features are essential in biomedicine, as they prevent particles' agglomeration when dispersed in solution [6, 7]. Thus, this specific type of NPs must combine high susceptibility and loss of magnetization after removal of the magnetic field, which make superparamagnetic nanoparticles (SP-NPs), synthetic antiferromagnetic nanoparticles (SAF-NPs) and vortex state nanodiscs very suitable in biomedical applications, as discussed in section 1.1.2.

The appropriate protection and functionalization of the magnetic NPs in nanomedicine is ruled not only by their intrinsic properties (magnetic saturation (M_s) and Curie temperature (T_c)) but also by their biophysical properties (colloidal stability, nontoxicity, SAR, and biocompatibility) under pH conditions similar to the physiological ones [8]. To avoid magnetic NPs' agglomeration, also the nanoparticle surface chemistry must be taken into account and should be stabilized by covering them with different types of materials, including inorganic and organic coatings [3]. Additionally, demands from the biomedicine require MNPs that are water stable at pH ≈ 7 and with salinity values close to the physiological ones. Such colloidal stability will be dependent on NPs' dimensions, surface chemistry, and charge [5]. Other limitations or requirements strongly rely on the use of the NPs, whether for in vitro or in vivo applications. In the case of in vitro applications, the limitations are not as restricted as in the in vivo case. For in vivo applications, the magnetic structures need to be covered with a biocompatible polymer (if the nanoparticle is not biocompatible) after or during the synthesis procedure to avoid toxicity, decrease the risk of blood capillary obstruction, and prevent nanoparticle aggregation [3, 9].

Due to their specific magnetic properties, some MNPs can be precisely collected in a desired location by an applied magnetic field, which is essential for target drug and gene delivery [10] allowing new therapeutic approaches of merging multistage short-term

magnetic control and directing with enhanced mediated-ligand targeting in recently developed nano-delivery systems [4].

Furthermore, MNPs are being developed for hyperthermia and heat-activated drug release as a result of their heating ability in high-frequency magnetic fields. Large efforts are being spent on the improvement of hyperthermia techniques for clinical uses. Advances in magnetic nanoparticle research contributed to the fast and, sometimes, disruptive development of magnetic hyperthermia (MH), making this technique a promising tool for cancer treatment due to the possibility of targeting cancerous tissues. This approach leads to lower side effects than traditional radiotherapy and chemotherapy. Similarly, controlled drug release trough MNPs has an essential role in the future of personalized medicine; once recent/ongoing clinical tests revealed substantial reduction of such side effects (nausea/vomiting, fatigue, constipation, and fever/chills) [11]. The outstanding safety profiles and appropriate magnetic properties of SP, SAF and vortex state NPs make them very good platforms for the design of cancer treatments that have negligible side effect and with the capacity to target cancers that cannot be obtained by other types of nanostructures [5].

Moreover, the unique spin arrangement of two novel types of magnetic nanostructures (MNS), namely the spin-vortex and antiferromagnetic state, have shown promising results respectively in the fields of magneto-mechanically induced cell damage and in magnetic resonance imaging (MRI). The basis of magneto-mechanical actuation in cells is the spatial rotation that the magnetic nanostructures perform, in order to align themselves with an applied magnetic field; this novel approach is promising as a new cancer therapy since it has some advantages when compared to other techniques, such as lower strength and frequency of the required magnetic field in comparison to the MH technique. The benefits of spin vortex nanodiscs rely on their zero remanence and large single domain when compared to SP-NPs [12]. SAFs also present zero remanence and low coercivity, which makes them suitable and effective as contrast agents in MRI [13], as lately discussed.

The magnetic NPs described above have found applications in many several areas, as briefly presented. More recently, attempts have been made to combine contrast agents for MRI, magnetic drug delivery, biomolecule separation and magnetic hyperthermia treatment into one system, namely theragnosis, in which magnetic NPs serve as multi-mode platforms for integrated applications. Multi-mode systems possess benefits of each modality operating in a synergistic manner. Various chemical moieties on the surfaces of nanoparticles can

serve as conjugating sites where other imaging modalities or functional biomolecules can be ligated. For example, in order to enhance MRI contrast effects of magnetic nanoparticle, other imaging active moieties such as those containing fluorophores and/or radioisotopes can be added [14]. The additional ligating molecules can also be functionalized so that they sense the presence of specific biomolecules or environmental factors. In addition, the magnetic nanoparticles can be employed as platforms to which a variety of therapeutically active chemical or biological agents can be conjugated to enhance the selectivity of hyperthermically active nanoparticles, as presented in Figure 1.1 [15].

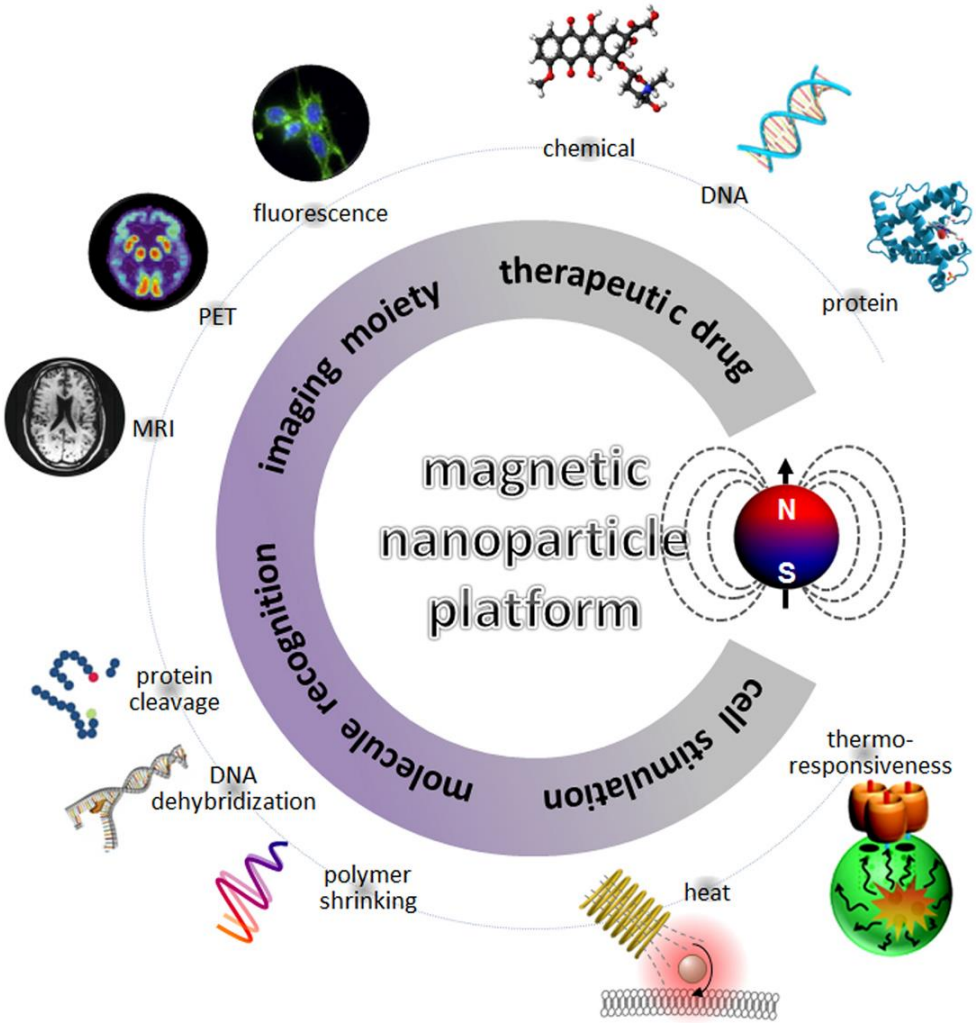

Figure 1.1: Magnetic nanoparticles as platform materials for the integration of various modalities. Various imaging modalities and therapeutic drugs can be ligated onto magnetic nanoparticle.

1.1.1 Special features

Different kinds of NPs, such as quantum dots, carbon nanotubes, gold NPs, silica NPs, polymeric NPs, and magnetic NPs have been designed and synthesized [16]. The magnetic properties of MNPs rely on the different type of possible magnetic states, such as diamagnetic, paramagnetic, ferromagnetic, antiferromagnetic and superparamagnetic states. Diamagnetic atoms are characterized by the presence of diamagnetic electrons, i.e. electrons paired together in an orbital so that the total spin is zero, and slightly repel magnetic fields. On the other hand, a paramagnetic atom is considered so if it has at least one unpaired electron, that realign in response to an external magnetic field, being therefore attracted towards it; paramagnets do not retain magnetization in absence of a magnetic field because thermal energy randomizes electron spin orientations. Permanent magnetizations can also be achieved, which is the characteristic behaviour of a ferromagnetic material. Ferromagnetism arises from two effects of quantum mechanics: spin and Pauli exclusion principle, which result in a spin configuration that remains aligned in the direction of the applied magnetic field even when the field is switched off. A similar behaviour is achieved by antiferromagnetic materials (high saturation magnetization) in presence of a magnetic field, although these materials have the capability to return to a zero state when the field is taken away. The same property of zero remanence and coercivity can be also achieved through atoms in the superparamagnetic state: in this situation the spins are all oriented in a single domain in the direction of the applied field, leading to high saturation values. The main key issues that dominate the magnetic properties of nanoparticles are finite-size effects and surface effects which give rise to various special features, as presented in Figure 1.2; the firsts result, for example, from the quantum confinement of the electron, whereas the second ones are typically related to the symmetry breaking of the crystal structure at the boundary of each particle.

1.1.1.1 Finite-size effects

The two most finite-size effects in nanoparticles are the single-domain limit and, consequently, the superparamagnetic one. It is well known that, in large magnetic particles, there is a multi-domain structure, where regions of uniform magnetization are separated by domain walls. The formation of the domain walls is a process driven by the balance between the magneto-static energy (ΔE_{MS}), which increases proportionally to the volume of the materials and the domain-wall energy (E_{dw}), which increases

proportionally to the interfacial area between domains. If the sample size is reduced, there is a critical volume below which it costs more energy to create a domain wall than to support the external magneto-static energy (stray field) of the single-domain state.

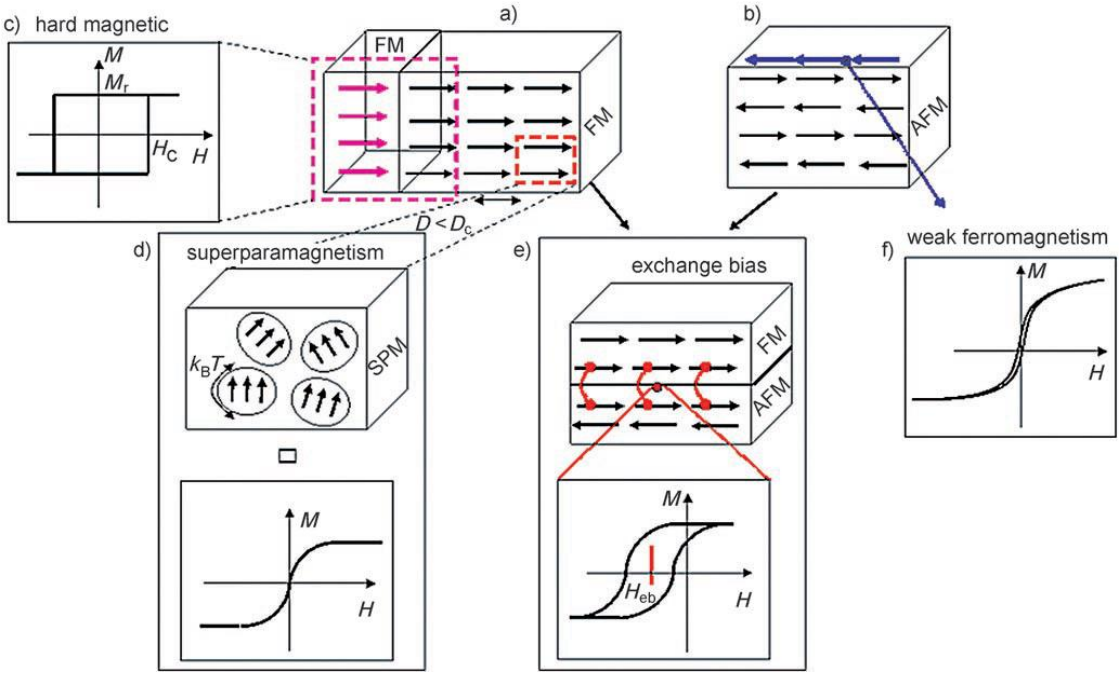

Figure 1.2: Different magnetic effects in MNPs. The spin arrangement in (a) ferromagnet (FM) (b) antiferromagnet (AFM); D=diameter, Dc=critical diameter. Hysteresis loop of (c) Hard magnet (d) Superparamagnet (SPM).(e) Exchange bias magnet (f) Pure antiferromagnet

This critical diameter typically lies in the range of a few tens of nanometers and depends on the material. The critical diameter of a spherical particle, D_c, below which it exists in a single-domain state is reached when $\Delta E_{MS} = E_{dw}$, which implies:

$$\mathrm{D_c} \approx 18 \frac{\sqrt{\mathrm{AK_{eff}}}}{\mu_0 {M_s}^2} \tag{1.1}$$

where A is the exchange constant, K_{eff} is the anisotropy constant, μ_0 is the vacuum permeability, and M_s is the saturation magnetization.

A single-domain particle is uniformly magnetized with all the spins aligned in the same direction. The magnetization will be reversed by spin rotation since there are no domain walls to move. This is the reason for the very high coercivity observed in small nanoparticles. [17] Another source for the high coercivity in a system of small particles is the shape anisotropy. The departure from sphericity for single-domain particles is significant and has an influence on the coercivity [3].

The second important phenomenon which takes place in nanoscale magnetic particles is the superparamagnetic limit. Superparamagnetism can be understood by

considering the behaviour of a well-isolated single-domain particle. The magnetic anisotropy energy per particle which is responsible for holding the magnetic moments along a certain direction can be expressed as follows:

$$\mathrm{E}(\theta) = \mathrm{K_{eff}V}\sin^2(\theta) \tag{1.2}$$

where V is the particle volume, K_{eff} the anisotropy constant and θ is the angle between the magnetization and the easy axis.

The energy barrier $K_{eff}V$ separates the two energetically equivalent easy directions of magnetization. With decreasing particle size, the thermal energy, k_BT, exceeds the energy barrier $K_{eff}V$ and the magnetization is easily flipped. For $K_{eff}V$>k_BT, the system behaves like a paramagnet, instead of atomic magnetic moments, there is now a giant (super) moment inside each particle. This system is named a superparamagnet. Such a system has no hysteresis and the data of different temperatures superimpose onto a universal curve of M versus H/T [18].

The relaxation time of the moment τ, is given by the Néel-Brown expression (eq. 1.3); where k_B is the Boltzmann' constant, and $\tau_0 \approx 10^{-9}s$.

$$\tau = \tau_0 \exp\left(\frac{K_{eff}V}{k_BT}\right) \tag{1.3}$$

If the particle magnetic moment reverses at times shorter than the experimental time scales, the system is in a superparamagnetic state, if not, it is in the so called blocked state [3], as presented in Figure 1.3.

Moreover, considering the magnetic interactions between nanoparticles which have a strong influence on the superparamagnetic relaxation, the behaviour of the system becomes more complicated. The main types of magnetic interactions that can be present in a system of small particles are: Dipole–dipole interactions, direct exchange interactions for touching particles, super-exchange interactions for metal particles in an insulating matrix and RKKY (Ruderman-Kittel-Kasuya-Yosdida) interactions, which is crucial for SAFs.

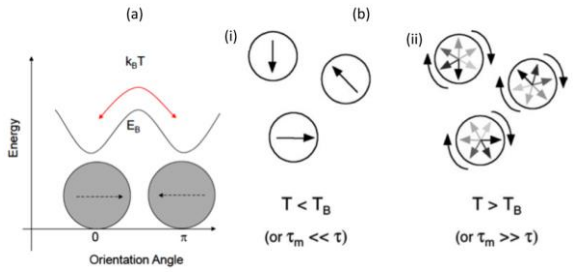

Figure 1.3: (a) Schematic of the energy barrier (EB) required for the magnetic moment to flip between their easy axis. (b) Illustration of particles in a (i) quasi-stable blocked and (ii) an unblocked freely rotating state [19]

1.1.1.2 Surface effects

As the particles size decreases, a large percentage of all the atoms in a nanoparticle are surface atoms, which implies that surface and interface effects become more important. Owing to this large surface atoms/bulk atoms ratio, the surface spins make an important contribution to the magnetization. This local breaking of the symmetry might lead to changes in the band structure, lattice constant or/and atom coordination. Under these conditions, some surface and/ or interface related effects occur, such as surface anisotropy and, under certain conditions, core–surface exchange anisotropy can occur.

Surface effects can lead to a decrease of the magnetization of small particles, for instance oxide nanoparticles, with respect to the bulk value. This reduction has been associated with different mechanisms, such as the existence of a magnetically dead layer on the particle's surface, the existence of canted spins, or the existence of a spin-glass-like behaviour of the surface spins [19]. On the other hand, for small metallic nanoparticles, for example cobalt, an enhancement of the magnetic moment with decreasing size was reported as well [20]. Another surface-driven effect is the enhancement of the magnetic anisotropy, K_{eff} , with decreasing particle size. [3] This anisotropy value can exceed the value obtained from the crystalline and shape anisotropy and is assumed to originate from the surface anisotropy.

For uncoated antiferromagnetic nanoparticles, weak ferromagnetism can occur at low temperatures (Figure 1.3 f), which has been attributed to the existence of uncompensated surface spins of the antiferromagnet. This property has been further investigated in this work, making synthetic antiferromagnets very suitable nanostructures in several biomedical areas.

Some important aspects should be emphasized. The magnetic behaviour of an assembly of nanoparticles is a result of both the intrinsic properties of the particles and the interactions among them. The distribution of the sizes, shapes, surface defects, and phase purity are only a few of the parameters influencing the magnetic properties, which makes the investigation of the magnetism in small particles very complicated. One of the great challenges remains the manufacturing of an assembly of monodisperse particles, with well-defined shape, a controlled composition, ideal chemical stability, tunable interparticle separations, and a functionalizable surface. Such particles will tremendously facilitate the discrimination between finite-size effects, interparticle interactions, and surface effects [21]. Thus, the synthesis of magnetic NPs with well-controlled characteristics is a very important task, which will be described in more detail in the next

sections, with particular attention on the synthesis of high aspect ratio NPs (nanowires) and synthetic antiferromagnets.

1.1.2 Biomedical applications

Among all nanomaterials, MNPs are one of the most frequently chosen systems for biomedical applications due to their nontoxicity, biocompatibility, and particularly their inducible magnetic moment that allows them to be directed to a defined site. Also, MNPs are one of the most promising system for theragnostic, they can be used as contrast image agents and at the same time heated with the use of an external alternating current (AC) magnetic field [11]. In this section, a brief description of some possible applications is given, such as magneto-mechanically induced cellular damage, cell manipulation and separation; a more detailed discussion about magnetic resonance imaging is presented in section 1.2.

1.1.2.1 Magneto-mechanically induced cellular damage

The current cancer treatment techniques, such as surgery, radiotherapy and chemotherapy, are highly aggressive to the organism due to invasiveness and possible sides effects. In this context, the different properties of nanoparticles have been studied and considered as potential path for next generation oncologic treatments [22]. Particularly, there exists an increasing interest in the use of magnetic nanostructures to mechanically stimulate and destroy specific cells, since magnetic nanomaterials can be remotely controlled by applying external magnetic fields and also due to the fact that cells convert mechanical stimuli into biochemical signals, via a process known as mechano-transduction [23, 24].

Most of the performed experimental studies used SP nanoparticles. However, their reduced saturation magnetization implies that high magnetic fields must be applied in order to manipulate them, which can lead to a destruction of healthy tissues by undesired local overheating [25].

An interesting alternative is known as magneto-mechanical induced cell death, which consists in exerting forces or torques on cells, using magnetic nanoarchitetures, in order to induce the programmed cell death, namely apoptosis [23]. The produced magnetic torques depend on the characteristics of the applied field as well as on the magnetic moment and magnetic susceptibility of the nanostructures.

The typical characteristics of such nanostructures are a high saturation magnetization and low field magnetic susceptibility, as well as a reduced remanence, to be easily manipulated and to do not agglomerate when dispersed in solution [3].

Leulmi et al. [25] have carried out studies of three types of disc-shaped anisotropic MNPs, namely SAFs, vortex and polycrystalline magnetite particles with random anisotropy. The reported structures are characterized by a diameter of 1.3 μm and have all been coated with gold layers. After a comparison between the magnetic properties of such structure, the authors have been concluded that the vortex state configuration have be considered the best option to start an in vitro study on the magneto-mechanical effect in human renal carcinoma cells, due to its magnetic softness and ease of fabrication.

Therefore, the surface of these microdiscs have been functionalized with specific ligands in order to target specific renal cancer cells (SKRC-59) during their incubation with the magnetic particles, having reached an average of 30 particles per cell. Then, an alternating magnetic field (30 mT) with a low frequency (20 Hz) have been applied during 1 h and the impact of the treatment has been analysed. The statistical results, obtained by measuring the proportion of the different categories of cells (live vs. apoptotic vs. necrotic) after the procedure, indicate a significant increase on the cancer cell death by apoptosis (70%), which is the natural death of the cell.

Besides disc-shaped magnetic nanostructures, other types of magnetic nanoarchitectures and magnetic fields have been studied in the context of magneto-mechanical induced cell death, such as magnetic nanowires (NWs).

Martinez-Banderas et. al. [22] developed a bimodal strategy to induce cancer cell death through the combination of the chemo-toxic effect caused by an anticancer drug (doxorubicin) with the mechanical perturbation exerted by Fe nanowires, with average length of 6.4 μm and diameter between 30 and 40 nm, exposed to a 10 Hz frequency AC magnetic field of 1 mT for a period of 10 minutes. The NWs have been coated with 3-aminopropyltriethoxysilane (APTES) or with bovine serum albumin (BSA), as shown in Figure 1.4, in order to be further functionalized with doxorubicin (DOX).

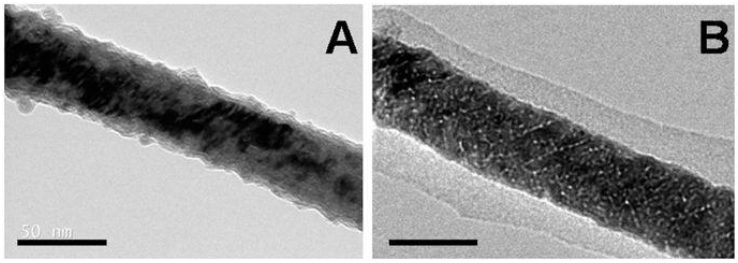

Figure 1.4: TEM micrographs of (A) APTES coated NWs and (B) BSA coated NWs. The scale bars are 50 nm.

The efficiency of this technique has been determined by the viability reduction of breast cancer cells (MDA-MB-231). The nanostructures have been incubated and it has been verified that the functionalized NWs have demonstrated a high degree of internalization by the cells, making them suitable as carriers for drug delivery. In this work, the authors have concluded that BSA coated nanoarchitetures have shown better internalization with a reduction of 73 % in cell viability, as a proof that the combination of the chemo-toxic and magneto-mechanical treatment modes led to synergistic effects, turning this technique into an attractive approach for novel cancer therapies.

Besides the nanostructures discussed above, the suitability of SAFs have also been investigated in the magneto-mechanical induced cell death field.

Mansell et al. [26], for example, have fabricated 2 μm diameter disc-shaped SAFs with perpendicular magnetic anisotropy and a repeated motif of ultrathin CoFeB/Pt layers to be applied in an in vitro study with glioma cells. The efficiency of such structures has been compared with Py spin vortex microdiscs. In this case, brain tumour cells (U87) have been incubated for 24 hours at a concentration of 50 particles per cell. The cell damage has been quantified after the application of a rotating (20Hz) magnetic field (1 T) for one minute. It has been verified that the CoFeB/Pt microdiscs induced cellular death on 62.3% of the cancer cells; however, under the same conditions, the Py microdiscs have only killed 12.2% of the glioblastoma cells. The torque applied by the two types of particles have also been measured, having a maximum value of 20 fNm for CoFeB/Pt and 75 fNm for the Py nanostructures. Therefore, it has been shown that the symmetry of the anisotropy is more relevant than the magnitude of the torque in causing effective cell destruction. Consequently, the ability to explore the anisotropy of nanostructures can open new paths for the magneto-mechanical induced cell death.

1.1.2.2 Cell manipulation and separation

The isolation and sorting of particular cells from heterogeneous populations is essential for various cell-based applications in multiple areas, such as cell and molecular biology, biochemistry and immunology, as well as for clinical research [12]. Numerous cell isolation and sorting techniques have been developed; the standard ones for the separation of cells include processing steps of filtration, centrifugation and sedimentation. However, in situations where cell size or density differences are not significant, effective cell separation is impeded in these techniques and other methods must be employed, such as fluorescence-activated cell sorting (FACS) and magnet-activated cell sorting

(MACS) [27]. In this context, MNPs provide and important means of applying force to biological systems.

While the standard particles currently used for magnetic manipulation of cells are superparamagnetic beads, an alternative type of nanoparticle with considerable potential in this area is electrodeposited nanowires; these structures possess several advantages, such as high surface area, large magnetic moments and shape anisotropy. In addition, they can be grown over a wide range of sizes and be properly tuned according the specific application.

Hultgren et al. [28] have successfully demonstrated that long ferromagnetic Ni nanowires (L=35 μm) have potential to outperform magnetic beads in cell separation applications. Base on the previous work Hultgren et. al [29] have explored the effects of the wire length on separation efficiency. The authors have stated that the wires generate high-purity separation over a considerable range of size; however, it has found out that the separation yield is optimized when the nanowires' length matches the average cell diameter.

In addition, it is crucial to assess to the biocompatibility of these nanostructures, due to the potential toxic effects associated with some materials (Ni for instance [12]); it would be of interest to fabricate nanowires with similar physical properties but constituted by more biocompatible materials. In this context, Fe nanowires and compounds have been fabricated, as reported by several authors, namely Ivanov et al. [30]

Besides nanowires, SAFs have been evaluated as possible surrogates to superparamagnetic beads; by modifying their surface with special protein or by applying a fluorescent labelling and adjusting the thicknesses of the magnetic layers, they can be used for detection of target molecules or to manipulate biological target through the application of magnetic fields. Due to their higher magnetic moments when compared to SP-NPs, SAFs have been analysed as potential candidates for the improvement of the current magnetic cell separation and manipulation techniques.

An in vitro study of these nanostructures has been performed by Zhang et. al [31], where they have been used to separate lung cancer cells (H1650) from blood sample. Firstly, they have been coated with silica shell and then conjugated with protein (streptavidin) in order to be capable to link to the cells of interest, making them highly magnetically responsive. Then, after the incubation of the cancer cells with the nanostructures, blood samples have been mixed with the stained cells. Afterwards, the spiked blood samples have been pushed through a magnetic separation device and the captured cells have been analysed using an optical microscope. In this process, a

capture efficiency of 46.8% has been achieved, indicating that SAFs can be used for the separation of cells from blood samples and, when combined to a subsequent optical analysis, possibly contribute to cancer detection in an initial stage.

1.2 Magnetic Resonance Imaging (MRI)

MRI is a non-invasive powerful diagnostic technique in medical science. This technique has several advantages, including extreme imaging flexibility, non-ionizing radiation, patient harmlessness, high patient acceptance high-resolution images with an excellent soft tissue contrast between different tissues, provision of physiological parameters and acquisition of unique clinical information. As compared to the imaging modalities, the main advantage is its high spatial resolution, whereas its major drawback is represented by the limited sensitivity of its probes [32]. Over the last decades, numerous attempts have been made to improve sensitivity and facilitate biological and functional information-rich imaging by the use of MNPs and/or magnetic ions [33], as described in section 1.2.2.

1.2.1 Basic principles of MRI

MRI is a tomographic imaging technique that produces images of an object from externally measured nuclear magnetic resonance (NMR) signals [34]. The precession of nuclear magnetic moments when they are placed in an external magnetic field is one of the fundamental principles of MRI. As a result of this motion, when a given sample, with its magnetic moments randomly oriented, is placed inside a strong magnetic field, a net magnetization in the direction of the field, called longitudinal magnetization, is generated [35].

Through the application of a properly adjusted RF pulse, it is possible to tilt magnetization away from current direction to originate a transverse magnetization component. When the RF pulse is switched off, both components of the magnetization will return, or ‘relax’, to their previous states in the presence of a static magnetic field. Due to this relaxation processes, there is therefore the production of a weak radiofrequency signal, which is detected by RF-coils and subsequently processed in order to produce an image. [36]

The main advantages of MRI are the use of non-ionizing radiation, high spatial resolution, great anatomic detail and improved soft tissue contrast. However, due to the

weak intensity of the generated signal, contrast agents are often employed in order to increase the contrast of the acquired images [32].

The purpose of this section is to provide a brief review of the fundamental principles of MRI, with a more detailed explanation on the difference between its types of contrast agents and the associated particles that lead to a better resolution of the images.

In this section the source of the MR signal, its excitation and return to equilibrium are briefly described; an overview of spatial encoding and Spin-Echo imaging mechanism are presented as well.

1.2.1.1 The source of the MR signal

The basis of the generation the MR signal relies on the nuclear magnetic resonance phenomenon. As its name implies, NMR involves nuclei (of an object to be imaged), magnetic fields (generated by an imager) and the resonance phenomenon, arising from the interactions of the nuclei with the magnetic fields [36].

A correct description of what happens when tissues are subjected to a magnetic field rely on quantum mechanics; however, all the theory necessary for MRI can be based on a simple classical model in which a certain nuclei that spin around their own axis behave like small magnets; for clinical imaging, hydrogen is the most frequently used nucleus; such nuclei possess spin ½, and are the only case considered below [34]. Under normal circumstances, these tiny magnets are randomly distributed in space, their magnetic moments cancel each other out, and thus the net magnetic vector is zero. When an external magnetic field **B** is applied to a nucleus possessing a magnetic moment, an interaction takes place. The energy of the nucleus changes by an amount -**m**·**B**, where the scalar product accounts for the orientation of **m** relative to **B**. The energy difference between the two states of the nucleus that have spin angular momentum components $\pm\hbar/2$ in the direction of **B** is $\Delta E = -\gamma\hbar B$, where $\hbar$ and γ are respectively Planck's constant h divided by 2π and the gyromagnetic ratio. These two particular states are often referred as 'spin-up' and spin-down, and do not evolve in time [32]. The parallel alignment is the lower energy state and is thus the preferred alignment, whereas the antiparallel alignment is referred as the higher energy one. The energy difference between the two states is very small (usually close to 1 [35], and in equilibrium state at a temperature T the probabilities p_{up} and p_{down} of observing the up and down states, respectively, are given by the Boltzmann factor:

$$p_{up}/p_{down} = \exp\left(-\Delta E/k_b T\right) \tag{1.7}$$

Other states of the nuclear spin in a magnetic field are dynamic; they change as a function of time. If a weak magnetic field $\boldsymbol{B}_1$ is applied perpendicular to a static magnetic field $\boldsymbol{B}_0$ aligned with the z-axis and B_1 is made to oscillate at an angular frequency $\omega_0 = \Delta E/\hbar = |\gamma B_0|$, the nuclear spins will execute a complex periodic oscillation between the two stationary states; If the B_1 field is removed when a nuclear spin is in between the stationary states, it transverse components will continue to oscillate between their allowed values at the angular frequency ω_0. The phenomenon of magnetic resonance results from the time evolution of spin states in combined static and resonantly oscillating magnetic fields [36].

When a patient is submitted to a strong external magnetic field B_0, aligned for instance along the z-direction, the nuclei adopt one of the two possible orientations described above; The energy difference between the two populations give rise to a net magnetization vector (M_z) aligned to the external magnet. Individual nuclei do not actually line up with the magnetic field but precess around the direction of the external field. The frequency of this precession is $f_0 = \gamma B_0/2\pi$ and is so called Larmor frequency [34].

The net magnetization vector from the nuclei inside the magnet in its equilibrium state is static and does not produce a measurable signal. To obtain information from the spins, the direction of the net magnetization must be altered. The precessing spins are thus excited by a radiofrequency pulse energy at exactly Larmor frequency (resonant condition). In this situation two phenomena occur: first, enough protons absorb energy to jump from the parallel state to a higher level of the antiparallel state, and second, the spins are 'whipped' to precess in phase. The effect is that the net magnetization M_z flips 90° from the positive z-axis to the transverse plane. The net magnetization in the transverse plane rotates around the B_0 field at ω_0 angular frequency. This rotating transverse magnetization can be measured, because it will induce an alternating current (AC) in the receiver coil placed around the patient [35].

The time-depend behaviour of the magnetization in presence of an applied magnetic field can be accurately described by the use of the Block equation [36], not reported is this brief introduction.

After the RF pulse is switched off, the system goes back to its initial configuration. This means that the magnetization decays over time, which is represented by a decreasing magnitude of M_z in the transverse plane. Consequently, the induced signal in the receiver coil will decrease in time. This decreasing signal is called the free induction decay (FID). The time required for the signal to return to equilibrium is the relaxation time.

As previously referred, two interdependent relaxation processes exist: transverse relaxation and longitudinal relaxation. The process of realignment to the external magnetic field is called the longitudinal relaxation process. It is characterized by the T_1, relaxation time. T_1 is defined as the time required for the system to recover to 63% of its equilibrium value after it has been exposed to a 90° RF pulse. The second process of relaxation, the transverse relaxation, depends on the spins precessing around the magnetization vector. Initially, after the excitation by the RF pulse, the spins precess completely in phase. However, as time passes, the observed signal starts to decrease because the spins begin to diphase due to small differences in the Larmor frequency induced by random local magnetic inhomogeneities, due to spin-spin interaction and inhomogeneity of the main static magnetic field B_0. This process is called the transverse relaxation or spin-spin relaxation and is characterized by T_2 relaxation time. T_2 is the time it takes for dephasing to decay the signal to 37% of its original value. Various human tissues have different T_1 and T_2 values, with T_2 always shorter that T_1 [35].

1.2.1.2 Spatial encoding

To create an image, the MR signal from the H-protons must contain information about the position of the latter ones in the patient. This is done in three steps: slice selection, frequency encoding and phase encoding.

To select an imaging slice though the body, a magnetic gradient is added along the main magnetic field in the caudal to cranial direction. Because the frequency of precession, and thus the frequency at which the spins can be excited, is dependent on the local strength of the magnetic field, a narrow band of frequencies will only excite a thin slice (3 to 8 mm [34]) of spins through the body. With a change in the excitation frequency another parallel slice can be acquired later. To obtain slices in other directions, for example vertical slices, the direction of gradients for the slice encoding are altered to an anterior-posterior gradient. By using combinations of gradients in all three directions, it is possible to acquire a slice in any arbitrary direction through the body.

The frequency and phase encoding are used to obtain information for the individual points within a slice, the picture elements or pixels. For the phase encoding, a short temporary change in the magnetic field is applied between the RF excitation pulse and the readout of the signal. This change in the magnetic field will influence the frequency of precessing, resulting in a shift in the phase of precessing of the spins dependent on

the duration of this gradient switch. By repeating this process with different duration of the temporary gradients, signals with a different phase encoding are acquired.

The frequency encoding is used to differentiate pixels with the same phase encoding. A magnetic gradient during readout of the signal results in a specific shift of the resonance frequency, likewise the effect of the slice-encoding gradient, for pixels with the same phase shift.

Combining phase and frequency information allows the creation of a grid in which each pixel has a defined combination of phase and frequency codes. This grid of raw data is called the K-space. With a Fast Fourier Transform, the raw data, which represent an amplitude as a function of time, are transformed into a curve that represents an amplitude as function of the frequency. The amplitude of each frequency represents the intensity of each pixel. The Fourier Transform is performed in both the frequency and phase encoding direction. Important to realize is that the imaging time for a single image depends on the number of image lines desired, which is directly related to the number of signals with different phase shift that have to be acquired [36].

1.2.1.3 Spin-Echo imaging

There are several reasons why the FID signal is not used for clinical imaging. First there is a certain time necessary to perform the spatial encoding, and even with present ultra-fast MR scanners this cannot be performed before the FID declines. Second, the creation of a second AC signal gives opportunities to modify the contrast in the images depending on the T_1 and T_2 values of the tissues. To evoke a second AC signal, a second RF pulse is applied that flips the spin by 180° also reversing the dephasing process (Fig. 1.5). As the spins rephase, the amplitude of the AC signal increases and this signal, called the echo signal, is measured at its maximum (time of echo TE). MR techniques using the combination of a 90° and a 180° RF pulse to generate an echo signal are called spin-echo sequences.

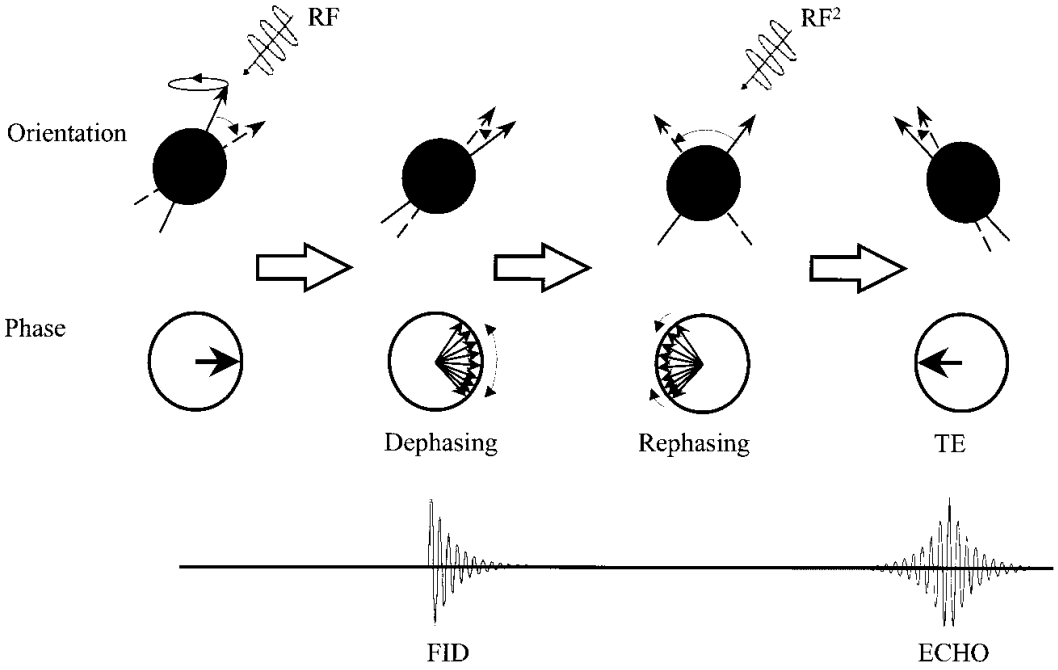

Figure 1.5: Mechanism of generation of the echo signal.

1.2.2 Contrast-enhancing agents

MRI contrast agents enhance image quality, as shown in Figure 1.6, by reducing the relaxation times of the nearby water protons and, consequently, changing the signal intensity of the water present in body tissues that contain the agent [37]. These contrast agents are commonly grouped in two main classes, according to their predominant effect: T_1 contrast agents which mainly shorten the relaxation time of the longitudinal magnetization and T_2 ones, which reduce the relaxation time of the transverse magnetization [33].

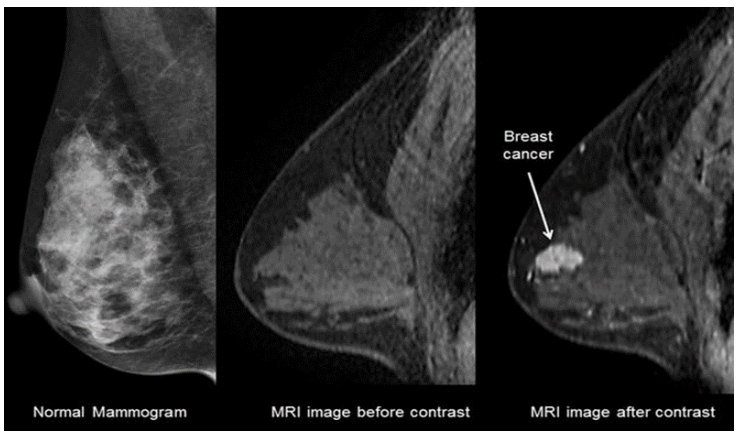

Figure 1.6: breast cancer imaged with (left) mammogram, (centre) MRI without contrast (right) MRI with contrast.

1.2.2.1 T_1 contrast agents

The longitudinal relaxation reflects a thermal loss from the spin system to its surroundings (lattice). Positive contrast agents reduce the T_1 and create bright contrast. The major advantage of such agents is positive imaging by enhancing the signal. The magnetization of paramagnetic materials, such as gadolinium complexes, is directly dependent on the ion unpaired electrons and the number of ions, and they have no magnetization in the absence of an external magnetic field.

Paramagnetic metal ions are widely used in conventional clinical practice, such as $Fe^{3+}, Mn^{2+}, Gd^{3+}$. The main problem with paramagnetic heavy metal ions in their native form is their toxicity. Both the metal ion and the ligand tend to exhibit substantial toxicity in the unbound state [38]. Slower clearance from the body is likely to significantly increase the toxicity of any Gd^{3+} complex [37]. Consequently, the interest for searching and studying new and safer alternatives has arisen.

Bailey et al. [39] have reported the fabrication of RE_2O_3-based nanodiscs, with diameters ranging from 10 to 14 nm; RE stands for Gd, dysprosium (Dy) or ytterbium (Yb) passivated with a biocompatible polymer (Poly(acrylicacid) grafted with short methoxy-terminated polyethylene oxides). Their suitability as MRI contrast agents has been analysed. The relaxation times of such nanostructures, measured at 37 °C (body temperature) in a magnetic field of 1.41 T, have been compared to the reported values for their spherical counterparts or small molecule chelates, based on pentetic acid (DTPA) ligand. The authors also performed an MR scan of a phantom for all the considered contrast agents, using T_1 weighted sequences. It has been found that Gd_2O_3 nanodiscs are more suitable as contrast agents compared to the commercially available Gd-DTPA, because of their higher relaxivities (the change in the relaxation rate normalized to the concentration of the contrast agent, per particle [40]). This factor should increase the efficiency of *in vivo* targeted imaging schemes, since it becomes possible to get a high amount of proton relaxation without requiring multiple small molecules in contact with the imaging target. Besides this benefit, it has been verified that these Gd_2O_3 nanodiscs are suitable as T_1 contrast agents. Also, no significant cytotoxic effects have been observed for the polymer coated Gd_2O_3 and Dy_2O_3 nanoarchitectures, on a cell line derived from human from cervical cancer cells (HeLa).

Singh et al. [41] also reports the suitability of polyethylene glycol (PEG) coated Gd_2O_3 paramagnetic nanodiscs and PEG coated Gd doped iron oxide (GdIO) superparamagnetic cubic/spherical-shaped nanoparticles, with different dimensions, as MRI contrast agents. In this case, the relaxivities of the different nanoarchitectures were

measured with a 7 T MR scanner and it has been showed that smaller sized nanostructures (<5 nm) have resulted in the more effective T_1 contrast agents, as can be seen from figure 1.7

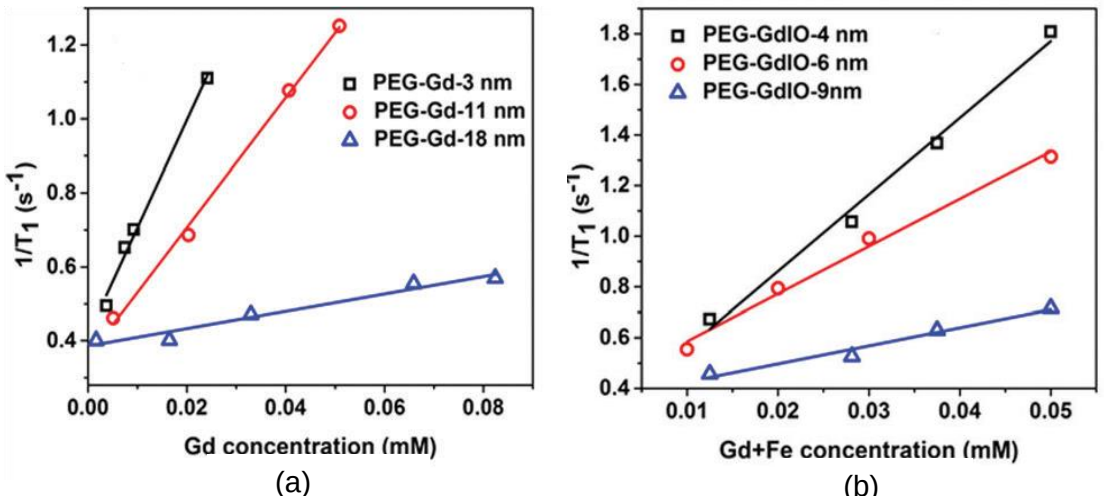

Figure 1.7: T1 relaxation rate as a function of concentration measured for (a) Gd2O3 nanodiscs of different diameters and (b) GdIO NPs of spherical (9 nm and 6 nm) and cubic (4 nm) shapes [41].

A report by Corr et al. [42] have addressed suspensions of linear chains of magnetite NPs, produced by the cross-linking of surrounding particles with polyelectrolyte molecules for biomedical application. Through the application of an external magnetic field, it has been verified that these nanostructures have rearranged into parallel arrays. The relaxivity has been measured using field-cycling NMR at 37 °C and a considerable reduction in the relaxation times at all the considered fields has been observed. The authors have also acquired MR images of live rats, injected with these nanoarchitectures, to assess their effect on the brain. The obtained results have proved that these nanoarchitectures have good biocompatibility and can be employed as contrast agents for *in vivo* MRI, having darkened the brain regions in a T_1-weighted image, as shown in Figure 1.8.

More recently, antiferromagnetic nanoarchitectures have also been investigated as potential T_1 contrast agents by different authors. Namely, Na et al. [43] have fabricated antiferromagnetic MnO nanoparticles of different sizes between 7 and 25 nm, coated with a PEG-phospholipid shell. The relaxivity of such particles has been measured in a 3.0 T human clinical scanner and their *in vivo* performance as MRI contrast agents have been analysed on a mouse. The obtained results indicate that these nanoparticles are suitable as T1 contrast agents, having demonstrated no significant toxicity, for a MnO concentration of less than 0.82 mM, in eight human cell lines originating from different

tissues. Furthermore, by conjugating them with a tumour-specific antibody, it has been possible to selectively improve the contrast of breast cancer cells located in a mouse's metastatic brain tumour, which has been intravenously injected with the functionalized nanoparticles through T_1-weighted MRI.

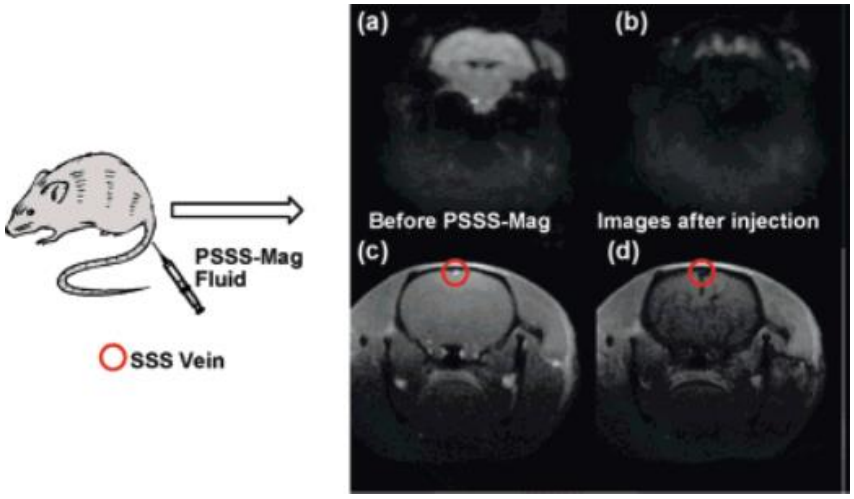

Figure 1.8: Echo planar image (EPI) of mouse brain (a) before and (b) as PSSS-Mag1(Fe/Polysodium-4-styrene sulfonate ratio 1:2) passes through; Fast Low Angle Shot (FLASH) image of mouse brain (c) before and (d) as PSSS-Mag1 passes through [42].

Neves et al. [44] have also addressed MnO nanoparticles (average size of ~ 20 nm); the difference relies in the coating: carboxymethyl-dextran has been used and the *in vivo* study have not been performed. Nevertheless, the authors have considered such nanostructures adequate as T_1 contrast agents, due to the significant longitudinal relaxivity measured on a clinical 3.0 T MRI scanner. Moreover, it has been observed that such nanoparticles present no *in vitro* cytotoxicity for healthy cells at concentrations lower than 25 µg/ml, however for HeLa cells there have been observed a notable toxicity even at low concentrations of nanoparticles (5 µg/ml).

On a different work, Peng et al. [45] have investigated another T_1 contrast agents, known as antiferromagnetic-iron oxide-hydroxide nanocolloids, with a diameter of 2-3 nm; such nanostructures have been prepared in the mesopores of worm-like mesoporous silica. The relaxation times have been measured at 40 °C using a 0.47 T Minispec spectrometer and have indicated that these nanoparticles had the lowest T_2 relaxivity/T_1 relaxivity ratio reported, until 2013, for iron-based colloidal T_1 contrast agents and possess a considerably high longitudinal relaxivity. Additionally, the acquired MR images have shown that such nanocolloids are a superior T_1 contrast agent in both *in vitro* (HeLa cells) and *in vivo* (rat and mouse) MRI, when compared to ultrasmall iron

oxide nanoparticles. Furthermore, these nanocolloids also demonstrated a high level of biocompatibility and biodegradability.

1.2.2.2 T_2 contrast agents

In this context, superparamagnetic iron oxides nanoparticles (SPIO-NPs) have been developed as a viable alternative to the Gd^{3+}-complexes. These nanostructures have various advantages, such as biocompatibility, ability to be metabolized, relatively high saturation magnetic moments and easiness of surface functionalization [8].

Nevertheless, the dimension of such nanoparticles is restricted by the superparamagnetic limit, which implies a maximum diameter of per particle in order to maintain zero remanence, fundamental property which prevents particles' aggregation in absence of magnetic field; for this reason, the magnetic moment of each particle is limited and, the ideal particle size for T_2 MRI contrasts agents (20 nm [46]) surpasses the superparamagnetic limit [3].

To overcome the problem of small magnetic moments of SP-NPs, several authors have studied various alternatives namely high aspect-ratio ferromagnetic NPs and SAF nanostructures.

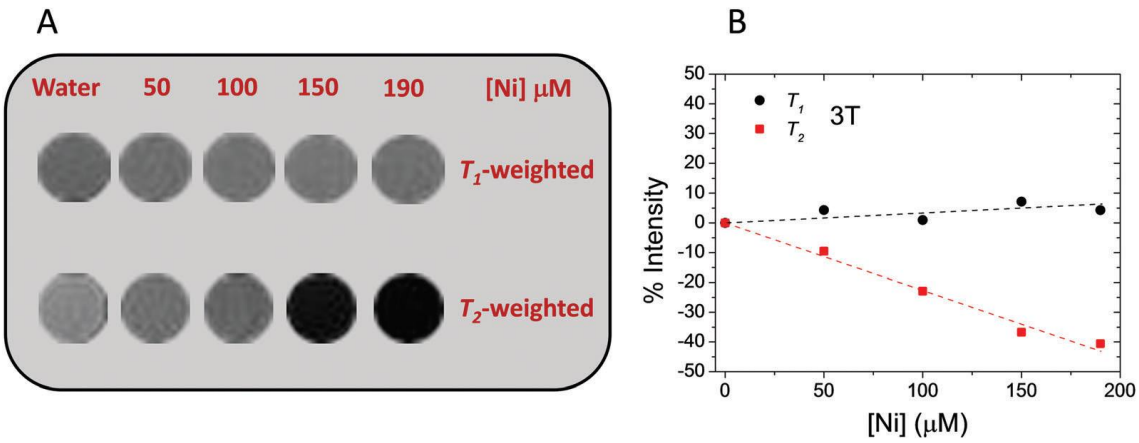

Figure 1.9: (A) Phantom image acquired under both T1- and T2-weighted sequences at 3 T and 37 1C. (B) MRI signal intensity (%) relative to the water control. Dotted lines are a guide for the eye [1].

Nanowires have also been addressed by some reports in the context of this biomedical application. Bañobre-López et al. [1] evaluated the relaxivity properties of poly-acrylic acid (PAA)-coated Ni ferromagnetic NWs characterized by longitudinal magnetic anisotropy, in a colloidally stable water dispersion. This dispersion has been produced through a process of pulsed electrodeposition of Ni/Gold (Au) multilayer nanowires inside a porous alumina at room-temperature, followed by the template

removal and chemical etching of the Au layer in a two-step acidic etching. The relaxation times of these nanostructures, which have presented a monodisperse average diameter and length of ~36 nm and ~600 nm, respectively, have been measured using a relaxometer operated at 60 MHz and 37 °C for two magnetic fields, namely 1.41 T and 3 T. In both situations, the obtained results indicate that these nanostructures are efficient as T_2 contrast agents, as clearly visible in Figure 1.9. The contrast effect of the PAA-coated Ni nanowires has been verified by performing an MR scan of a phantom at a magnetic field of 3 T.

Shore et al. [2] have also studied nanowires for this specific application. Fe and segmented Fe/Au nanowires have been fabricated by template-assisted electrodeposition with various lengths and diameters. These nanostructures have been coated with compounds, namely Dop-PEG and/or SH-PEG-COOH, which allow the binding of biological molecules to the nanowires in order to target specific cells. The magnetic characterization of both nanostructures has shown that the Fe/Au nanowires exhibit a larger saturation magnetization, due to the fact that their Fe layers are thinner than the diameter of the nanostructures, allowing them to be more easily magnetized in the direction perpendicular to the long axis of the nanoarchitecture, when compared to the Fe nanowires. The relaxivity properties of the nanowires have been measured at 25 °C in a 1.5 T magnetic field and compared with Fe and Fe-Au nanoparticles' ones. It has been verified that the Fe nanowires with a length of 0.7 μm and a diameter of 110 nm, coated with Dop-PEG, are best suited as T_1 contrast agent. On the other hand, Fe-Au nanowires with a length of 1 μm and a diameter of 32.8 nm, coated with SH-PEG-COOH and Dop-PEG, were the most appropriate as T_2 contrast agents, being comparable to commercial Fe oxide nanoparticles. The authors have also performed an MR scan of some samples containing Fe and Fe-Au nanowires, at a magnetic field of 9.4 T, in order to confirm the contrast caused by the nanostructures in the image.

In addition to the previously addressed nanoarchitectures, SAF nanostructures have also been studied as potential contrast agents for MRI. Roosbroeck et al. [13] have fabricated phospholipid-coated, disc-shaped and multilayered [Au(10 nm)/Ni80Fe(5 nm)20/Au(2.5 nm)/Ni80Fe(5 nm)20/Au(10 nm)] SAF nanoarchitectures, with diameters ranging from 89.8 nm to 523.2 nm, using a colloidal lithography technique. The magnetic characterization of these nanodiscs have indicated a very low remanence value, which is necessary for particles to do not agglomerate, as well as a high magnetization, making them adequate for biomedical applications. Then, these nanostructures have been evaluated as T_2 contrast agents, as reported in Figure 1.10, having shown improved

relaxivities, at 24.85 °C in a 9.4 T magnetic field, when compared to the SPIO-NPs, especially the smallest particles with a diameter of 90 nm. The authors also carried out an *in vitro* MRI study, using an ovarian cancer cell line (SKOV3), confirming the increased T_2 relaxation for cells marked with such nanostructures.

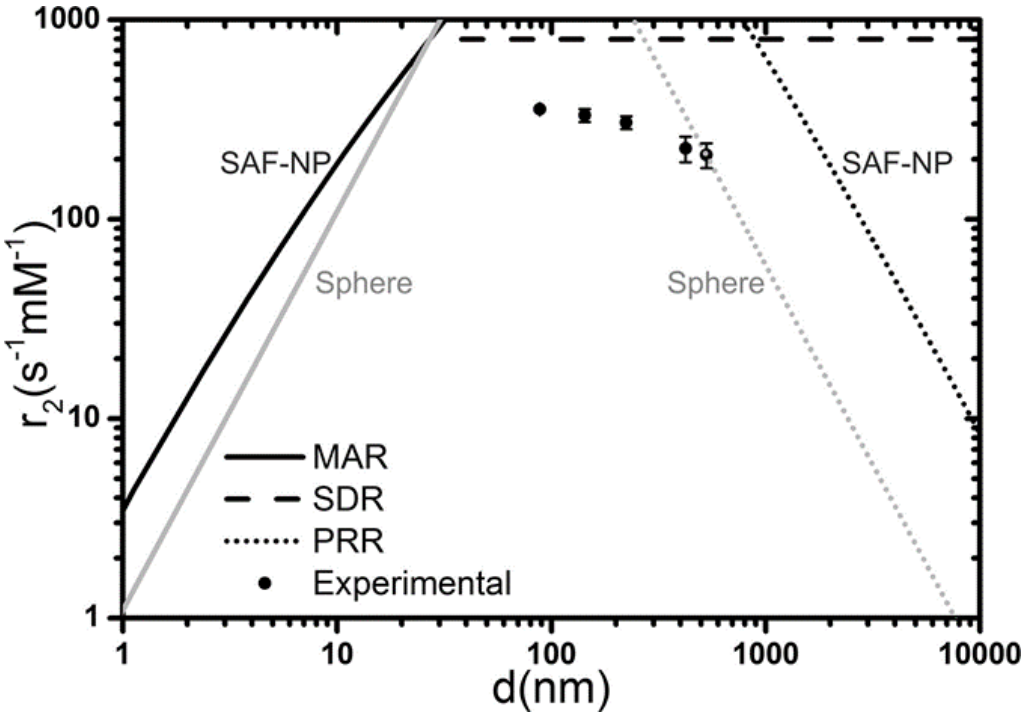

Figure 1.10: Theoretical (black lines) and measured (points) r2 values of [Au(10 nm)/NiFe(10 nm)/Au(2.5 nm)/NiFe(10 nm)/Au(10 nm)] SAF-NPs as function of SAF-NP diameter. The reference theoretical values for spherical NiFe particles [13].

1.3 Magnetic nanostructures

In the previous sections, the most common types of magnetic nanoparticles and applications have been briefly described. In the current one, the focus is put on the fabrication and characterization of two different types of magnetic nanostructures: Synthetic antiferromagnetic nanoparticles (SAF-NPs) and high aspect-ratio ones, namely nanowires.

1.3.1 Synthetic antiferromagnetic nanostructures

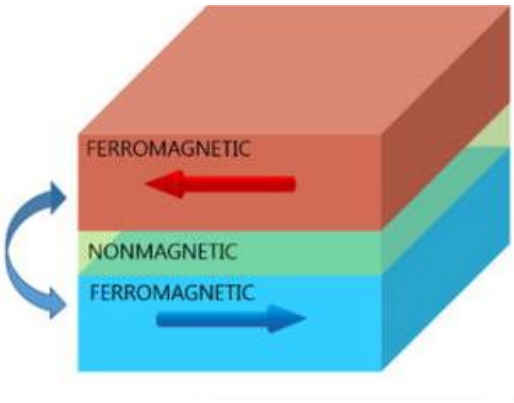

Figure 1.11: Schematic representation of antiferromagnetic structure.

Biomedical applications of MNPs impose several requirements. Structurally, they should be uniform in shape, size and composition [47]. In general, size uniformity is defined by 'monodispersity'. Particles are considered monodisperse in size if the variation is lower than 10% [18].

The control of particle dimension is achieved through appropriate manipulation of factors such as choice of surfactants, their ratios with reagent chemicals, reaction rates and temperature [47]. However, there are several limitations in MNPs using such techniques. Firstly, their dimensions tend to be log-distributed with large variations in the diameter. Secondly, their size need to be constrained to <20 nm in diameter (~12nm for Fe) [48] because it is only at this length scale that the superparamagnetic behaviour is achieved, allowing NPs to have negligible remanence field. Owing to their small volume, the resulting magnetic moments of these nanoparticles, typically iron oxides nanospheres, tend to be too low. To overcome this problem, some methods have been developed [49]. However, there are still limitations associated with controlling monodispersity, magnetic response and variation in size [50].

SAFs are a novel type of magnetic nanoparticles; their structure consists mainly in two ferromagnetic layers separated by a nonmagnetic one (Figure 1.11). The nomenclature of 'synthetic anti-ferromagnetics' refers to the anti-parallel alignment of the ferromagnetic layers, which then results in the near zero remanence at low fields [47]. The coupling between the two ferromagnetic layers can be of two forms: magnetostatic or by interlayer exchange coupling. The first one strongly depends on the aspect ratio of the structure, while the second one depends on the material and the number of atomic layers [51]; Moreover and an oscillatory dependence on the thickness of the spacer has been find out as well [52].

SAFs are nanostructures optimized to have negligible remanence, low susceptibility around zero field and a distinct, tunable, switch to full magnetization, which allows high saturation magnetization values at low applied fields [47]. These magnetic properties make the SAFs promising nanoparticles for several medical applications, in particular as image contrast agents in MRI.

1.3.1.1 Fabrication methods and materials

SAF-NPs usable for biological application have been recently developed using top-down approaches. Table 1.1 summarizes the main techniques and materials used for this proposal.

Ref.	Fabrication technique	Stabily layer	Ferromagnetic layer	Nonmagnetic spacer	Diameter(nm)
[47]	Nanoimprint lithography	Ta	$Co_{90}Fe_{10}$	Ru	~120
[50] [49]	Nanoimprint lithography	Ta	$Co_{90}Fe_{10}$	Ru	~120
[6]	Lithography*	Ta	CoFeB/Pt	Ru	~2000
[13]	Colloidal lithography	Au	$Ni_{80}Fe_{20}$	Au	~60/110/200/500
[53]	*	*	NiFe	Ru	~120

Table 1.1: Fabrication techniques and materials reported in literature about SAF-NPs. (*) not specified.

The most suitable techniques to fabricate such nanostructures are nanoimprint lithography, direct deposition of multilayer films and retrieval in liquid phase via an ‘etching’ release process. Such physical fabrication methods enable accurate control of particle shape, size and composition; since the use of nanoimprint lithography techniques for particle fabrication deviates significantly from conventional chemical synthesis methods, it has been postulated that the parameters affecting the structural and magnetic properties of the SAFs will be affected by different parameters compared to MNPs synthesized by wet chemistry [47]. Thus, different materials and thicknesses of the layers have been investigated, in order to achieve the desired properties.

The process of nanoimprint lithography is briefly described in Figure 1.12 adapted from [47].

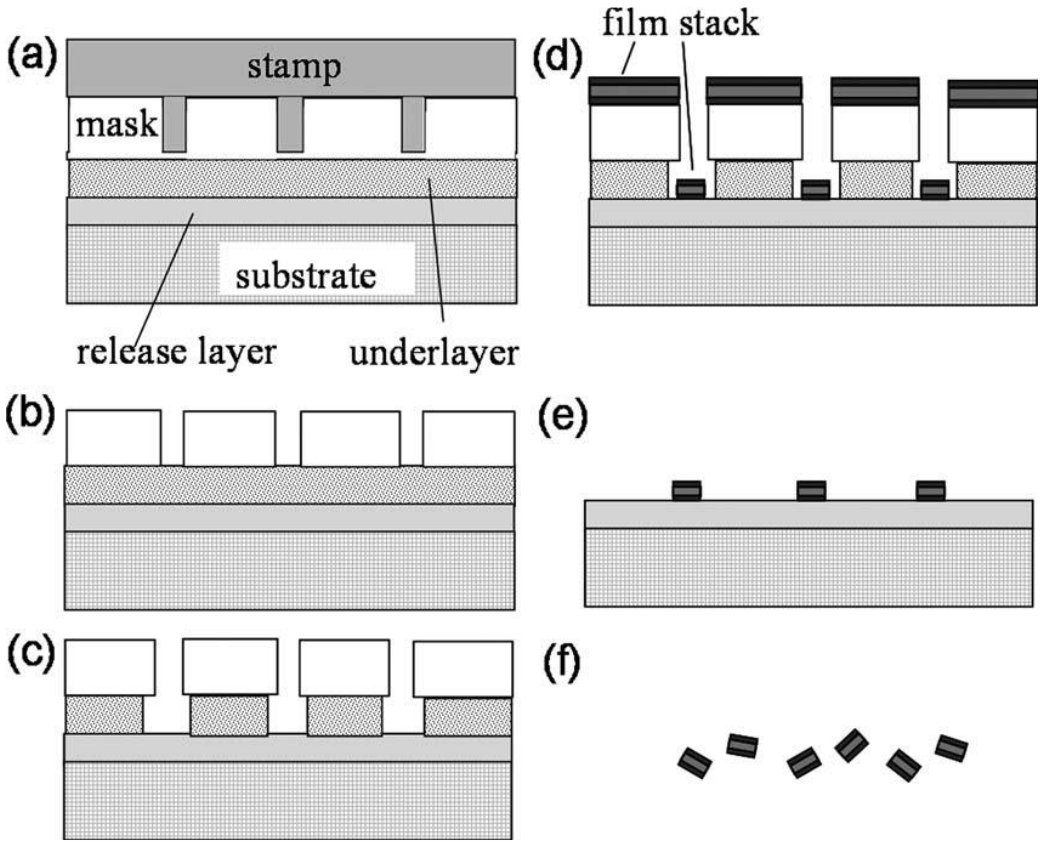

Figure 1.12: NIL process (a) template formation by nanoimprint lithography, (b) residue layer removal by O2 plasma, (c) undercut profile creation in the underlayer resist, (d) metal film deposition, and (e) lift-off followed by (f) chemical etching.

A. L. Koh et. al [47] has reported the fabrication of disk-shaped $Co_{90}Fe_{10}$ nanostructures with subsequent characterization; a similar study has been carried out in Hu et. al [50] and Hu et. al [49]. In both cases, the diameter of the nanostructures is about 120nm. The common point of the works is the study of the magnetic behaviour by varying the thickness of the ferromagnetic layers. The main differences rely on the focus; in the first case the authors have put particularly attention on the composition of release layer and in the magnetic properties before, after the ion milling process and subsequent release in aqueous solution; in the second one variations of the nonmagnetic layer have been investigated, after release of the sacrificial layer, with particular attention in the behaviour of the magnetic susceptibility, which can be tuned by exploiting interlayer magnetic interactions [50]. The obtained stacks are reported in the tables below, Table 1.2 and 1.3 respectively, where thicknesses are expressed in angstrom (Å).

Ref. [47]	Ta	R. layer	Ta Buffer	Ru	$Co_{90}Fe_{10}$	Ru	$Co_{90}Fe_{10}$	Ru	Ta
Effect of the	20	Cu 500	70	22	120	25	120	24	170
ion milling	20	Cu 500	-	22	120	25	120	24	100
process	20	-	-	22	120	25	120	24	100
Effect	30	Cu 500	70	20	120	25	120	20	70
of the	30	CuOx 500	70	20	120	25	120	20	70
release	40	-	-	20	120	25	120	20	70
layer and	30	Cu 500	70	20	60	25	60	20	70
ferromagetic	30	CuOx 500	70	20	60	25	60	20	70
thickness	40	-	-	20	60	25	60	20	70

Table 1.2: Thicknesses and materials of the deposited stacks by A. L. Koh et. al [47].

Ref. [49] [50]	Ta	Ru	$Co_{90}Fe_{10}$	Ru	$Co_{90}Fe_{10}$	Ru	Ta
Effect of thickness variation of ferromagnetic layers	50	20	120	25	120	20	50
	50	20	60	25	60	20	50
	50	20	30	25	30	20	50
Effect of thickness variation of spacer layer	50	20	60	25	60	20	50
	50	20	60	6	60	20	50
effect of the increase in number of interfaces	50	20	[30/6]x3		30	20	50

Table 1.3: Thicknesses and materials of the deposited stacks by Hu et. al [49, 50].

Besides the fabrication of CoFe disk shaped nanostructures, others ferromagnetic materials have been investigated, such as CoFeB/Pt and Ni-Fe.

Velmulkar et. al [6] have successfully demonstrated the transfer of magnetic properties from ultrathin perpendicularly magnetized CoFeB/Pt films antiferromagnetically coupled through RKKY interaction using Ru interlayers, to lithographically defined 2µm particles which have been lift-off into solution. The structure has been optimized to obtain a zero-magnetization remanence state, low magnetic susceptibility at low applied fields, a sharp switch to full magnetization at a desired applied field, and the ability to vary the total magnetic moment without affecting any of these characteristics. The motif of the magnetic multilayer stack used consists of Ta(20)/Pt(20)/CoFeB(9)/Pt(2.5)/Ru(9)/Pt(2.5)/CoFeB(9)/Pt(20), with thicknesses in Å; it has been demonstrated that by stacking multiple repeats of the blocks (12 in this case) the magnetic moment is maximized. The Ta(20)/Pt(20) buffer layers are included for each repeated bilayer system and are crucial in decoupling consecutive blocks, and therefore obtaining a field response that is similar to a single building block. The amorphous Ta layers also minimize the degradation of growth properties higher up the stack, which is crucial in synthetic antiferromagnetic nanoparticles.

Van Roosbroeck et. al [13] have presented the top-down synthesis of a novel type of MRI contrast agents with great control over size and shape using a colloidal lithography technique. A schematic overview of the standard fabrication procedure is presented and briefly described in Figure 1.13.

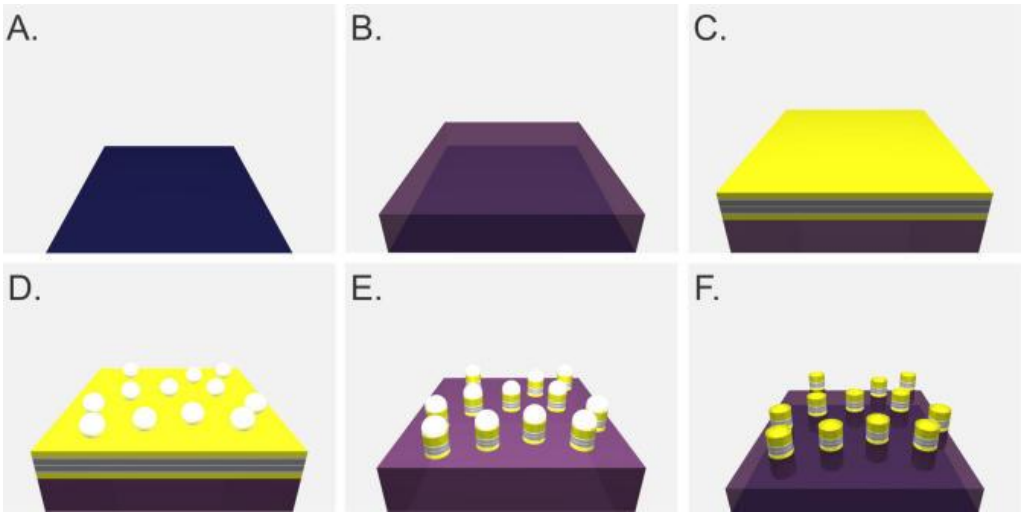

Figure 1.13: Colloidal lithography schematics. (A) blank wafer, (B) photoresist coating, (C) sputtered magnetic stack, (D) polystyrene beads drop casted, (D) ion milling, (E) SAF creation, (F) removal of beads.

The particles consists of Au(100)/$Ni_{80}Fe_{20}$(50)/Au(25)/ $Ni_{80}Fe_{20}$(50)/Au(100) layered structures and have been fabricated using different PS-bead masks of (60,110,200,500) nm, as presented in Figure 1.14. Post synthesis the mean diameter has been measured using ImageJ program; due to the slope that is created during the ion milling process, the diameters have shown an increase of ~20-30 nm compared to the original, nominal bead size. The synthesised particles have been suspended in 2-propanol and coated with 1,2-distearoyl-sn-glycero-3-phosphoethanolamine-N-[carboxy(polyethylene glycol)-2000], in order to achieve a stable colloidal suspension. The average diameter has shown an increase of 50-60 nm for all particle suspensions.

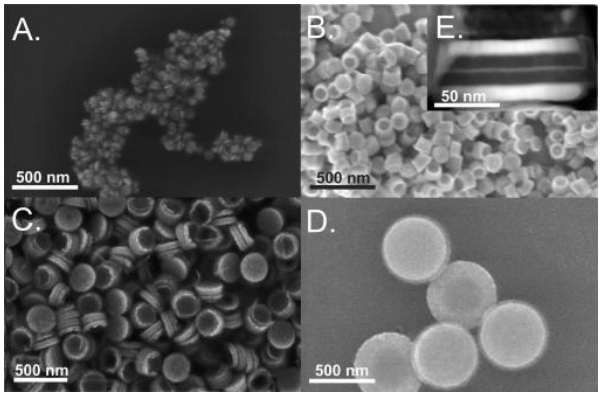

Figure 1.14: (A-D) SEM-images of SAF-NPs fabricated using (A) 60 nm, (B) 110 nm, (C) 200 nm, and (D) 500 nm polystyrene bead masks. (E) HAADF-STEM-image of a 110 nm diameter SAF-NP. Two NiFe layers (dark), separated by a gold spacer (bright) [13].

Courcier et. al [53] have also presented SAFs with NiFe as ferromagnetic layers. The diameter is ~120nm and the composition is the following, with thicknesses expressed in Å: [NiFe(100)/Ru(6)]x11/NiFe(100). In this study, various modes of SAF-NPs displacement in solution have been investigated, under application of various types of magnetic fields: uniform or exhibiting a gradient, constant or variable, and alternating along one axis or rotating in plane. The experimental results have shown that controlling the motion of the magnetic particles chains with a rotating magnetic field allows a much more effective action than a field gradient. Furthermore, this action is enabled over a longer range. In comparison with particle motion induced by magnetic field gradient, the tumbling motion is particularly advantageous for applications where the biological environment is relatively far from the magnetic field sources (for example for body internal organs). In addition, the more effective action exerted on these particles allows them to move faster, or in more viscous solution, or to transport biological or chemical species of larger volume than conventional particles can do in field gradients. In addition,

the combination of rotational and translational motion may be used to increase the capture cross section of these particles for instance for diagnostic purposes.

1.3.1.2 Physical characterization

As previously discussed, a crucial property for biological application is the zero magnetization remanence state, which prevent particles from agglomeration through the interaction of their magnetic moments, thus maintaining the stability of the particles when dispersed in solution; a low susceptibility at low fields is also desired, as a high one may lead to particles staying agglomerated once the applied field is removed. Moreover, a sharp switch to full magnetization at a desired applied field would allow efficient access to the saturation moment of the particle.

From these considerations, is possible to predict the shape of the hysteresis loop of an ideal particle, which is shown in figure 1.15 a.

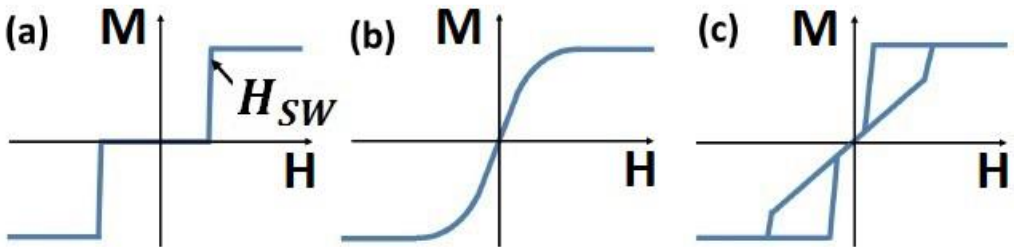

Figure 1.15: (a) Hysteresis loop of an ideal SAF particle. (b) hysteresis loop of a superparamagnetic particle. (c) hysteresis loop of a vortex-state particle.

The horizontal line at zero magnetization and passes through zero applied field ensures both the zero-remanence state as well as the negligible low field susceptibility (Figure 1.15 a). The figure also shows the curves of typical hysteresis loops for two commonly used particles for biomedical applications: superparamagnetic nanoparticles (figure 1.15 b) and magnetic vortex state nanodiscs (figure 1.15 c). The first ones have been widely used, particularly in cancer therapy, magnetic hyperthermia and contrast agents in MRI, as previously explained; these particles have zero moment at zero field, but, as limited in size due to the superparamagnetic regime, have quite low value of the saturation magnetization [11]. The second ones, have been recently considered suitable for applications such as drug targeting, magnetic fluid hyperthermia and magneto-mechanically induced cell damage [12]; these vortex state nanostructures display zero remanence as well, but have larger susceptibilities around the zero field which can lead to irreversible agglomeration under applied field [54].

It has been shown that SAFs fulfil the desired key criteria, with a significant degree of control in the engineered magnetic parameters. A typical In-plane hysteresis loop for such particles is presented in Figure 1.16 [50]. Without an external magnetic field, the remanence of these nanoparticles is nearly zero, which indicates that the magnetization of the ferromagnetic layers, $Co_{90}Fe_{10}$ in this specific case, are anti-parallel and, thus, cancel out each other, as expected [48]. As an external field is gradually applied in the in-plane direction, this anti-parallel configuration is overcome and the magnetization starts to rotate towards the field orientation, resulting in a nearly increase of the net magnetization. Increasing the field strength, the magnetic moments are finally parallel and magnetic saturation is reached and is proportional to the magnetic layer thickness [48]. The slightly flatter region in the middle of the curve can be attributed to the spin flop and negative remanence phenomena [55].

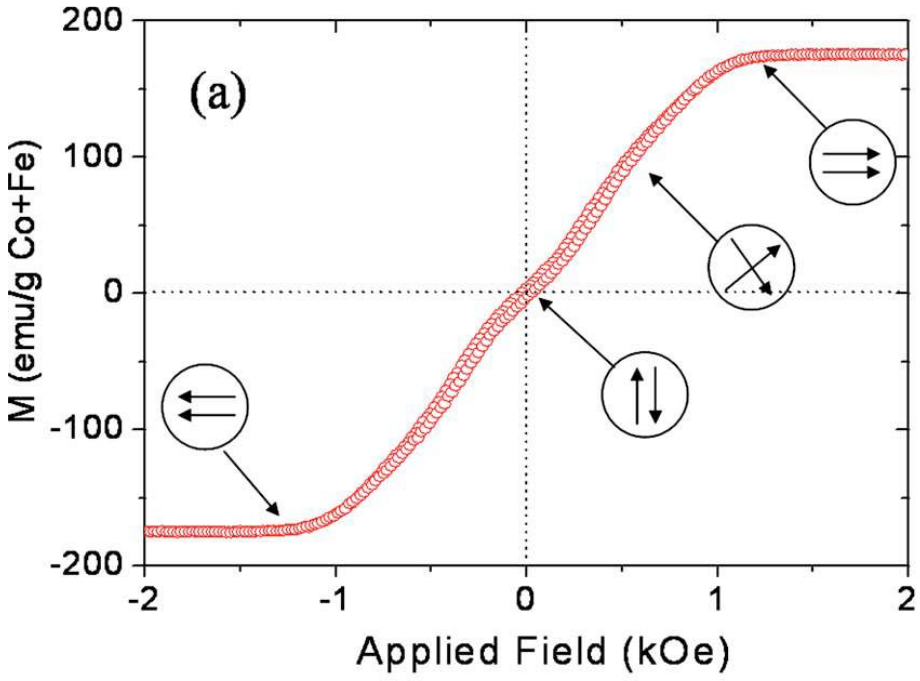

Figure 1.16: Typical hysteresis loop of a synthetic antiferromagnetic nanoparticle [47].

In A. L. Koh et. al [47], to examine possible differences in the structural and magnetic properties as a result of the additional release layer and ion milling, SAFs with structure Si(sub)/Ta(20)/Cu(500)/Ta(70)/Ru(22)/ $Co_{90}Fe_{10}$(120)/Ru(25)/ $Co_{90}Fe_{10}$(120)/Ru(24)/Ta (170) have been produced, where the numbers represent the nominal thickness of the layers in Å. It has been shown that after ion milling, the entire Ta buffer layer and part of the Cu release layer have been removed, exposing the Cu surface for the subsequent

chemical etch process. The final fabrication step has involved the etch of the Cu sacrificial layer and harvesting the SAF nanoparticles in water. The magnetic properties of the nanostructures and their changes before, after ion mill are shown in figure 1.17. The superimposition of the magnetic hysteresis loops before and after ion mill indicates a slight decrease in the magnetic moments after the ion mill process; this can be attributed to reduced Ta passivation leading to some oxidation of the ferromagnetic constituents [56]. Released SAFs in water typically show a reduction of the saturation field, due to increase interparticle interactions when dispersed in solution [47], but still retain low magnetic remanence when the external field is removed.

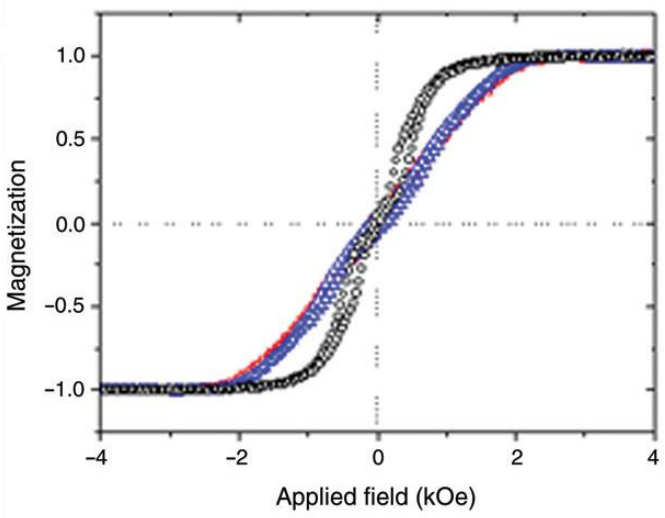

Figure 1.17: Magnetic hysteresis loops of substrate-bound SAF nanoparticles before ion mill (red), after ion mill (blue) and after release in aqueous solution (black) [47].

To investigate the effects of different release layers and ferromagnetic thicknesses on the SAFs' structural and magnetic properties, samples of Si/Ta(30)/Release(500)/Ta(70)/Ru(20)/ $Co_{90}Fe_{10}$ (t)/Ru(25)/ $Co_{90}Fe_{10}$ (t)/Ru(20)/Ta(70) have been fabricated, where release denotes either a Cu sacrificial layer or a Cu sacrificial layer with the introduction of 1.3×10^{-5} Torr of oxygen during its deposition, namely CuOx release layer; for the two types of release layer, the thicknesses of the ferromagnetic $Co_{90}Fe_{10}$ layers have also been varied, by setting t as 60 or 120. In addition, control samples of Si/Ta(40)/Ru(20)/ $Co_{90}Fe_{10}$(t)/Ru(25)/ $Co_{90}Fe_{10}$(t)/Ru(20)/Ta(70), where t=60,120 (figure 1.18 a, 1.18 b respectively), have been implemented. Thicknesses, again, are express in Å. As it can be seen from figure 1.18 the shapes of the hysteresis loops are similar to the one observed in figure 1.16. The changes in M-H loops for different samples are

insignificant regarding the quality of the curve; there is a significant change in quantity: The saturation field increases when the ferromagnetic thickness is doubled, as already expected [48].

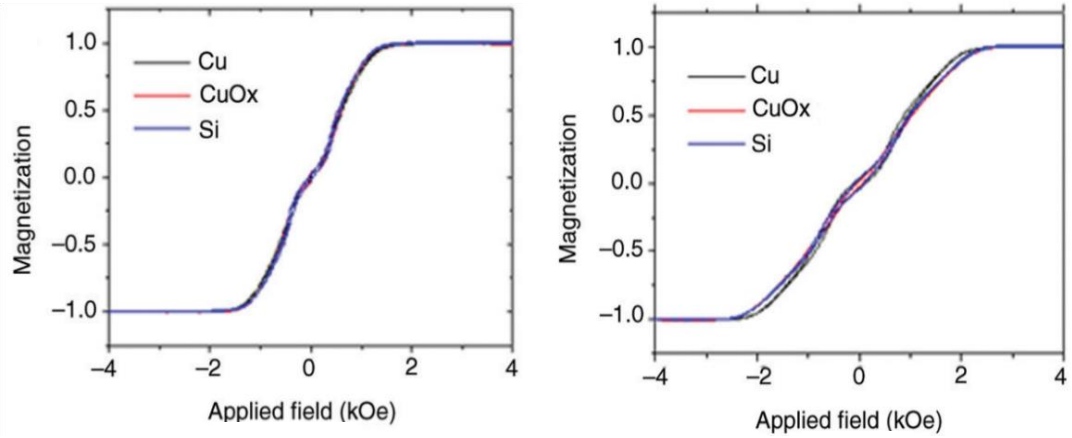

Figure 1.18: (Colour online) comparison of SAFs with different release layers (Cu, CuOx or none) with CoFe layers thicknesses of (a) 60 Å and (b) 120 Å [47].

Hu et. al [50, 49] have also been investigated the magnetic behaviour of disk shaped Co-Fe nanostructures; SAFs exhibit zero magnetic remanence, as previously presented, and adjustable magnetic properties over a wide range of sizes. These properties are controlled using interlayer magnetic interactions which depend on multilayer film structure and materials. The magnetic properties have been measured by alternating gradient magnetometry (AGM) at room temperature.

Firstly, the hysteresis loops of substrate-bound 120 nm diameter SAF-NPs have been examined [49]; The stacks' composition consist of Ta(50)/Ru(20)/ $Co_{90}Fe_{10}$(t)/Ru(25)/ $Co_{90}Fe_{10}$(t)/Ru(20)/Ta(50), for ferromagnetic bilayers thicknesses of t=30 Å (trace A), t=60 Å (trace B), and t=12 Å (trace C). The remanence and coercivity of these nanoparticles are nearly zero, as required in most biomedicals applications. The functional dependence of the magnetization M is $M(H) = M_s(\frac{H}{H_s})$, until M attains a constant value M_s when H reaches the saturation field H_s. M_s and H_s are both proportional to the magnetic bilayer thickness because interlayer magnetic repulsion increases linearly with the thickness of the ferromagnetic layer, as expected from considerations of the demagnetizing fields [48].

Secondly, the effect of different spacer thickness has been studied by the authors [49]. The effects on hysteresis loop can be included by considering the interfacial exchange coupling as producing an effective magnetic field which adds to, or subtracts from, the

magnetostatic demagnetizing field; this effect is quite pronounced for thin (<1nm) Ru spacer [57], which provide strong antiferromagnetic coupling and thus increase saturation.

Figure 1.19 shows the expected increase in saturation fields by changing the Ru spacer from 25 Å (trace A, Circles: Ta(5)/Ru(2)/CoFe(6)/Ru(2.5)/CoFe(6)/Ru(2)/Ta(5);) to 6 Å (trace B, Triangles: Ta(5)/Ru(2)/CoFe(6)/Ru(0.6)/CoFe(6)/Ru(2)/Ta(5)). In trace C (squares: Ta(5)/Ru(2)/[CoFe(3)/Ru(0.6)]3/CoFe(3)/Ru(2)/Ta(5), the subset of CoFe(30)/Ru(6) bilayer is repeated 3 times, maintaining the sum of the magnetic layer thickness the same; the saturation field is further increased in this case.

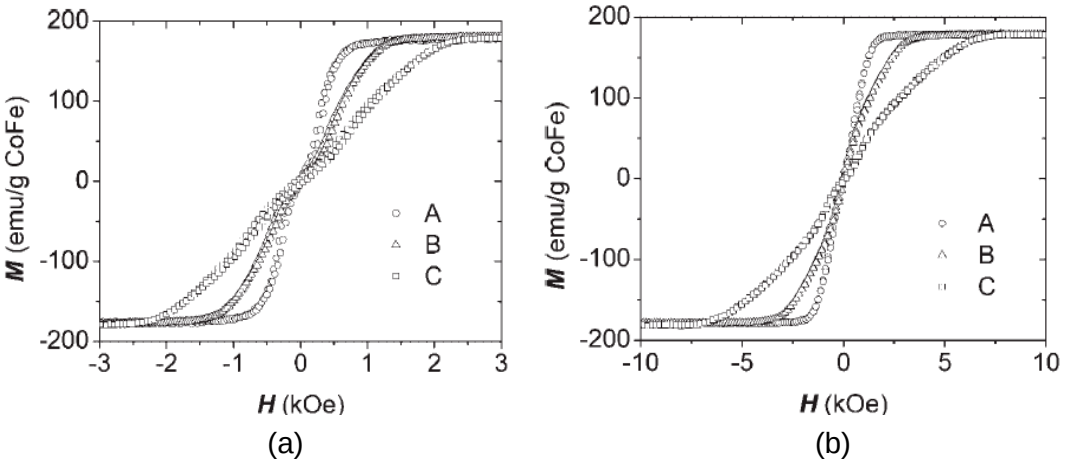

Figure 1.19: (a) Hysteresis loops for different thickness of the magnetic layer. Circle, triangle, and square curves represent t=30, 60, and 120 Å respectively. (b) Hysteresis loops for different thickness of the non-magnetic spacer. Adapted from [49]

Finally, the field dependence of magnetic susceptibility of three different SAFs, the same ones reported in the previous paragraph, have been investigated [50]. SAFs susceptibilities show a double peak, as can be seen in Figure 1.20. The valley of the susceptibility is due to a non-zero spin flop field, which causes the magnetization to deviate from linearity at small fields [58]. By controlling the interlayer magnetic interactions, the susceptibility of a SAF can be tuned over a wide range. For example, trace A (circles:Ta(50)/Ru(20)/CoFe(60)/Ru(25)/CoFe(60)/Ru(20)/Ta(50), total of 285 Å), represents a typical behaviour in presence of strong magnetostatic interactions between the two ferromagnetic layers, corresponding to Ru thickness of 25 Å. The susceptibility flattens by reducing the spacer layer thickness to 6 Å (trace B, triangles: Ta(50)/Ru(20)/CoFe(60)/Ru(6)/CoFe(60)/Ru(20)/Ta(50), total of 266 Å), where strong antiferromagnetic interlayer exchange coupling starts dominating. This effect can be further enhanced by increasing the number of interfaces and magnetic layer, as can be

seen from trace C (squares:Ta(50)/Ru(20)/[CoFe(30)/Ru(6)]x3/CoFe(30)/Ru(20)/Ta(50), total of 278 Å).

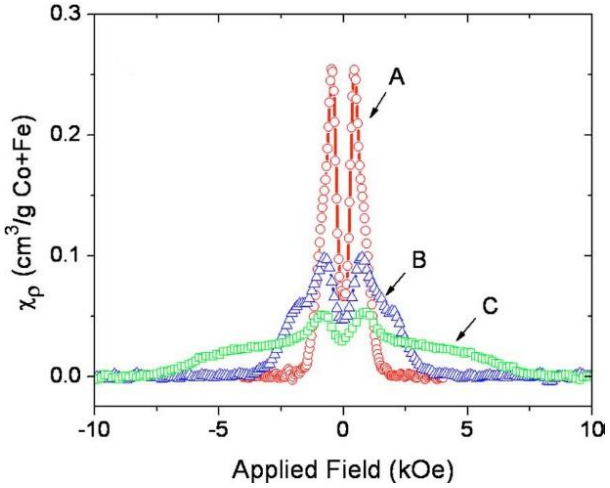

Figure 1.20: (Colour line) Susceptibility normalized by the mass of Co+Fe vs in-plane applied field. Adapted from [50].

Velmulkar et. al [6] have studied the transfer ability of desired magnetic properties to a bilayer system that is free to rotate under an applied field. The motif of the stack consists of Ta(20)/Pt(20)/CoFeB(9)/Pt(2.5)/Ru(9)/Pt(2.5)/CoFeB(9)/Pt(20), as shown in figure 1.21 a with thicknesses expressed in Å.

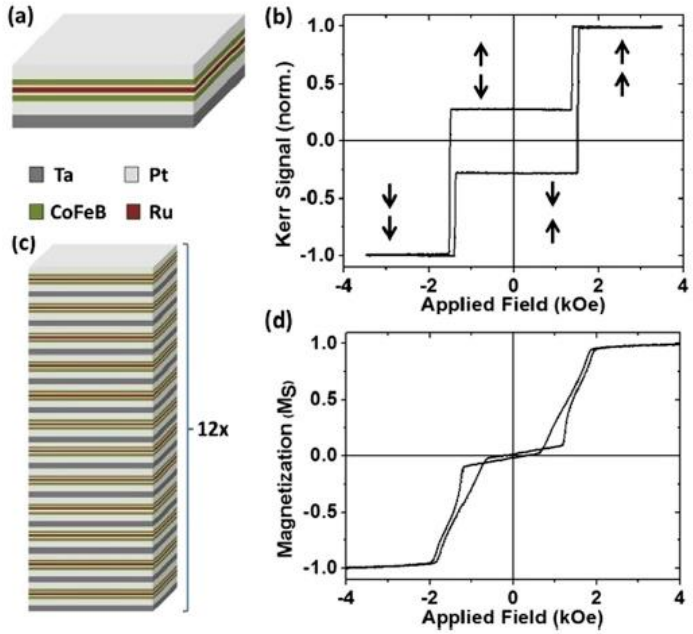

Figure 1.21: (a) The single coupled bilayer motif. (b) Polar MOKE of the single bilayer (c) The multilayer stack, where the basic motif is stacked 12 times. (d) VSM easy axis hysteresis loop of the 12-repeat motif multilayer stack [6].

The authors have stated that the Ru thickness has been chosen so because it relies on the first antiferromagnetically coupled peak [59]. In figure 1.20 b the single bilayer hysteresis loop is presented, where the field is applied parallel to the direction of the layer magnetizations; the direction is represented by the arrows. Here, the non-zero remanence is stated, by the authors, to the depth of the (polar) MOKE signal. Figure 1.20 d shows the field response of the stack of bilayers represented in 1.20 c, which is comparable with the one of the single bilayers. It has been shown that increasing the number of repetitions has not significantly changed the anisotropy in the layers but has caused the transition to saturation to occur more gradually.

Van Roosbroeck et. al [13] have proposed SAFs containing NiFe as ferromagnetic layers to be used as possible contrast agents in MRI, for instance. The coupling between the magnetic layers oscillates between the ferromagnetic and antiferromagnetic as a function of the spacer layer thickness. Figure 1.22 A shows the oscillation of the saturation field between ferromagnetic (at 0, 15, 30 Å) and antiferromagnetic behaviour (at 10, 25 Å) for a 222nm diameter SAF, consisting of 100 Å $Ni_{80}Fe_{20}$ separated by an Au layer.

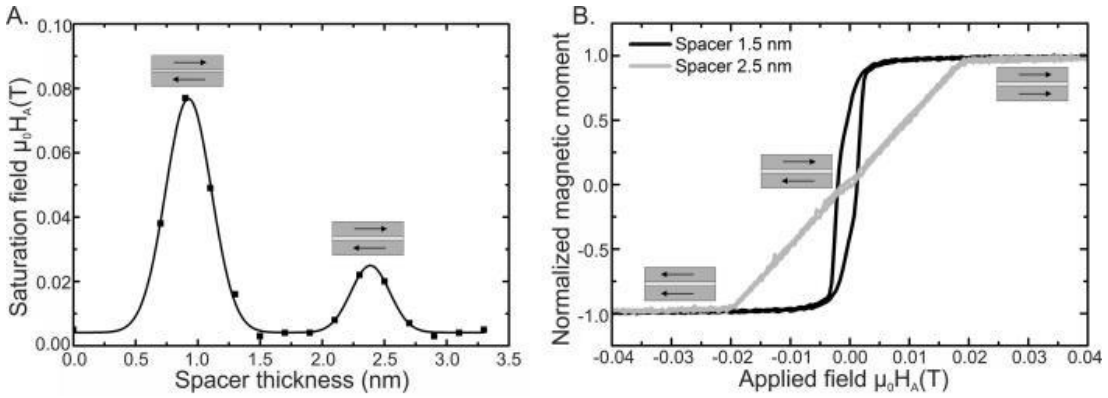

Figure 1.22: (A) Magnetic saturation field of SAF-NPs in function of the spacer thickness. (B) Magnetic hysteresis curves of 222 nm SAF-NPs [Au(100)/NiFe(100)/Au(x)/NiFe(100/Au(100)] with thicknesses in Å. [13]

Figure 1.22 B presents the magnetic hysteresis curves for typical ferromagnetic and antiferromagnetic spacer thicknesses, respectively at 15 and 25 Å. At 15 Å, the ferromagnetic coupling results in a high magnetic susceptibility because the two layers tend to align their magnetizations spontaneously to follow the applied field together. Increasing spacer thickness to 25 Å, lower susceptibilities are achievable, typical for the antiferromagnetic coupling; these nanoparticles show nearly zero magnetic remanence and coercivity. After lift-off and functionalization, the saturation magnetization has been determined using Superconducting Quantum Interference Device (SQUID)

magnetometry; it has been find out that the value is quite higher if compared with SPIO-NPs [60].

Courcier et. al [53] has also studied the behaviour of NiFe SAFs. It has been shown that particles do not agglomerate in zero field, since their susceptibility is lower than the critical value for self-polarization and agglomeration [61].

1.3.2 Magnetic nanowires

Recently, a considerable effort has been placed on the study of 1D nanostructures such as nanowires, nanopillars and nanoroads, owing to their unique applications. The term nanowires describe wires with large aspect ratio (length to diameter ratio), while nanopillars and nanoroads are nanostructures characterized by a smaller length. The unusual properties of nanowires originate from their high-density electronic states, diameter dependent band gap, enhanced surface scattering of electrons and photons, high surface to volume ratio and high aspect ratio [62]. In comparison with others low-dimensional systems, nanowires have two quantum-confined and one unconfined direction for electrical conduction and thermal transport. Moreover, nanowires with multiple segments along their length have tunable magnetic properties, such as the orientation of the magnetic easy axis, Curie temperature, coercivity, saturation field, saturation magnetization and remanence magnetization. Their magnetic properties can be modified by changing the diameter, chemical composition and thickness of the segmented layers. Nanowires are also widely used in nanomedicine, for example in accumulation of therapeutics (Figure 1.23), as they persist in circulation about ten times longer than the spherical ones [63].

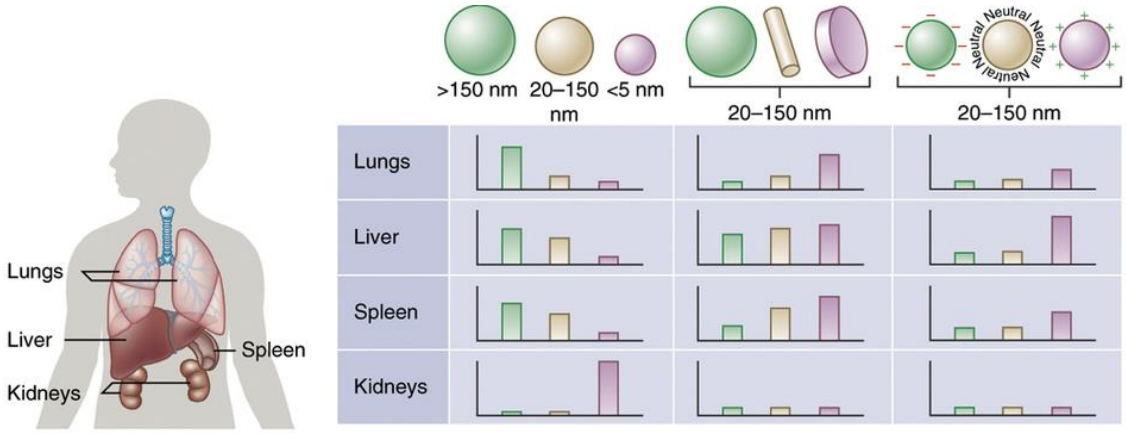

Figure 1.23:Nanoparticle size, shape and surface charge dictate biodistribution among the different organs including the lungs, liver, spleen and kidneys [63].

1.3.2.1 Fabrication methods and materials

Generally, the synthesis of nanowires can be divided int two main classes: Direct synthesis, where the morphology is controlled by tuning synthetic conditions or by using appropriate templates, and assembly methods [62]. For the purpose of this work, a brief description of nanoporous alumina template-assisted synthesis followed by electrodeposition is given.

Anodization of aluminium is cheap process for the synthesis of nm-scale porous structure, consisting in close packed cells in a local hexagonal arrangement, with pores at their centres. Hexagonally ordered patterns can be obtained by cycles of anodization and successive removal of the porous oxide. Such a method appears very promising in the production of hexagonal patterns with extended long-range order [64]. The combination of porous anodic alumina (PAA) templates with different deposition methods, sputtering or electrodeposition for instance, allows the fabrication of highly ordered nanostructures, such as NWs, nanotubes (NTs), nanodots or antidots [65].

Nanowires often appear as alternatives to the spherical particles, as this geometry translates into intrinsic anisotropy properties that cause them to interact differently [62]. They are characterized by increased surface to volume ratio and higher magnetic moments, originated from a prevalent shape anisotropy, which make them attractive in several areas of biomedical research. Magnetic nanowires, either segmented or not, and their magnetic properties have been widely investigated [66, 67, 68].

Several studies have been carried out in the last decades; Ni-based nanowires have been widely used, as well as Fe and Co based ones. The table below resumes different types of magnetic NWs suitable for biomedical applications, fabricated by assisted electrodeposition in porous anodic templates.

Ref.	L[Ni] (nm)	L[Fe] (nm)	L[Co] (nm)	L[Cu] (nm)	L[Au] (nm)	D (nm)	L[NW] (µm)	~L/D	name
[69]	-	-	40000	-	-	20	40	2000	Co NWs
			From 40000 to 500			100	From 40 to 0.5	From 400 to 5	
[70]	-	-	10000			35	10	286	Co NWs
			20000			500	20	40	
[70]	10000	-	-	-	-	35	10	286	Ni NWs
	20000					500	20	40	
[71]	22000	-	-	-	-	35	22	628	Ni NWs
						75		293	
[72]	1000	-	-	-	-	30	1	333	Ni NWs
						40		250	
						55		181	
[73]	1000	-	-	-	-	20	1	500	Ni NWs
	5000					40	5	125	
	15000					170	15	88	
[74]	100	-	-	10	-	170	55	323	NiCu NWs
	20			10			15	88	
	30			35			32.5	191	
[75]	-	30	-	15	-	45	0.54	12	FeCu NWs
				60			1.08	24	
				120			1.8	40	
[76]	20	-	-	25	-	50	13.5	270	NiCu NWs
	30						16.5	330	
	100			75			52.5	1050	
	140						64.5	1290	
[64]	-	-	64	-	-	25	0.064	2.5	Co NWs
			770				0.77	30	
[77]	-	-	5700 to 240	-	-	100	5.7 to 0.24	2.5 to 60	Co NWs
[78]	-	*	-	-	-	30	*	>250	Fe NWs
						50			
						70			
[1]	600	-	-	-	10	40	4	60	NiAu NWs
	130							13	
	150				10	20		15	
	100							10	
[2]	-	500	-	-	-	35	0.5	14	Fe NWs
		1000					1	28.5	
		1800					1.8	51	
		2300					2.3	66	
		1000			-	50	1	20	
		700			-	110	0.7	6	
		*			*	32	1	31	FeAu NWs
		*			*	28	2.66	95	

Table 1.4:Thicknesses and materials of magnetic nanowires, adapted from literature. (*) not specified.

1.3.2.2 Physical characterization

It has been stated that, for infinite cylinders, the magnetization reversal mainly occurs in three different ways such as coherent rotation, magnetization buckling and magnetization curling. The reversal mechanism chosen by the nanowire depends on the relation between its radius and the critical one [12].

However, Wernsdorfer et al. [79] have shown that the reversal process results from the nucleation and propagation of a single volume along the wire, in 40 to 100 nm individual Ni wires; Based on this study, it has been stated, from Ferré et al. [70], that the magnetization reversal can be described in terms of nucleation-propagation mechanism.

Strijkers et al. [69] have further investigated the orientation of the Co nanowires c-axis, with diameters of 20 nm and 100 nm, by using NMR. The authors have stated that the magnetization behaviour is mainly a result of a competition between the demagnetization of the individual wires and dipole-dipole interaction with the neighbour wires. To conclude their work, the length of the Co wires has been decreased from 40 to 0.5 µm; it has been observed that a crossover takes place from a perpendicular easy direction of magnetization towards an easy direction parallel to the wire, and, as can be seen in figure 1.24, it occurs for wire's length of ~1µm. In addition, Metzger et al. [64] have also found that the Co nanowires have a distribution of c-axis orientation, confirmed by their study on 770 nm and 64 nm long NWs.

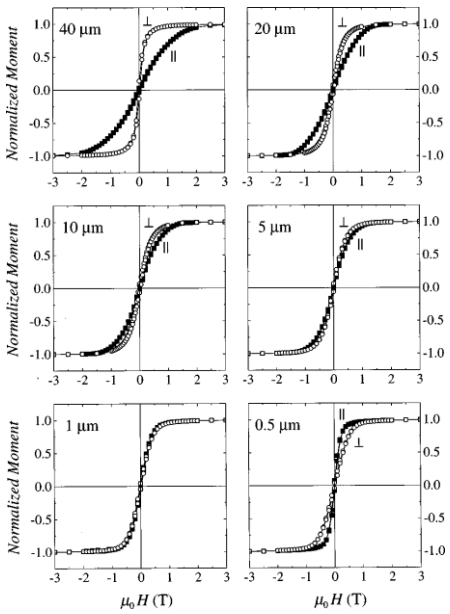

Figure 1.24: Magnetization hysteresis curves of 100 nm wires as a function of the wire length at 10 K, with the applied field perpendicular (open circles) and parallel (solid squares) to the wire axes [69].

Pal et al. [77] have also studied the magnetization reversal dynamics of Co nanowires with competing magnetic anisotropies and concluded that for length to diameter (L/D) higher than10 the shape anisotropy is the dominant contribution, which lead the easy axis to be parallel to the axis' wire, while for L/D lower than 3 the easy axis is perpendicular to the axis of the wire.

Ni nanowires have been widely studied, over a range of different diameters and lengths. Pignard et. al [71] has studied the magnetization reversal mechanism by anisotropic magnetoresistive (AMR) measurements of 22 μm-long Ni NWs with diameter of 35 and 75 nm and concluded that the first discrete jump represents the starting point of the reversal process, that ends after the second one.

Nielsch et al [72] have stated, by the study of (30,40,55)nm Ni NWs ,that the magnetic anisotropy of the array results from the interplay of the different effective fields. Carignan et al [73] have also studied the influence of the diameter of Ni nanowires on their magnetic properties and stated that the magnetic behaviour depends on the magnetization reversal process, which is different depending on the diameter length.

A considerable effort has been put on the study of segmented nanowires, due their suitable application in biomedicine. Carignan et al. [74] have investigated the magnetic behaviour of Ni/Cu nanowires and have concluded that the hysteresis curves of multilayer wires are closer than for pure ones, which indicates a reduction of the effective field. Moreover, it has been shown that a crossover between an easy axis to an easy plane occurs when the Ni/Cu ratio is reduced, giving the possibility to adjust the magnetic anisotropies by accurately tuning these lengths. Susano et al. [76] have also study Ni/Cu multisegmented NW arrays, with diameter of 50nm and made of alternating segments respective of Ni and Cu, with Ni length varied from 10 nm up to 140 nm. It has been found that coercivity and remanence increase with increasing Ni length, when the magnetic field is applied along the parallel direction.

Moraes et. al [75] have study the role of Cu length on the magnetic behaviour of Fe/Cu nanowires; in this work, the Fe length has been fixed at 30nm, while the Cu segments have been varied from 15 to 120 nm. For small Cu thicknesses the system has shown to behave like a nanowire array, while a decoupling of Fe discs has been observed for Cu spacer lengths greater than 60 nm.

Some authors have carried out different studies, using the Au material as spacer between ferromagnetic materials either Fe, as reported in [2] or Ni, as studied by Bañobre-López et al. [1]. This technique has revealed to be suitable for biomedical applications, such as MRI contrast enhancing agents.

Chapter 2

Experimental details

In this chapter, the fabrication techniques of the samples and characterization methods are briefly described.

2.1 Fabrication techniques

Two different routes have been used to fabricate the samples, either top-down and bottom-up. In the top down approach, the substrate patterning has been performed by interference laser lithography, with subsequent deposition either through magnetron sputtering and ion beam deposition. In the bottom-up approach, nanoporous alumina templates have been fabricated, followed by electrodeposition.

2.1.1 Top-down approach

A top-down route essentially refers to slicing or successive cutting of bulk material to get nano-sized particles.

Starting with a silicon substrate, the anti-reflective coating (ARC) WIDE-8B has been spin coated at 5000 rpm for 60 seconds and baked on a hotplate at 100°C for 40 seconds, followed by subsequent baking at 180°C for 60 seconds. After that, the negative resist tone (TSMR-IN027) has been spin coated on the ARC at 400 rpm for 60 seconds, followed by a baking step at 90°C for 90 seconds, which has led to a 280 nm resist stack in total. The sample has been patterned through laser interference lithography technique immediately after the spin coating steps, to prevent resist ageing.

2.1.1.1 Laser Interference Lithography

Interference lithography is a maskless patterning technique in which the standing wave pattern that exists at the intersection of two or more coherent beams is used to expose a photosensitive layer. The beams, with the same polarization, are made to interfere and

project the interference pattern on the resist. In this case, the beams are symmetrically incident at angles of $\pm\theta$ and the period of the interference pattern is $\lambda/2nsin(\theta)$. The experimental set-up in presented in figure 2.1a, where the beams cross each other at θ ~ 45°. After the exposure, the photosensitive material is developed, revealing the desired periodic pattern.

To yield a square array of dots, which characterize our samples, the system has specifically used a Lloyd's mirror interferometer, with a He-Cd laser (λ=325 nm) as light source. The first exposure has lasted 7 minutes; Subsequently, another exposure with equal time has been performed, rotated by an angle of 90°, in order to achieve the desired pattern, as can be seen in figure 2.1 b. The periodicity of the array and the lateral size of the pattern can be easily adjusted either by selecting the exposure dose, changing the incident angle or rotating the sample holder. The exposed resist has been post-baked at 110°C for 90s and developed in AZ736MIF for 1 min. Finally, the samples have been cleaned with deionized water and dried with nitrogen.

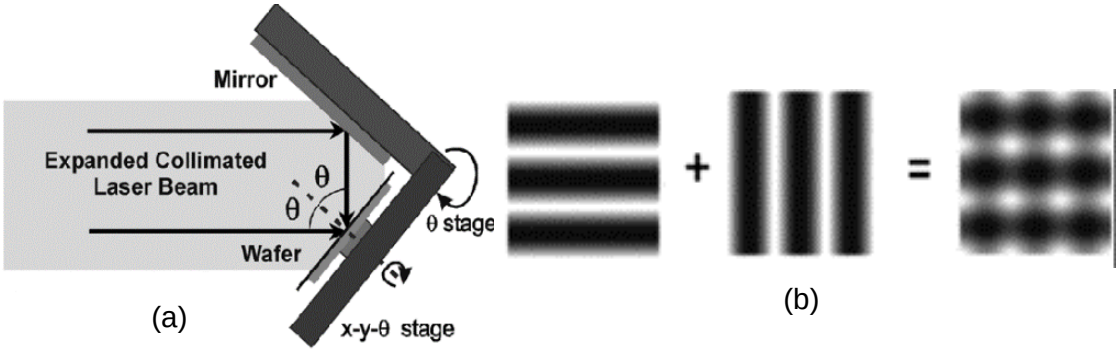

Figure 2.1:Interference lithography schematics. (a) Experimental set-up adapted from [89], (b) cross exposure with resultant pattern.

2.1.1.2 Ion Beam Deposition

In Ion beam deposition (IBD), which is a physical vapour deposition (PVD) method, the ions used to sputter the target are produced, accelerated and converged into a beam in an independent ion source (gun). The plasma is distanced from the targets allowing deposition pressures one order of magnitude lower than sputtering. The metallic or insulator target is grounded and the material sputtered from the target is deposited in a substrate.

The IBD used, Nordiko 3000 from INESC-MN in Lisbon, is a one module system incorporating a load lock separated by the main chamber through a guillotine gate valve.

Between the load lock and the gate valve there is a region dedicated to handling the samples, named dealer, which shares the same vacuum environment of the load lock.

A schematic diagram of the main chamber interior viewed from the back is presented in figure 2.2.

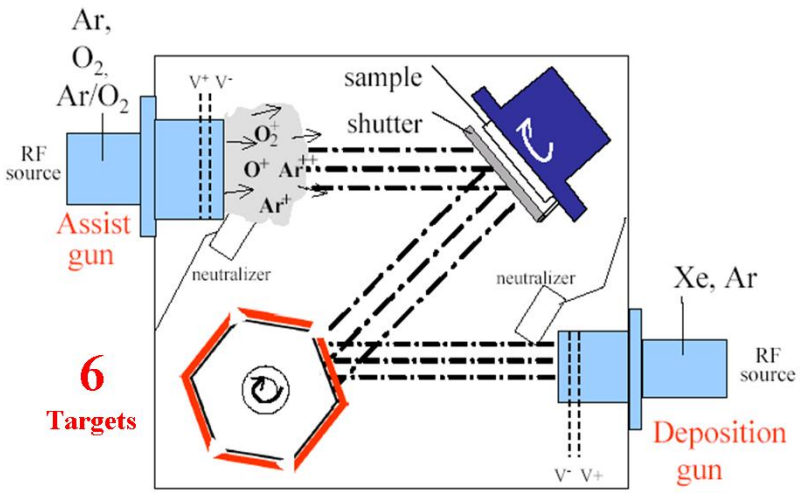

Figure 2.2: Ion beam system schematic representation, Norkiko 3000 at INESC-MN.

The system works with a base pressure down to 10^{-8} Torr and incorporates two ion beam guns, a substrate holder and a target holder in Z configuration. Both targets and substrate holders are water-cooled. The system works essentially with two inert gases, Ar for milling and Xe for deposition.

Six targets are used to deposit multilayer devices. The targets are mounted in a target holder which can rotate to align each target with the deposition gun. A shutter covers the targets not used, minimizing contamination. The substrate is automatically placed in the substrate holder with rotation capability up to 30 rpm, improving the uniformity, and equipped with fixed permanent magnets to create 4 mT (40 Oe) defining the anisotropy direction of the deposited materials. In addition, the substrate holder can rotate between pan = 0º to 80º, regarding the beam direction. The sample is loaded at 0º and is completely facing the assist gun at 90º, as represented in Figure 2.2. A shutter is also present to protect the processing sample from the plasma preparation.

The system has been used to produce multi-layers of thin films, in order to find the antiferromagnetic coupling, strictly depending on the thickness of the nonmagnetic layer. Several stacks of different thicknesses and materials have been fabricated, as reported in detail in chapter 3. The deposited materials have been Ti, Au, Fe and Ru, with deposition rates of 0.14 Å/s, 0.44 Å/s and 0.23 Å/s, respectively.

2.1.1.3 Magnetron Sputtering

The sputtering technique consists in the removal of atoms from a target composed of a certain material using an ionic beam by momentum transfer. The basic configuration of a sputtering system is based on two electrodes with diameter up to 200 mm, with separation of 50-60 mm, in a vacuum chamber with a gas line typically argon; power-supply is used connected to the target electrode (cathode) and to the substrate holder (anode). The potential difference feeds an electric discharge which creates and accelerated ions towards the target. The power supply can be either DC or RF, the first one is used in deposition of thin metallic films, while the RF in the deposition of insulation materials.

To increase the density of current keeping low gas pressures and low voltage a magnetron is used. The target electrode is modified including permanent magnets to create a magnetic field parallel to the target surface; the magnetic field in the cathode assures the shield of the electrical field from the discharge over 1 mm. In this region electrons released during the incidence of ions are confined. The energetic ions are not affected by this confinement and therefore the sputtering of the material and the emission of electrons continues. If the electrons released are free to move in the chamber due to the negative charge repulsion between the electrons and the target (cathode), the electrons collide with the gas molecules resulting in the ionization of the neutral Argon molecules keeping the plasma. In this situation if the gas pressure is reduced the ionization is also reduced to the limit of the plasma extinction.

Therefore, the advantage of magnetrons is the reduction of the limit pressure for the plasma due to the confinement of the electrons from the target.

The magnetron sputtering that have been used to deposit the desired films are Nordiko7000 and Nordiko2000, from INESC-MN in Lisbon.

The Nordiko7000 is an automated 6-inch capable modular sputter system consisting of a central dealer module connected to a load lock module and four other process modules. Each process module and the dealer are pumped with cryogenic pumps which provide base pressures of $\sim 5 \times 10^{-9}$ Torr, while the load lock is pumped with a turbo pump capable of reaching $\sim 5 \times 10^{-6}$ Torr. All the modules are separated from the dealer by gate valves which allows more than one wafer to be processed at a time.

The four process modules serve different purposes: flash annealing, sputter etching, TiW(N) deposition and AlSiCu deposition. In this specific case, only the last module has been used; a thin sacrificial layer (~30nm) of AlSiCu with a DC power supply and

deposition rate of 2000 W and 37.5 Å/s, respectively, has been deposited at the bottom of the synthetic antiferromagnetic structures.

Nordiko2000 is a DC/RF Magnetron Sputtering system which has six main targets with 3-inch diameter mounted on magnetrons at the top part of the chamber, and an extra 2-inch target at a magnetron adapted to the load lock, as shown in Figure 2.3a.

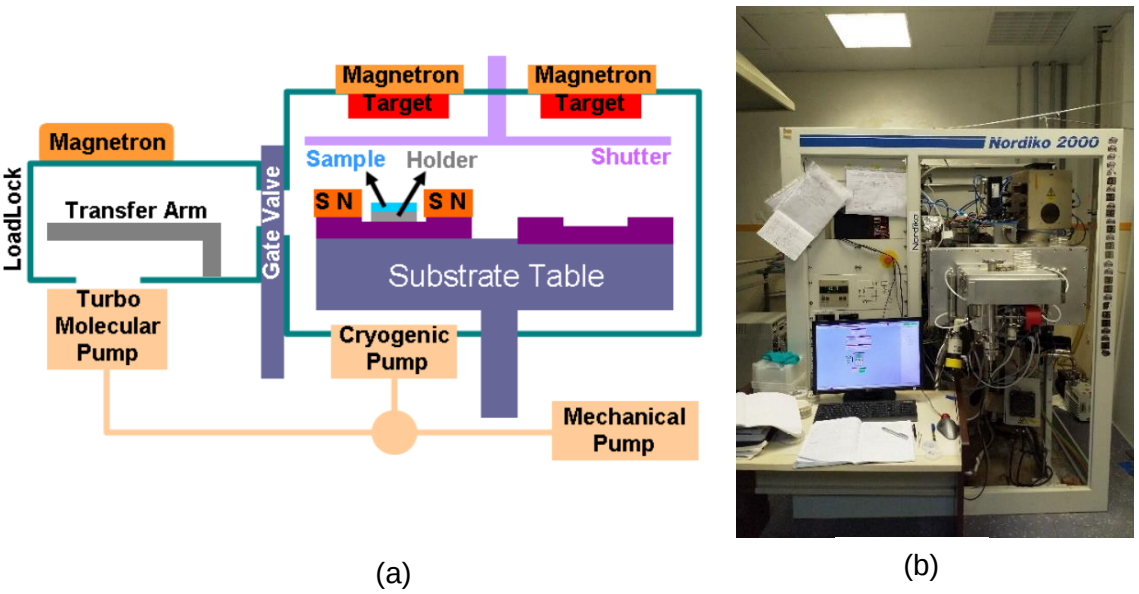

(a) (b)

Figure 2.3: Nordiko2000 DC/RF Magnetron Sputtering system; (a) schematic representation, (b) picture.

The access to the main chamber is made through a load lock and an automatic arm. The chamber has a substrate table with 12 slots, however only one has permanent magnets mounted to define the anisotropy direction during deposition with 25 Oe field uniform over a sample area of 2x2 inch2. The relative position between the fixed targets and the wafer is set by rotating the table and a shutter is present with rotation capability. The load lock is pumped by a turbo pump down to $\sim 5 \times 10^{-6}$ Torr and the chamber can achieve base pressure of $\sim 5 \times 10^{-8}$ Torr pumped by a cryo-pump. Nordiko2000 has been used to deposit stacks composed of different materials, such as Ta, Ru, CoFeB and CoFe with deposition rates of 0.54 Å/s, 0.543 Å/s, 0.303 Å/s and 0.53 Å/s, respectively.

2.1.2 Bottom-up approach

The other fabrication method used has been the template-assisted electrodeposition in PAA templates, which consist on a bottom-up route which starts with building blocks such as atoms, molecules and whose assembly is controllable.

2.1.2.1 Porous anodic alumina templates

Anodization is an electrochemical oxidation process employed to increase the thickness of the native oxide layer on the surface of metals or semiconductors. Among anodizable materials, aluminium has been of particular interest due to its many profitable engineering properties.

Anodization of aluminium can results in two different types of anodic oxide, depending on the nature of the used electrolyte; a compact and non-porous barrier-type from neutral electrolytes and a porous-type oxide from acid ones [80]. Focusing on the PAA, it's divided into two parts, a thin oxide barrier layer which is in conformal contact with the Al and a relatively thick porous oxide film composed of nanopores extending from the oxide barrier to the surface of the film. The growth of the PAA films relies on a balance between electrical-field-driven oxide formation at the metal/oxide interface and oxide dissolution at the electrolyte/oxide interface. The electrochemical process can be expressed as follows:

$$2Al(s) + 3H_2O(l) \rightarrow Al_2O_3(s) + 6H^+(aq) + 6e^- \quad (2.1)$$

and

$$Al_2O_3 + 6H^+(aq) \rightarrow 2Al^{3+}(aq) + 3H_2O(l) \quad (2.2)$$

which correspond to the formation (Eq. 2.1) and dissolution (Eq. 2.2) of the oxide at the anode [65].

These nanopores, in specific electrochemical conditions, self-organize into a close-packed hexagonal arrangement (Figure 2.4); their diameter and interpore distance depend on the type of electrolyte an applied voltage during the anodization process. [81].

The pre-treatment of the substrate is of great importance, since the surface morphology and purity influence the organization of the template. The processes involved in the fabrication of the template are briefly described in the following paragraphs.

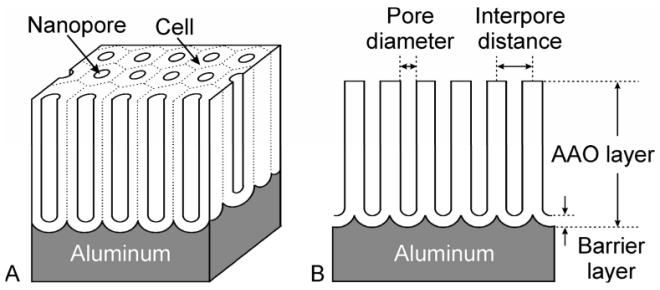

Figure 2.4: Schematic representation of hexagonally arranged nanopores in anodic porous alumina (A) and cross-sectional view of anodized layer (B). Adapted from [90].

Substrate cleaning**:** An Al foil (99.997% purity) has been cut in squares of 1.5 cm2 and subsequently pressed to level the surface. The samples have been rinsed in ultrasound baths of acetone and ethanol for 3 minutes, without passing them through water since the electropolish solution is hydrophobic.

Electropolishing**:** Electropolishing is the electrolytic removal of a metal in an ionic solution by means of an electrical potential and is used to remove a thin layer of undesired materials on the surface of the metal. This process also improves the Al surface prior to the anodization, by smoothing the peaks and valleys [82]. The used set-up is shown in figure 2.5a. It consists in a metal substrate (anode) and platinum mesh (cathode), which are in an electrolyte solution that establishes an electric circuit with a DC voltage applied. The temperature of the electrolyte has been to be controlled (bellow 10°) and the DC voltage (20V) has been applied for two minutes. After this process the substrates have been rinsed with ethanol, followed by deionized water and thus ready to be anodized.

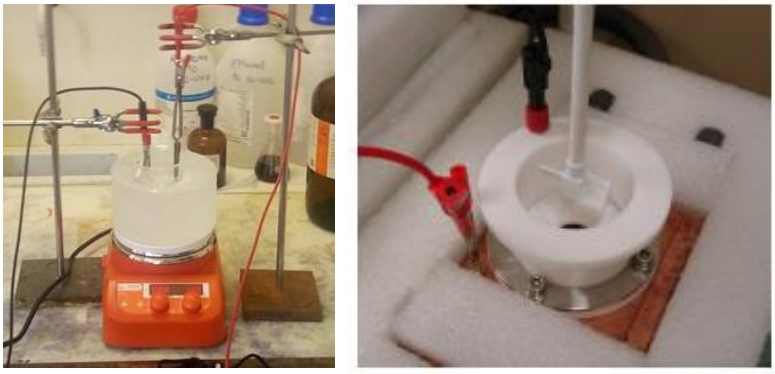

(a) (b)

Figure 2.5: Experimental set-up for (a) Electropolish and (b) Anodization.

Anodization: The electrochemical cell used consists of a Teflon container with the Al substrate (working electrode) placed in a small hole, on the bottom, and a Pt mesh is inserted at the top (counter electrode), Figure 2.5b. An O-ring is used to prevent any leakage between the sample and the container. The anodization has been performed under constant potential and the current monitored as a function of time using a digital source meter (Keithley 2400 C) controlled by a home-developed LabVIEW program. The source meter has been connected to the Pt mesh and to a Cu plate in direct contact with the Al sample. The anodization of the samples has been performed in two steps, always with the oxalic acid ($C_2O_4H_2$) as the electrolyte, with concentration of 0.3 mol/L.

The first anodization step consists in the application of 40 V for 24 h (mild anodization conditions) while keeping the temperature around 3°C and subsequent chemical etching of the grown aluminium oxide layer. After dissolution of the oxide layer, a periodic concave-triangular features formed on the aluminium surface serve as nucleation sites for the formation of nanopores during the second anodization (second step).

The second anodization has been conducted at the same anodizing potential as been used during the first anodizing step. A potential of 40 V has been firstly applied for 5 minutes. This creates a thin PAA template to suppress breakdown effects caused by the high current densities, used in the second step. An increased rate of 0.6 V/s follows, to get the hard anodization step at to 140 V (hard anodization). This voltage has been applied for two/three hours, being followed up by another minute with 40 V, to stabilize the barrier layer at the bottom of the pores [83] .

Aluminium removal and Pore widening: After the anodization process, the Al is removed from the samples using 0.2 M $CuCl_2$ in a 4.1 M HCl aqueous solution, at room temperature. The opening of the pore and consequently widening has been done using a solution of 0.5 M H_3PO_4 ; the basics of this procedure consist in put the templates, with the bottom side in contact with the acid, laid carefully on the surface of the solution. The membranes are made to float, with the top side never below the liquid level, until they start to create bubbles on the top of the surface to further sink into the solution, which means that the pores have been opened. The temperature of this process has needed to be optimized for hard anodization membranes. In fact, at room temperature, besides the amount of time needed to widen the pores (~12h), it has been observed that the acid solution started to corrode the sides of the floating membranes, leading to very thin templates that have not been possible to use. Several trials with different temperatures have been performed in order to obtain solid, high resolution and good reproducibility membranes. The optimum conditions have been observed with the process performed in a stirred-thermic bath (to ensure temperature uniformity) at 55 °C and 500 rpm. Under these conditions, the sinking of the membranes have been observed after a time of ~23 min. A thin Au layer has been then sputtered on the backside of the membrane to serve as the working electrode.

2.1.2.2 Electrodeposition

Electrodeposition is a chemical deposition method with a high growth rate in which an electrolyte solution is used to deposit material in a conductive substrate. The set-up used for electrodeposition is similar to the anodization, with the PAA template as the cathode and Pt mesh as the anode. A LabVIEW routine has been used to control the process. The deposited materials are Au and Fe. To deposit the Au layers, Orosene has been used as solution; in the case of Fe, the prepared solution consists in an aqueous mixture of 0.4 M of boric acid (H_3BO_3), 0.003 M of ascorbic acid ($C_6H_8O_6$) to prevent Fe oxidation, and 0.19 M of iron sulphate heptahydrate ($FeSO_4 \cdot 7H_2O$). The deposition potentials are 1 V and -1.1 V and the deposition rates have been calculated to deposit the desired thicknesses, as discussed in Chapter 3.

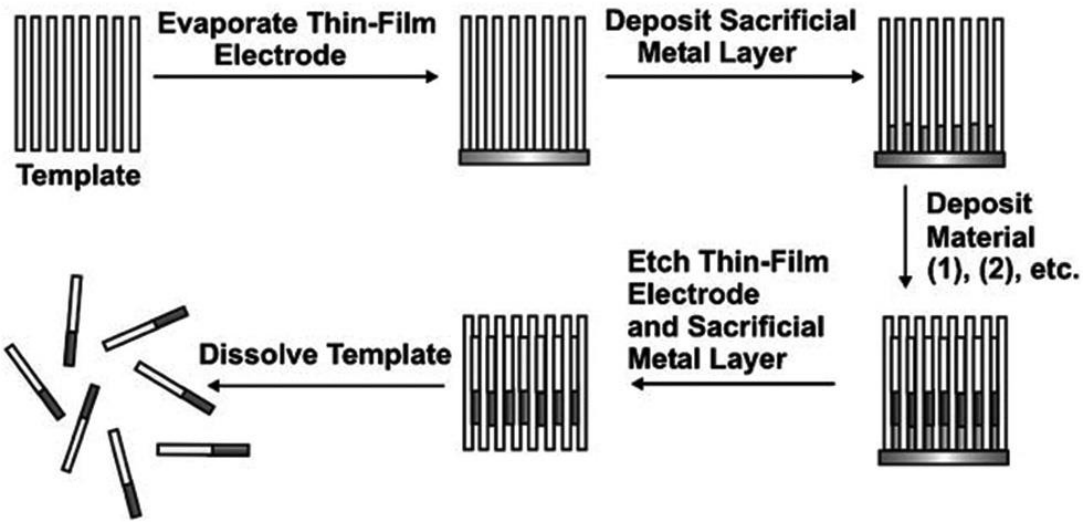

Figure 2.6: General scheme describing the fabrication of nanorods/nanowires by electrodeposition into nanoporous templates. From [80].

2.2 Characterization methods

The samples' structure and morphology have been characterized by X-rays diffraction and scanning electron microscopy, respectively. The magnetic properties have been investigated with superconducting quantum interference device and vibrating sample magnetometer.

2.2.1 Scanning Electron Microscopy

The scanning electron microscope (SEM) is one of the most versatile instruments available for the examination and analysis of the microstructure morphology and chemical composition characterizations. With the beam focused on the sample and with a set of magnetic lenses that control its motion, on the surface, an image of the detected electrons after the interaction with the sample surface can be created. Image formation in the SEM is dependent on the acquisition of signals produced from the electron beam and specimen interactions. These interactions can be divided into two major categories: elastic interactions and inelastic interactions. Elastic scattering results from the deflection of the incident electron by the specimen atomic nucleus or by outer shell electrons of similar energy. This kind of interaction is characterized by negligible energy loss during the collision and by a wide-angle directional change of the scattered electron. Incident electrons that are elastically scattered through an angle of more than 90˚ are called backscattered electrons (BSE), and yield a useful signal for imaging the sample. Inelastic scattering occurs through a variety of interactions between the incident electrons and the electrons and atoms of the sample, and results in the primary beam electron transferring substantial energy to that atom. The amount of energy loss depends on whether the specimen electrons are excited singly or collectively and on the binding energy of the electron to the atom. As a result, the excitation of the specimen electrons during the ionization of specimen atoms leads to the generation of secondary electrons (SE), which are conventionally defined as possessing energies of less than 50 eV and can be used to image or analyse the sample. In addition to those signals that are utilized to form an image, a number of other signals are produced when an electron beam strikes a sample, including the emission of characteristic x-rays, Auger electrons, and cathodoluminescence.

The most commonly used modes are secondary electrons, backscattered electrons and energy-dispersive X-ray spectroscopy (EDS).

When the primary beam strikes the sample surface causing the ionization of specimen atoms, loosely bound electrons may be emitted, and these are referred to as secondary electrons. As they have low energy, typically an average of around 3–5 eV, they can only escape from a region within a few nanometers of the material surface. So secondary electrons accurately mark the position of the beam and give topographic information with good resolution.

Another valuable method of producing an image in SEM is by the detection of BSEs, which provide both compositional and topographic information in the SEM. A BSE is

defined as one which has undergone a single or multiple scattering events and which escapes from the surface with an energy greater than 50 eV.

Another class of signals produced by the interaction of the primary electron beam with the specimen is characteristic X-rays. The analysis of characteristic X-rays to provide chemical information is the most widely used microanalytical technique in the SEM.

In order to characterize our sample, a FEI Quanta 400FEG high resolution (HR) SEM has been used.

2.2.2 X-Ray Diffraction

X-ray diffraction (XRD) analysis allows for the identification and structural characterization of the samples. The diffraction pattern arises from the interaction between the X-rays and the electrons in the atoms. Bragg diffraction happens when the wavelength of the incident electromagnetic radiation is comparable to the inter-atomic distances in the crystalline sample, acting as diffractive centres. The constructive interference between the reflected radiation results in Bragg peaks, each one corresponding to a set of Miller indices hkl. Bragg's law can be expressed as follows:

$$n\lambda = 2d_{hkl}\sin(\theta) \tag{2.3}$$

where n is an integer, *l* is the wavelength, $2d_{hkl}$ is the distance between planes with Miller indices hkl and θ is the angle of incidence of the X-ray in respect to the atomic plane. Our XRD measurements has been performed on a Rigaku SmartLab diffractometer, at IFIMUP-IN.

2.2.3 Superconducting Quantum Interference Device

Superconducting quantum interference device (SQUID) is a very sensitive magnetometer based on superconducting loops. This device features a superconducting magnet in a helium bath, that applies a magnetic field up to 5.5 T, and a magnet control system that allows for accurate magnetization measurements in the 5 - 380 K temperature range. There are two types of SQUID, the radio frequency RF SQUID and the direct current (DC) SQUID having one Josephson junction, and two or more, respectively. A Josephson junction is made by sandwiching a thin layer of a non-superconducting material between two layers of superconducting material, which allow quantum tunnelling effect to occur. This effect is influenced by magnetic fields in its vicinity, which enables the Josephson junction to be used in devices that measure

extremely weak magnetic fields. The SQUID used in this work is from Quantum Design at IFIMUP-IN.

2.2.4 Vibrating Sample Magnetometer

The characterization of the magnetization of a thin film have been made using a Vibrating Sample Magnetometer (VSM), DMS 880. The operation principle is schematized in Figure 2.7. In a VSM, the sample with moment M is mounted on a vibrating holder, a glass rod. A vibration at frequency f = 200 Hz is induced to the sample holder by a piezoelectric crystal which originates a magnetic flux change φ in time. A set of pick up coils placed around the sample produces a differential of potential induced by φ which is proportional to the total moment of the sample, $V \propto d\varphi/dt$. The magnetic characterization of the sample is made by varying an external dc field created by an electromagnet with field resolution of about 0.1 Oe (8 A/m). The moment resolution of the VSM tool is about 10^{-5}emu ($10^{-2} A \cdot m^2$). The sample holder used, and in almost cases the sample substrate, is composed of glass with a diamagnetic demagnetizing contribution that is then is subtracted to the measurement.

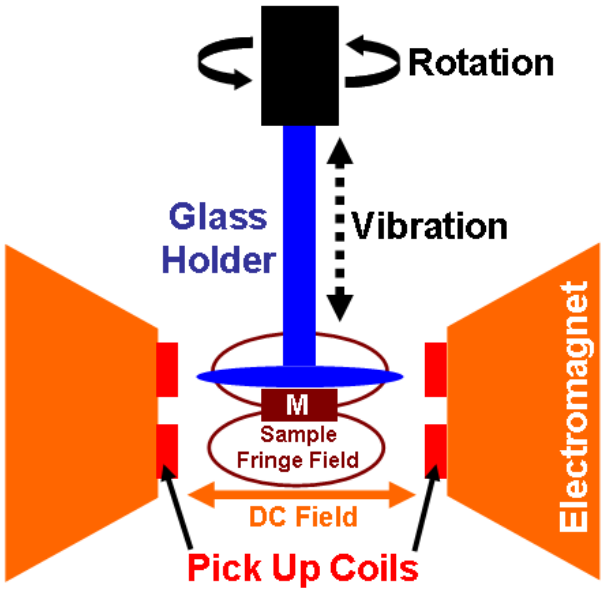

Figure 2.7: VSM operation principle schematics.

2.2.5 Magneto Optic Kerr Effect

Magneto-optic Kerr effect (MOKE) describes the change of the polarization states of light when reflected at a magnetic material. Three different configurations can be used; in the polar configuration, the magnetization lies perpendicularly to the sample surface; in the longitudinal Kerr effect the magnetization lies parallel to the sample surface and to the plane of incidence. The transversal configuration is characterized by the magnetization parallel to the sample surface while perpendicular to the plane of incidence.

Chapter 3

Magnetic nanostructures

The fabrication process of Synthetic Antiferromagnetic (SAFs) nanoparticles can be divided into two different approaches: ‘bottom-up’ and ‘top-down’. In the ‘bottom-up’ approach all begins from small building blocks such as atoms and molecules that get assembled to form nanostructures; examples of this approach are the anodization and electrodeposition techniques used in this work. By contrast, the ‘top-down’ starts from a bulk material, which is the step-by-step removed to form objects in the nanometer scale, in this work the lithography and sputtering/ion beam deposition. In this Chapter the structural, morphological and magnetic characterization of the SAF nanoparticles/nanowires is presented.

3.1 Synthetic antiferromagnetic nanoparticles grown through the top-down route

Starting from a silicon substrate with approximate thickness of 360 μm, the ARC WIDE-8B has been spin coated at 5000 rpm for 60 seconds followed by two-steps process on a hotplate: 40 seconds at 100°C with subsequent 60 seconds at 180°C. The negative resist tone (TSMR-IN027) has then been spin coated on the ARC at 400 rpm for 60 seconds, followed by a baking step at 90°C for 90 seconds, which has led to a 280 nm resist stack in total.

Immediately after the spin coating steps, to prevent resist aging, the samples have been patterned through IL technique.

To yield a square array of dots, the system has specifically used a Lloyd’s mirror interferometer, with a He-Cd laser as light source. Two exposures have been performed and both lasted 7 minutes, with the beam rotated by an angle of 90 to achieve the desired pattern, as shown in section 2.1.1.1. After being patterned, the exposed resist has been post-baked at 110°C for 90 seconds and developed in AZ736MIF for 1 minute. Finally, the samples have been cleaned with deionized water and dried with nitrogen, to further be deposited.

3.1.1 Morphological and Structural Characterization

To access the morphological and structural characterization of our samples, the SEM and XRD technique have been used.

3.1.1.1 Scanning Electron Microscope (SEM)

To fabricate SAF nanodiscs, first polymeric templates have been patterned by interference lithography, a cost-effective technique that enables to pattern large areas (in this work homogeneous samples with 2 cm^2 have been prepared), leading to high mass production of magnetic nanostructures for biomedical assays. The set-up of the equipment makes easy to tailor the shape and size of the nanoelements, from about 50 nm up to a few microns, which enables to engineer nanostructures with specific magnetic properties. Through use of a negative route, as described in section 2.1.1.1, we have been able to fabricate arrays of resist antidots (holes), namely SAF_Dots0, as presented in Figure 3.1, so that the magnetic discs have grown on the substrate and remained attached to it after the lift-off process. Therefore, to be able to detach the magnetic nanostructures from the wafer, a sacrificial layer has been placed between the Si wafer and the resist coating.

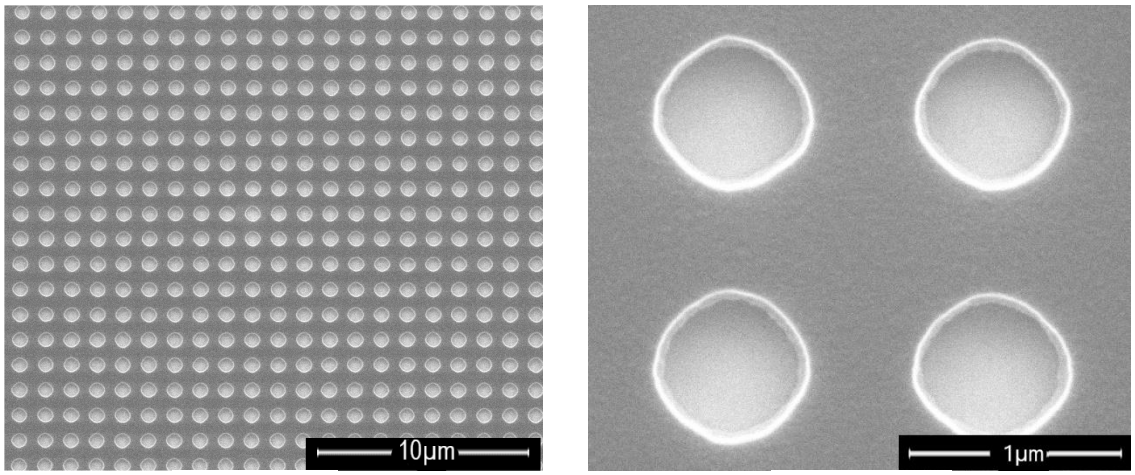

(a) (b)

Figure 3.1: SEM images of patterned discs previous deposition (SAF_Dots0). (a) Magnification of 10 000x, (b) Magnification of 100 000x

While a considerable number of materials have been deposited onto thin glass bars to find the antiferromagnetic peak, as shown in the magnetic characterization part,

section 3.1.2, the stack deposited through magnetron sputtering in the Si substrate patterned by interference lithography, named SAF_Dots1, is the following one: $Al_{98.5}Si_1Cu_{0.5}(300)/[Ta(50)/Ru(20)]_2/Co_{80}Fe_{20}(60)/Ru(8)/Co_{80}Fe_{20}/Ru(20)/Ta(50)$, with thicknesses expressed in Å.

The structures have been imaged through the SEM and reported in Figure 3.2.

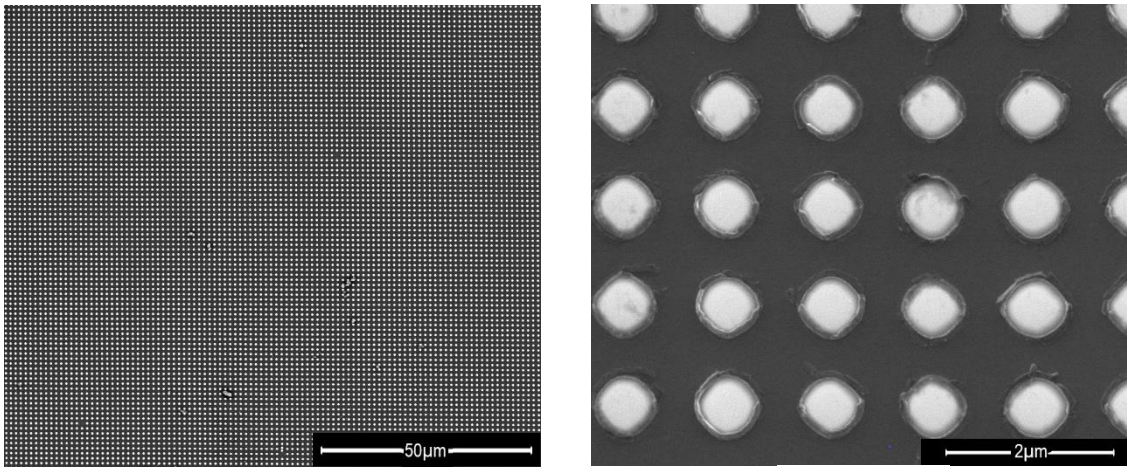

(a) (b)

Figure 3.2: SEM images of the magnetron sputtered discs after resist development (SAF_Dots1). (a) Magnification of 2 000x, (b) Magnification of 40 000x.

From Figure 3.1 and 3.2 it can be noticed that the shape of the discs is not an ideal circle, but more like a lozenge, as expected from the nature of the fabrication of the discs, namely the IL previously discussed. Furthermore, Figure 3.2 shows that the lift off has led to a complete removal of the photoresist, achieved by the use of an already optimized process; this process consists in the use of an organic developer (1-Methyl-2-pyrrolidone, NMP) heated in a glass up to 135 °C, where the sample has been then introduced and left in solution for 5 minutes; it has followed an ultrasonic bath for 30 seconds with subsequent cleaning with isopropanol and deionized water. Finally, the sample have been dried and its surface investigated through a microscope; the steps have been repeated until a surface without leftover resin has been achieved (5 cycles). In the upper image little pieces of photoresist are visible around the perimeter of the dots, and, for this reason, a further ultrasound bath has been performed in order to ensure a complete remove (not shown). Thus, areas of 2 x 2 cm^2 of homogeneous discs have been obtained as presented in Figure 3.1 a.

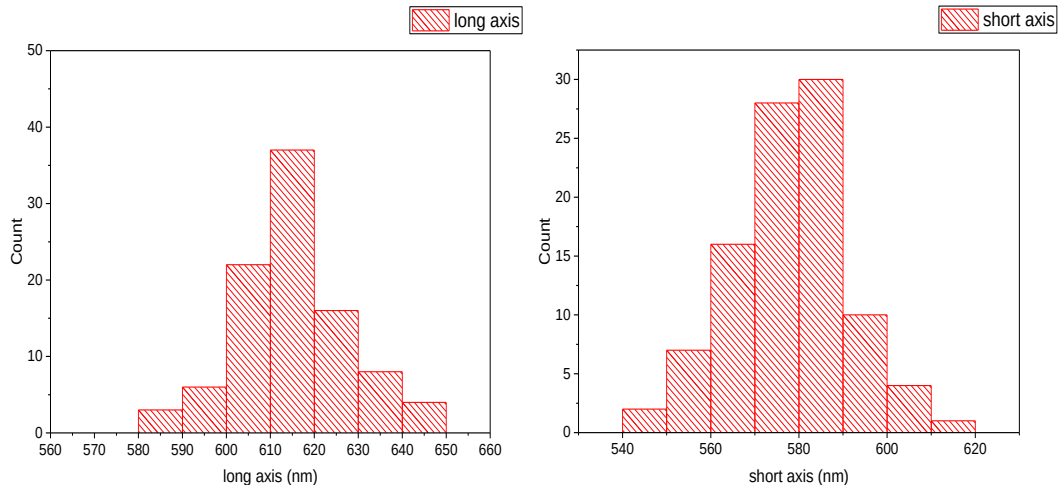

Figure 3.3: Analysis of discs diameter (SAF_Dots0). (a) Long axis' histogram, (b) Short axis' histogram.

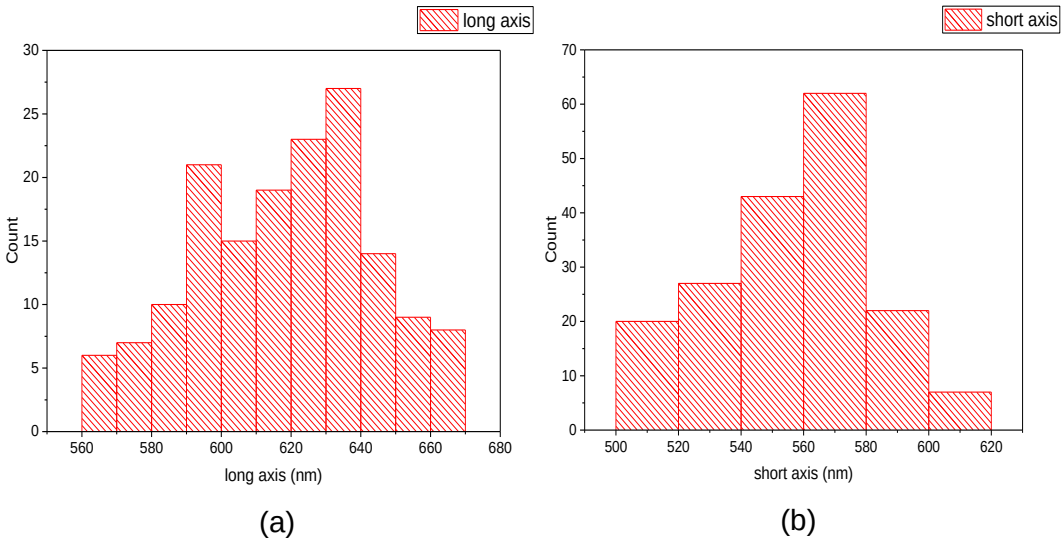

Figure 3.4: Analysis of discs diameter (SAF_Dots1). (a) Long axis' histogram, (b) Short axis' histogram.

The size distribution of the dots has been taken into account and the histograms relative to each main axis of the discs have been estimated with the help of the ImageJ software [84], as reported in figure 3.3 and 3.4, for sample SAF_Dots0 (previous deposition) and SAF_Dots1 (After deposition), respectively. The average sizes and standard deviations of the long and short axis for SAF_Dots0 are μ_{long}=615,3 nm and μ_{short} =578,2 nm with σ_{long}=12,4 nm and σ_{short}=12,8 nm, while μ_{long}=618,8 nm and μ_{short} =557,9 nm with σ_{long}=25,6 nm and σ_{short}=24,7 nm for SAF_Dots1. The average values of the long axis are almost equal in the two cases, while the short axis' value present a slight decrease after the depositions. The variances of the acquired data

increase after the lift-off process, as small pieces of the photoresist may have remained attached to the dots slightly modifying their diameters, as can be seen in Figure 3.2 b.

3.1.1.2 Energy-dispersive X-ray spectroscopy (EDS)

Energy-dispersive X-ray spectroscopy (EDS) is an analytical technique used for the elemental analysis or chemical characterization of a sample. Its characterization capabilities are due to the fundamental principle that each element has a unique atomic structure, allowing a unique set of peaks on its electromagnetic emission spectrum. The excitation of the incident beam influences the electron configuration which results in a release of energy in the form of an X-ray. As the energies of the X-rays are characteristic of the difference in energy between two shells and of the atomic structure of the emitting element, EDS allows the elemental composition of the specimen to be measured, as presented in Figure 3.5.

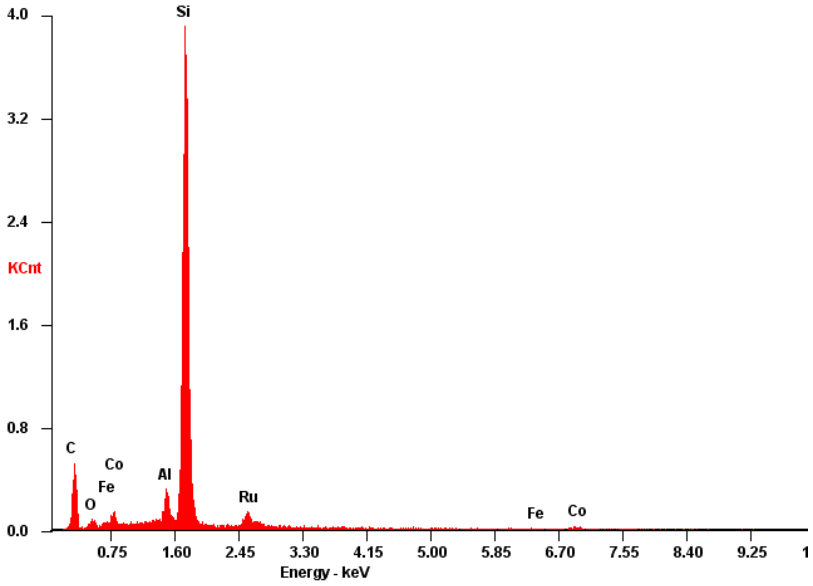

Figure 3.5: EDS spectrum of sample SAF_Dots1.

The reported figure shows that the major element is Si, being the substrate used as pattern for subsequent depositions. A considerable presence of Al is present, as deposited as first layer to further be able to release the discs. Ru, Co, Fe also appear, as are the main components of the structure; however, the intensities are not that high as the deposited layers are very thin. C and O has also been observed, due to the presence of photoresist residues and carbon tape used to fix the sample in the equipment.

3.1.2 Magnetic characterization

For magnetic characterization of the magnetron sputtered/ion beam deposited stacks, the VSM and MOKE techniques have been chosen. The hysteresis' loop vertical axes always refer to the normalized magnetic moment and not to the samples' total magnetization, as they have been cut by hand and therefore no accurate dimension could be calculated.

3.1.2.4 VSM measurements on magnetron sputtered samples

In order to find the antiferromagnetic coupling between the ferromagnetic layers, several stacks have been deposited on thin bar glasses, either by ion beam deposition or magnetron sputtering one, with subsequent magnetic characterization by using a vibrating sample magnetometer.

Two measurement have been performed for each sample, with the direction of the applied magnetic field parallel to the sample's plane; however, as the characteristic flat zone of the SAF manifests when the field is parallel to the direction of the magnetic moment of the sample defined by the deposition, to find the antiferromagnetic coupling only the parallel directions have been reported.

A typical hysteresis loop for such structures is of the form represented in Figure 3.6 a. This behaviour is due to the diamagnetic contribution of the glass substrate, whose thickness is much bigger that of the deposited sample. Because of this, the linear parts of the graph have been fitted and the magnetic contribution of the substrate has been subtracted from the real behaviour of the stacks, as shown in Figure 3.6 b. This process has been repeated for each hysteresis loop.

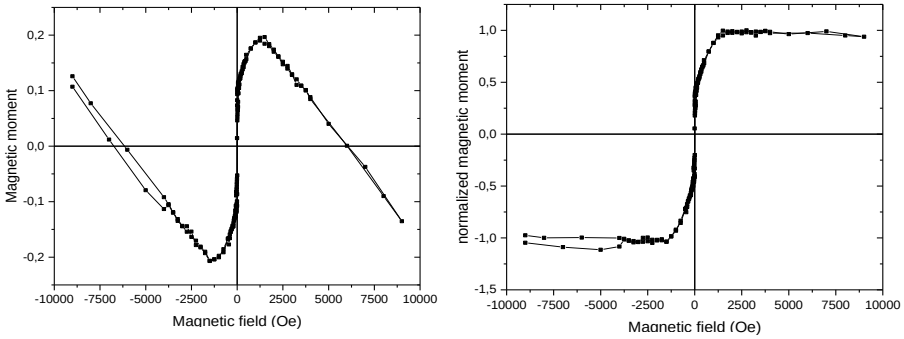

(a) (b)

Figure 3.6: Typical hysteresis loop characterized by diamagnetic contribution of glass thin film. Sample CoFeB_1, parallel direction. (a) Raw data, (b) processed data.

As widely reported in literature [47, 12, 6, 53, 49, 50], the first ensemble of deposited stacks (Batch 1 and Batch 2) have been fabricated through magnetron sputtering deposition with the following materials: CoFeB or CoFe as ferromagnetic layers, Ru as nonmagnetic spacer layer, and Ta to ensure chemical/magnetic stability and protect the stack. The details of the stacks are reported in Table 3.1 and Table 3.2 respectively, where thicknesses are expressed in Å, and the general structure of a synthetic antiferromagnet is presented in figure 3.7.

The two batches mainly differ on the choice of the ferromagnetic materials (CoFeB/CoFe) and in the protective one; while Batch 1 uses Ta, to further improve the nucleation of the ferromagnetic layer, in Batch 2 it has been decided to deposit a thin Ru layer over the Ta, as reported by Wei Hu et al. [49].

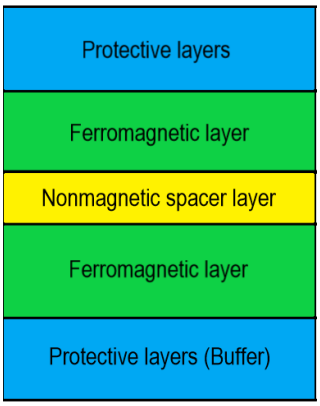

Figure 3.7: Schematic structure of the deposited stacks.

The fixed thicknesses of the layers have been chosen according to specific studies reported in literature, namely [6, 85] and [47, 49, 50] for Batch 1 and 2, respectively.

Batch 1	Ta	CoFeB	Ru	CoFeB	Ta	Hc(Oe)	μ_{rem}(%)
CoFeB_1	50	50	4	50	50	6.005	30.61
CoFeB_2	50	50	5	50	50	5.324	82.27
CoFeB_3	50	50	6	50	50	5.151	80.27
CoFeB_4	50	50	7	50	50	5.210	92.90
CoFeB_5	50	50	8	50	50	5.454	95.65
CoFeB_6	50	50	10	50	50	5.459	96.42

Table 3.1: Thicknesses, coercivity and remanence of deposited layers of Batch 1.

Figure 3.8 shows the hysteresis loops for the different sample of the batches (3.8 a), while in figure 3.8 b the remanence and coercivity values are presented as a function of the spacer thickness.

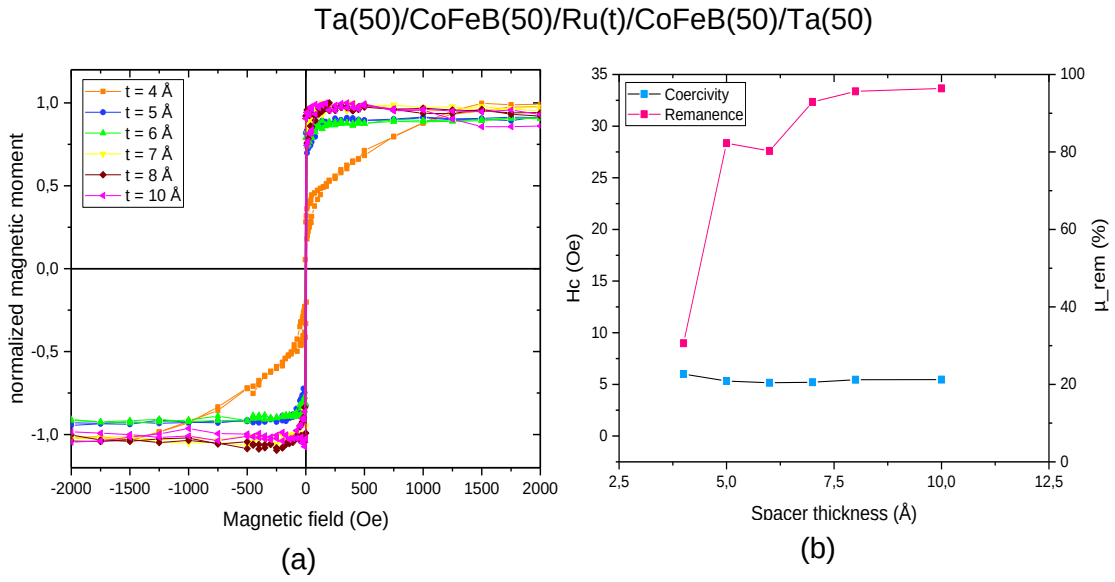

Figure 3.8: (a) In plane parallel hysteresis loops of Batch 1 samples. (b) Coercivity and remanence as function of spacer thickness.

While for t(Ru)>5 Å the curves present almost the same magnetic behaviours (quite low coercivity but high remanence field) and shapes, sample CoFeB_1 presents a significant decrease in remanence, which value is almost 1/3 when compared to the others of the same Batch, as can be seen from figure 3.8 b. It can be understood how the antiferromagnetic coupling strongly depends on the spacer layer thickness; specifically, changing its value from 4 to 5 Å, the remanence field triplicates.

Thus, sample CoFeB_1 can be considered a SAF good candidate due to its low remanence values, however, for further application in biomedicine, its remanence value is still too high; is important to remind that for such application the zero remanence field is a crucial property, in order to prevent particle from agglomeration when dispersed in solution.

To further try to decrease the remanence values, Batch 2 has been fabricated, where the CoFeB ferromagnetic layers have been substituted with CoFe and thin Ru layers (20 Å) have been added to the Ta to improve the nucleation of the magnetic layers and the protection of the deposited stack; its characteristics are reported in the table below (Table 3.2)

Batch 2	Ta	Ru	CoFe	Ru	CoFe	Ru	Ta	Hc(Oe)	μ_{rem}(%)
CoFe_1	50	20	60	4	60	20	50	*	*
CoFe_2	50	20	60	6	60	20	50	*	*
CoFe_3	50	20	60	8	60	20	50	88.38	5.51
CoFe_4	50	20	60	10	60	20	50	71.97	4.98
CoFe_5	50	20	60	12	60	20	50	9.24	63.69
CoFe_6	50	20	60	25	60	20	50	15.01	41.51

Table 3.2: Thicknesses, coercivity and remanence of deposited layers of Batch 2.

The coercivity and remanence values of samples CoFe_1 and CoFe_2 have not been found. Samples CoFe_5 and CoFe_6 show low coercivity values but higher remanences, which behaviour is typical of a soft ferromagnetic material [86], as previously reported. The choice is thus between sample CoFe_3 and CoFe_4; both present a weak antiferromagnetic coupling. Looking at the values reported in Table 3.2, the best apparent choice would be the sample which has lower remanence and coercivity, namely CoFe_4; however, considering the shape of the loops (Figure 3.9), the most appropriate sample is CoFe_3 where the thickness of the spacer is 8 Å, because of its lower magnetic susceptibility, essential for biomedical applications [50]. The SAF is still not perfect, as its remanence magnetization and coercivity are not zero, but its shape can be compared to those reported in literature, by A.L Koh et al. [47] for instance.

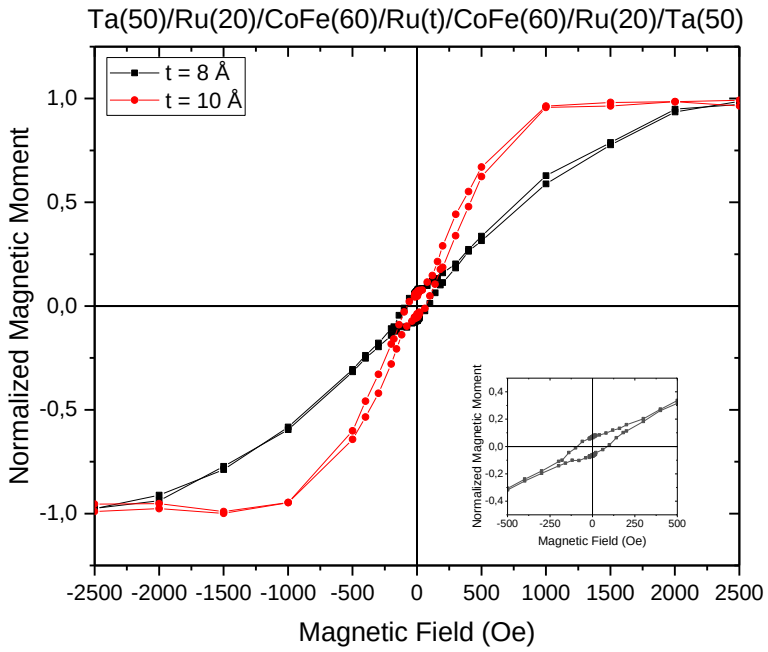

Figure 3.9: In plane parallel hysteresis loops of CoFe_3 and CoFe_4 samples. Zoom: detail around zero of CoFe_3.

3.1.2.2 VSM measurement on IBD samples

Because of the need to use biocompatible materials, Batch 3, 4, 5 and 6 have been fabricated through ion beam deposition with the following materials: Au, Ti, Fe and Ru. The details of the stacks are reported in the following tables (Table 3.3, 3.4, 3.5 and 3.6 respectively), with thicknesses expressed in Å, followed by magnetic characterization.

In this ensemble of samples, different combinations of buffer and spacer layers have been explored, while maintaining fixed the thicknesses of Fe ferromagnetic layers in order to achieve the antiferromagnetic coupling with such material; the buffer layer, which is crucial for the chemical stability of the stack and for optimum nucleation of the ferromagnetic layers, has been varied between Ti/Au, Ti and Ru, while the material of the nonmagnetic spacer has been varied between Ti and Au, exploring a wide range thicknesses for each Batch, in order to find the antiferromagnetic coupling of the two iron layers.

Batch3	Ti	Au	Fe	Ti	Fe	Au	Hc(Oe)	μ_{rem}(%)
Ti_1	10	50	100	6	100	50	3.013	96.92
Ti_2	10	50	100	8	100	50	3.310	92.68
Ti_3	10	50	100	10	100	50	4.760	91.19
Ti_4	10	50	100	12	100	50	7.336	92.84
Ti_5	10	50	100	14	100	50	7.111	94.35
Ti_6	10	50	100	16	100	50	6.759	93.97
Ti_7	10	50	100	18	100	50	4.021	88.5

Table 3.3: Thicknesses, coercivity and remanence of deposited layers of Batch 3.

Table 3.3 reports the thicknesses of the deposited stacks of Batch 1. The nonmagnetic layer spacer, which serves as coupler, is the Ti. The first layers (Ti/Au) have been used as buffer and to facilitate the Fe nucleation, and the last one to protect the stack, particularly to prevent Fe oxidation.

The hysteresis loops for such structures are reported in figure 3.10. The coercivity and remanence have been calculated as well, as a mean of the positive and negative value, which should be equal as no exchange bias are expected; the values are summarized in Table 3.1. It can be clearly seen that the in-plane loops, parallel to the magnetization axis of the deposited thin films, don't show the behaviour expected for a synthetic antiferromagnetic structure [47].The thin films magnetic properties are closer to those of a soft ferromagnetic material [86], characterized by low coercivity and high remanence, when the magnetic field is turned off; moreover, varying the thickness of the nonmagnetic layer (Ti), no significant change in quantity and quality of the reported curves is observed; while the Hc values are tolerable for a typical SAF [53], remanence

values higher than 88.5%, which is the lowest value for Batch 3, cannot be acceptable especially because such particles will retain a high value of magnetization in absence of an external magnetic field, agglomerating in clusters when dispersed in solution [54]. Thus, it can be concluded that Titanium is not an appropriate material to be used as antiferromagnetic coupler, which is coherent as no studies with such element in this field have been found.

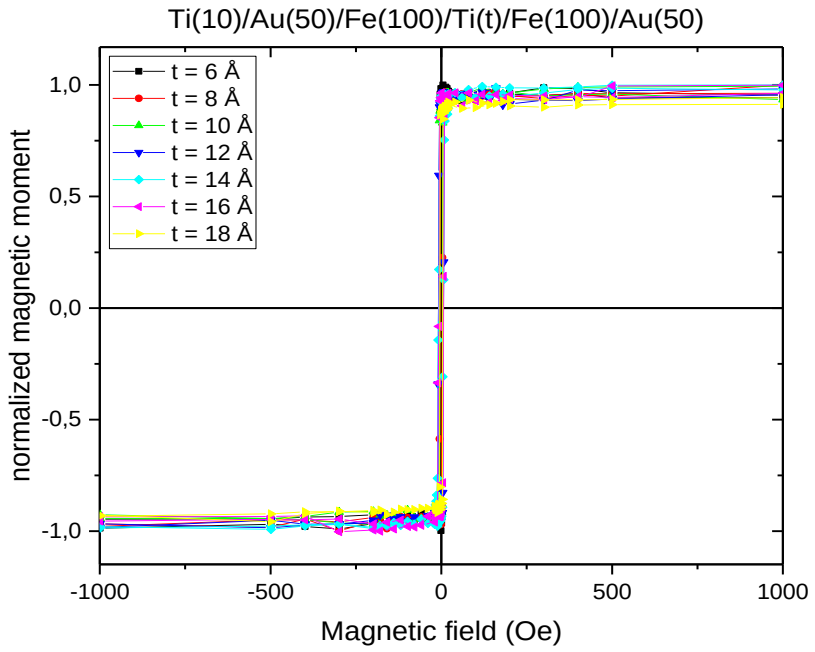

Figure 3.10: In plane parallel hysteresis loops of Batch 3 samples.

In Batch 4, a different approach has been adopted. The Ti spacer has been substituted by Au and the protective layers have been replaced by Ru to improve Fe nucleation; this because Au, previously used to nucleate the first Fe layer, is a material characterized by considerable roughness for the current proposal, affecting the grow of the subsequent deposited layers. The characteristics of Batch 4 are reported int table 3.4, with the associated values of coercivity, in Oe, and remanence, as a percentual of the normalized magnetic moment. The behaviour of the normalized magnetic moments as a function of the applied field and of the spacer layer is presented in Figure 3.11.

Batch 4	Ru	Fe	Au	Fe	Au	Hc(Oe)	μ_{rem}(%)
Au_1	50	100	8	100	50	3.024	92.90
Au_2	50	100	10	100	50	3.209	89.45
Au_3	50	100	12	100	50	4.119	90.19
Au_4	50	100	14	100	50	3.991	90.88
*	50	100	16	100	50	-	-
Au_5	50	100	18	100	50	4.072	96.23
Au_6	50	100	20	100	50	4.039	92.16
Au_7	50	100	22	100	50	4.056	87.62

Table 3.4: Thicknesses, coercivity and remanence of deposited layers of Batch 4. (*) Failed during deposition.

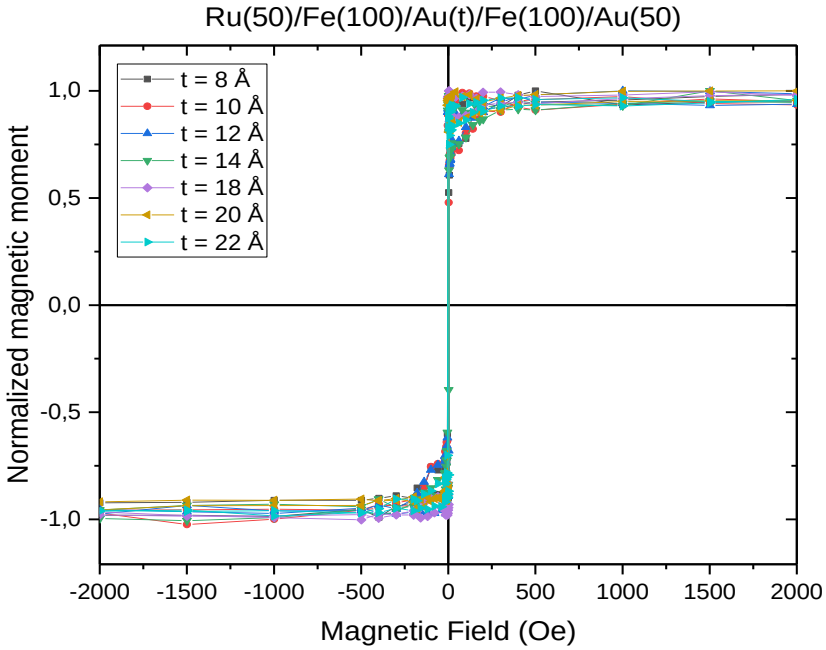

Figure 3.11:In plane parallel hysteresis loops of Batch 4 samples.

From the reported figure, no substantial differences are noticed in the behaviour of the curve by varying the thickness of the spacer, and the shape of the hysteresis loops matches the magnetic behaviour of a soft ferromagnetic material [86].

The first antiferromagnetic peak has been expected to be around 10 Å, as reported in Roosbroeck et. al's work [13]; however, for such spacer thickness no distinct behaviour has been observed. It has been thought, thus, that the material of the protective layers (Ru at the bottom and Au as cap layer) could have influenced the magnetic response, because it has been demonstrated that layers external to the basic ferromagnet/spacer/ferromagnet sandwich influence the interaction between the ferromagnetic layers [87]. For this reason, Batch 5 has been implemented, in which the first Ru and cap Au layers have been substituted both with Ti, in order to explore all the possible combinations, as can be seen in Table 3.5.

Batch5	Ti	Fe	Au	Fe	Ti	Hc(Oe)	μ_{rem}(%)
Au_8	50	100	8	100	50	15.025	88.79
Au_9	50	100	10	100	50	18.317	86.22
Au_10	50	100	12	100	50	17.988	88.81

Table 3.5: Thicknesses, coercivity and remanence of deposited layers of Batch 5.

Figure 3.12 reports the magnetic behaviour for such structures. The shapes of the curves matches the ones reported in Figure 3.12; the differences are, when comparing the samples Au_8, Au_9 and Au_10 with Au_1, Au_2 and Au_3 from the previous Batch ,respectively, a significant increase in the coercivity (4/5 times higher) and a slight decrease in samples' remanence, as represented in figure 3.13a and 3.13b, respectively.

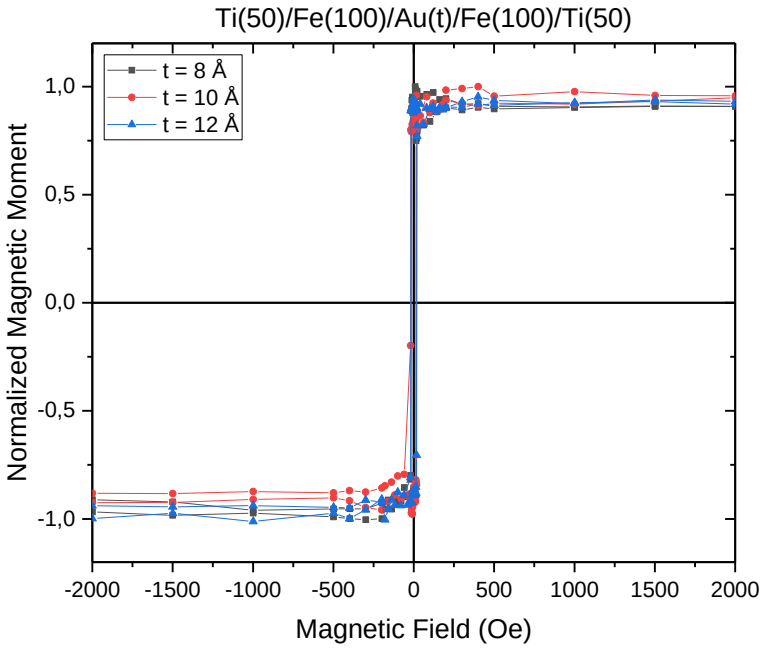

Figure 3.12: In plane parallel hysteresis loops of Batch 5 samples.

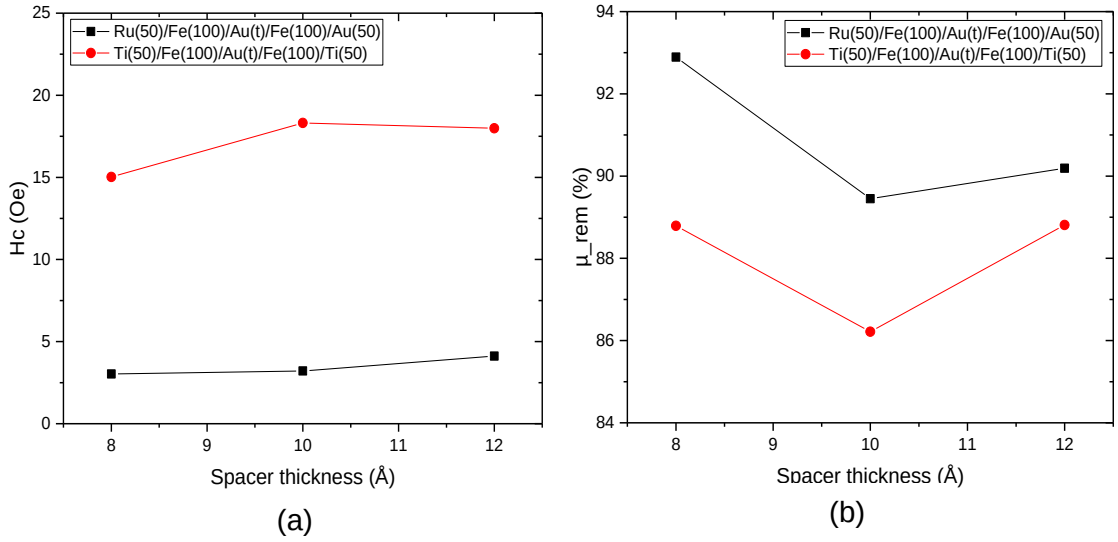

Figure 3.13: Comparison between (a) coercivity and (b) remanence values of samples Au_1, Au_2, Au_3 and Au_8, Au_9, Au_10.

To further investigate the Au properties as nonmagnetic spacer and its possibility to behave as a possible antiferromagnetic coupler, Batch 6 has been fabricated; the aim of this ensemble of samples has relied on the possibility to find a weak antiferromagnetic coupling, namely on the second peak of the oscillation, for thickness of the Au spacer around 25 Å; moreover, the protective layer of Ru has been changed with an opportune combination of Ti and Au. The thicknesses of the layers (in Å), the coercivity and remanence values are reported in Table 3.6.

Batch 6	Ti	Au	Fe	Au	Fe	Au	Hc(Oe)	μ_{rem}(%)
Au_11	10	50	100	20	100	50	4.078	92.97
Au_12	10	50	100	22	100	50	5.014	90.06
Au_13	10	50	100	24	100	50	3.738	89.28
Au_14	10	50	100	26	100	50	4.081	92.61
Au_15	10	50	100	28	100	50	4.407	90.47

Table 3.6:Thicknesses, coercivity and remanence of deposited layers of Batch 6.

The hysteresis loops are shown in Figure 3.14. Again, no flat region is observed around the zero applied field; the coercivity values are quite low as the previous one, while the remanence is still high.

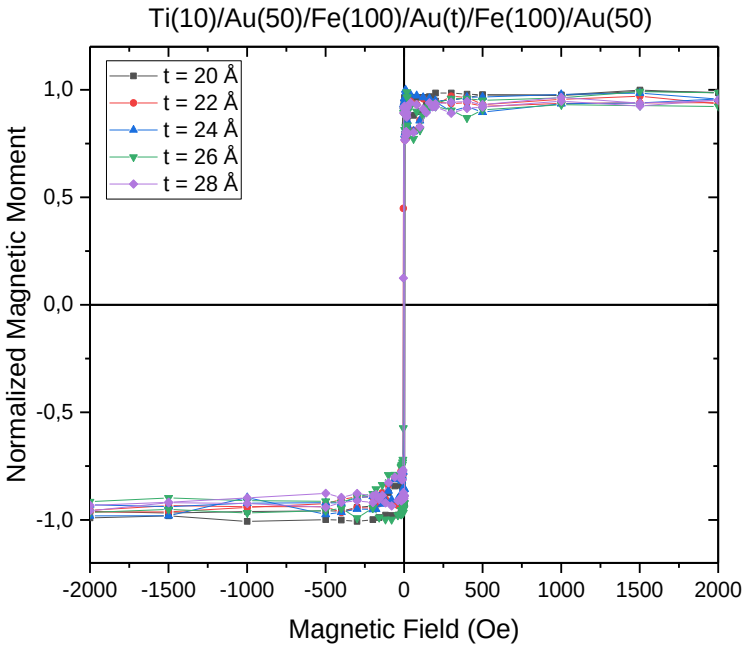

Figure 3.14: In plane parallel hysteresis loops of Batch 6 samples.

It is important to remind that the generic behaviour of oscillatory interlayer exchange coupling is an interaction which oscillates periodically in sign and magnitude, with an amplitude which decays as $1/t^2$, where t is the spacer thickness. The oscillation periods depend on the nature and crystalline orientation of the spacer metal, but not on the nature or thickness of the magnetic layers [87].

Interlayer exchange coupling in Fe/Au/Fe(100) sandwiches have been investigated by Unguris et al. [88]. The films have been epitaxially grown on single-crystal Fe(100) substrate; moreover, in this situation, the Au have been rotated by 45°C to match as much as possible the Fe(100) crystalline structure. In this situation, an antiferromagnetic coupling has been observed, fact that has not happened in our samples, where the films have not been grown onto single-crystal Fe(100) substrates and the Fe films have been deposited through ion beam deposition and not epitaxially grown. From this, it can be understood how difficult and how many factors may affect the antiferromagnetic coupling. In order to obtain a biocompatible synthetic antiferromagnet new samples need to be fabricated and an epitaxial growth of the layers must be adopted, in order to have precise control of the nucleation processes.

As no antiferromagnetic coupling has been found for the Fe ferromagnetic layers, either with Au or Ti spacers, it has been stated that the sample which better fulfil the requirements needed to a subsequent use in the biomedical field is CoFe_3.

3.1.2.3 VSM measurement on magnetron sputtered discs

For the reasons previously discussed, the stack that has been deposited on the patterned silicon substrates is the following one, with thicknesses expressed in Angstroms:

$Al_{98.5}Si_1Cu_{0.5}(300)/[Ta(50)/Ru(20)]_2/Co_{80}Fe_{20}(60)/Ru(8)/Co_{80}Fe_{20}/Ru(20)/Ta(50)$,

where the AlSiCu serves as sacrificial layer and the first two protective layers have been doubled to prevent erosion from a subsequent chemical etching; the deposition of the substrate has been accompanied by a thin film, namely sample J, which hysteresis loops (in plane parallel and perpendicular to the magnetization vector of the deposition) are presented in Figure 3.15.

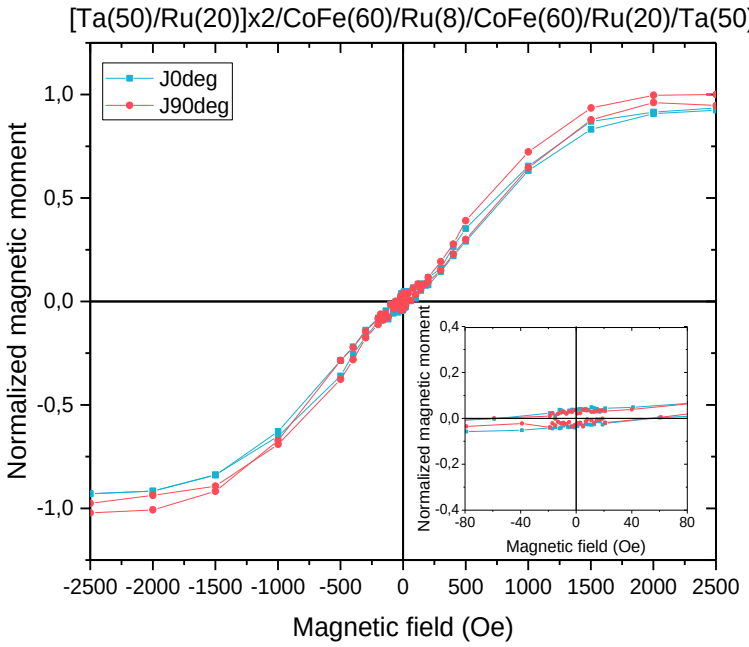

Figure 3.15: In plane parallel (0deg) and perpendicular (90deg) hysteresis loops of sample J

The coercivity values for J0deg and J90deg are 55.57 Oe and 56.60 Oe, respectively. The remanences are quite low, being 3.72 % for J0deg and 2.74% for J90deg.

3.1.2.4 MOKE analysis on magnetron sputtered discs

For a more accurate magnetic analysis, a MOKE measurement have been performed on sample SAF_Dots1, as presented in Figure 3.16. It can be observed that, as expected, the structure shows low negligible magnetization when the field is turned off, which is in agreement with the VSM data reported in the previous section.

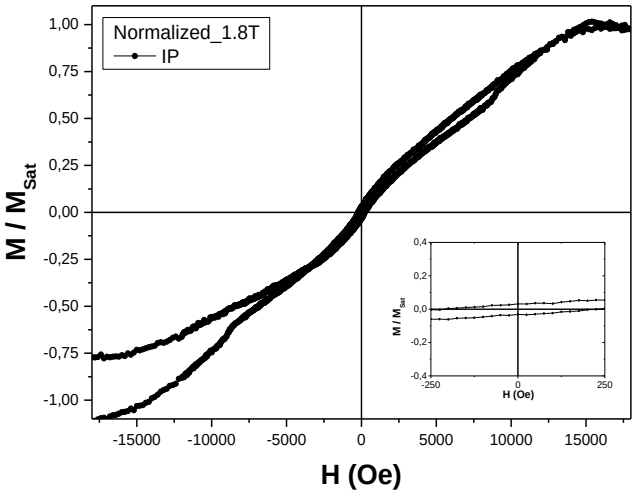

Figure 3.16: MOKE measurement on sample SAF_Dots1

3.2 Nanowires in Porous Anodic Alumina templates

Through a bottom-up route, namely template-assisted electrodeposition in PAA templates, magnetic Au/Fe NMs have been fabricated; The samples have been morphologically characterized by XRD and SEM techniques, while the magnetics properties have been assessed by using superconductive quantum interference device.

3.2.1 Template fabrication by Al anodization

With the techniques described in section 2.1.2.1 Porous Anodic Alumina (PAA) templates have been successfully fabricated. In Figure 3.17 and 3.18 the typical first and second anodization curves are presented, respectively.

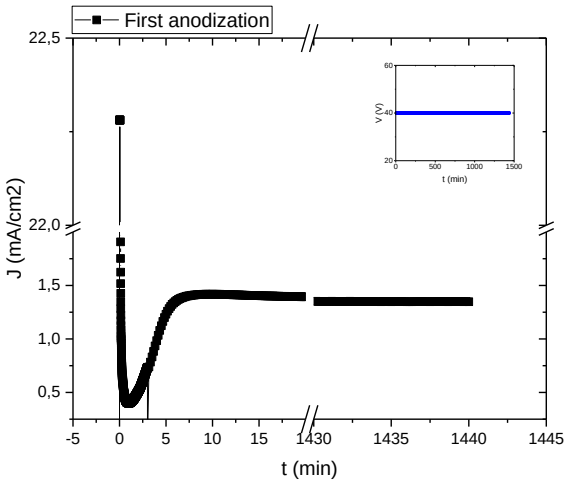

Figure 3.17: First anodization (24h) curves.

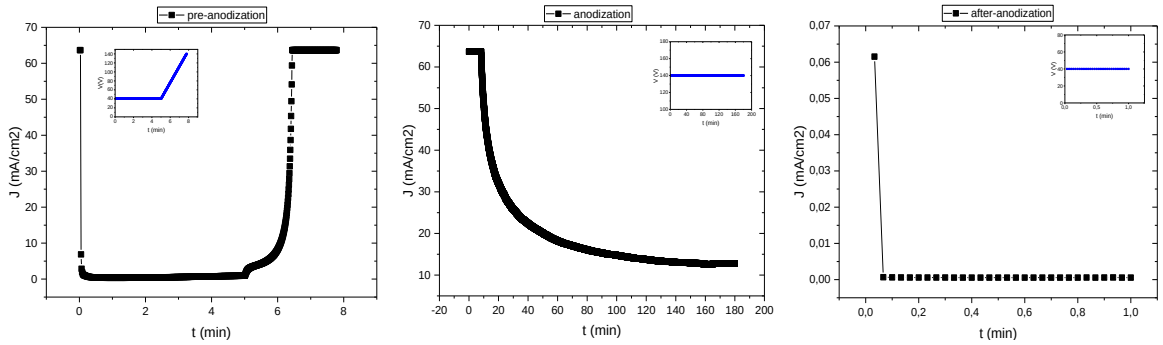

Figure 3.18: Second anodization curves. From left to right: Pre-anodization, anodization and after-anodization.

Figure 3.17 presents the mild anodization performed at 40V for 24 hours. The curve includes the different stages of pore formation; when an anodic voltage is applied, a barrier layer of aluminium oxide forms on the surface of aluminium, which corresponds to the initial current drop. Tiny cracks appear at the oxide/electrolyte interface and they widen to form pores, corresponding to an increase in current density. Further anodization causes the pores to accelerate and attain a constant dissolution speed until an equilibrium between oxide growth and dissolution is reached, represented by the constancy of the current density after a certain point.

The oxide has been then removed, as previously described, leaving a pre-patterned Al surface to facilitate the growth of hexagonally ordered pores in the subsequent anodization step.

Figure 3.18 shows the three stages characteristics of a hard anodization. The pre-anodization is a step that has been performed at 40 V for 5 minutes to create a thin PAA template to suppress breakdown effects caused by the high current densities used in the following step. The hard anodization (step 2) has been done for three hours, in order to obtain templates with thickness around 150 µm. In this stage, the current density is initially saturated, which means that the oxide layer at the bottom of the pores is not proportional to the anodization potential but is thick enough to prevent breakdown. A decrease in current density follows, without reaching any saturation value; this means that the oxide layer is always growing without attaining a constant anodization rate. A minute at 40 V is then performed, to stabilize the barrier layer at the bottom of the pores.

3.2.2 Morphological Characterization

The samples have been characterized by using a SEM and an XRD, to access their morphological and structural properties.

3.2.2.1 Scanning Electron Microscope (SEM)

SEM images of the sample have been acquired after the pore widening and the different electrodepositions. Images of the top and bottom surfaces are shown in Figure 3.19. The small diameter of the pores at the top surface is the result of the performed pre-anodization. Nonopores with approximately 45 nm and interpore distance of 105 nm has been observed, as expected for mild anodization at 40 V [76, 75]. From figure 3.19a it can be clearly seen that the pore widening has not opened all the pores, meaning that a longer time has been needed to be applied in order to exploit the whole template to further electrodeposition processes. After the application of a high voltage (140 V) the neighbouring pores will collapse into each other, resulting in larger pores seen at the bottom of the surface. After the pore widening, the diameters of such pores have been found to be around 130 nm, with interpore distance of 300 nm.

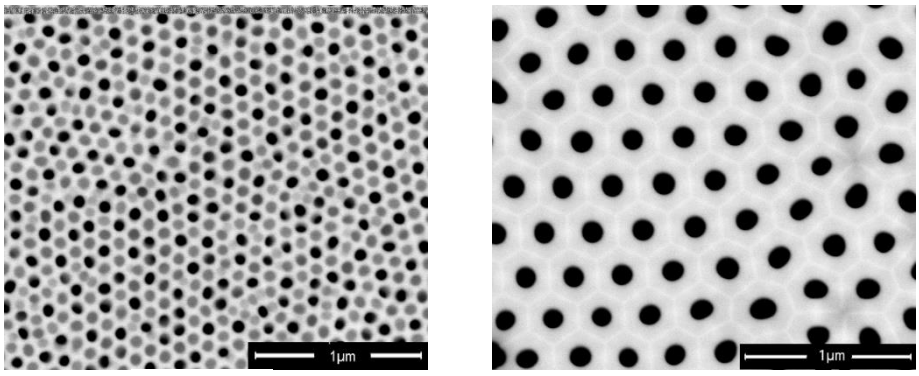

(a) (b)

Figure 3.19: SEM images of the PAA templates after hard anodization with subsequent pore widening. (a) Top surface, (b) bottom surface.

The distribution of the pore diameter is presented in Figure 3.20, with a calculated mean value of 135,2 nm and a standard deviation of 5,63 nm.

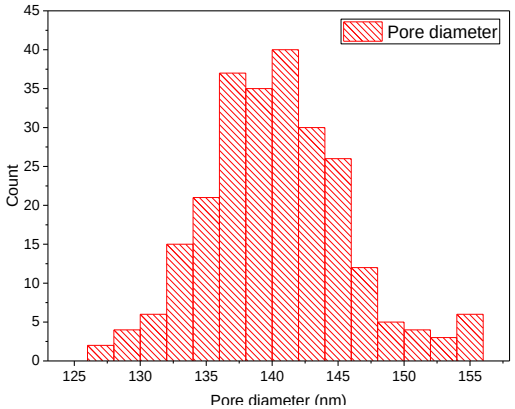

Figure 3.20: Pore diameter distribution.

In the next paragraph, the deposition rates are presented (Figure 3.21). The voltages have been omitted, being 1 V and -1,1 V for the deposition of Au and Fe, respectively. In the next sections, the five layers have been named as Au1, Fe2, Au3, Fe4 and Au5.

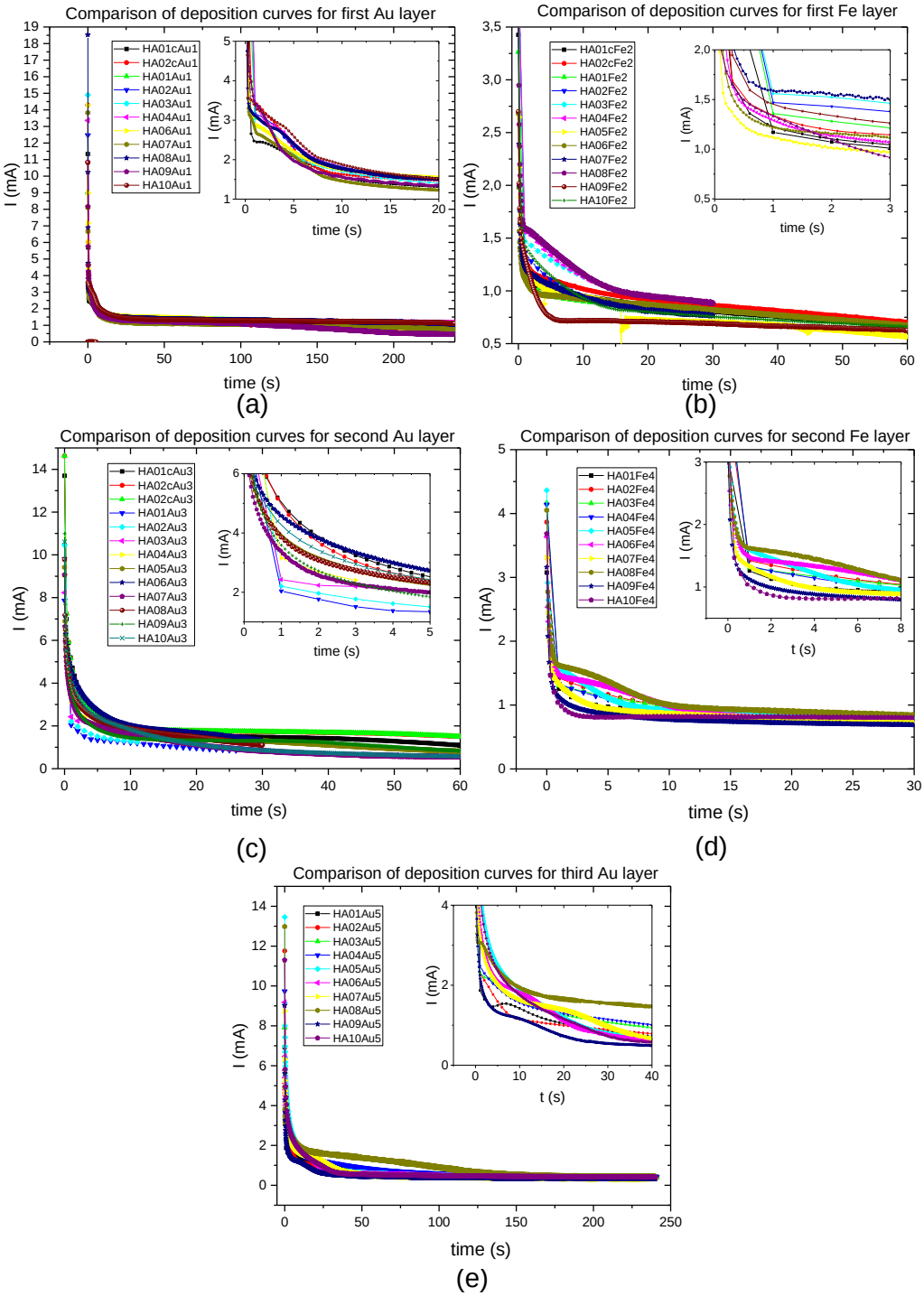

Figure 3.21: Comparison of intensity deposition curves; (a) layer Au1, (b) layer Fe2, (c) layer Au3, (d) layer Fe4, (e) layer Au5.

Samples with different deposition times of Au/Fe have been fabricated, as reported in table 3.7, to explore the smallest thicknesses that can be deposited through electrodeposition technique.

Sample name	$t_{Au}(s)$	$t_{Fe}(s)$	$t_{Au}(s)$	$t_{Fe}(s)$	$t_{Au}(s)$	T_{Fe} (°C)
HA_Calibration1	300	1800	300	-	-	19
HA_Calibration2	300	3600	300	-	-	19
HA_01	240	10	25	10	240	19
HA_02	240	10	10	10	240	19
HA_03	240	10	4	10	240	19
HA_04	240	10	2	10	240	19
HA_05	240	60	60	60	240	19
HA_06	240	60	30	60	240	19
HA_07	240	30	60	30	240	19
HA_08	240	30	30	30	240	19
HA_09/10/11/12(4x)/13(4x)	240	60	60	60	240	10-12

Table 3.7:Electrodeposition parameters.

The first two samples (HA_calibration1,2) have been used to calculate the deposition rates of Au and Fe; The SEM images are reported in figure 3.22 a and 3.22 b respectively, where the brighter parts correspond to Au;

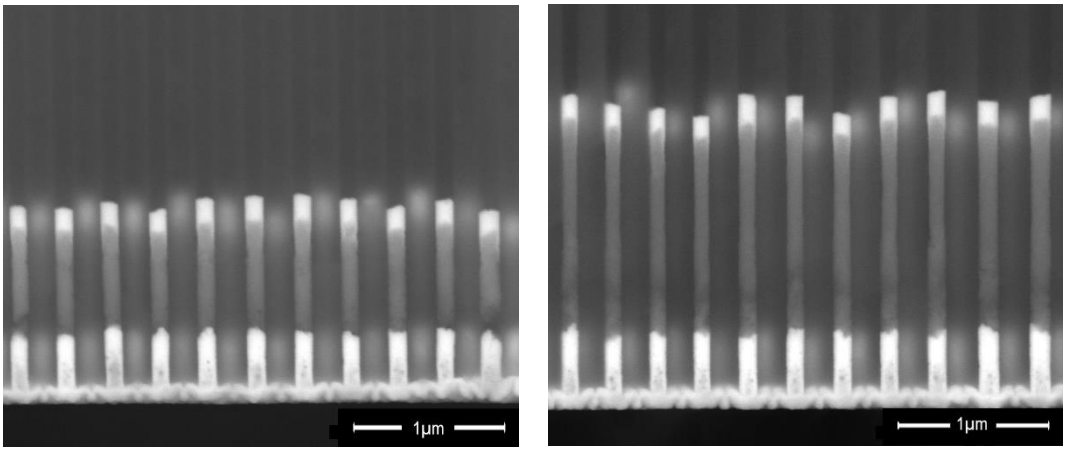

(a) (b)

Figure 3.22: SEM images calibration samples. (a) HA_Calibration01, (b) HA_Calibration02.

With the help of the ImageJ software [84], the deposition rates for Au and Fe have been calculated, giving 0.44193 nm/s and 3.5903, respectively. It is important to notice that the thickness of the first Au layer is different from the top one even if the deposition time is the same. This is because before electrodeposition a thin Au layer has been sputtered on the bottom of the PAA template to be used as electric contact, and the Au

has been penetrated the pores in the template. The Au quality is also different as can be roughly seen from the images, being less dense.

The deposition rates have allowed to have a good estimation of the needed time to achieve the desired layers' thicknesses.

In order to build a synthetic antiferromagnet through electrodeposition technique, the fist approach has been to fix the deposition time of Fe (10 s) to obtain ferromagnetic layers of about 35 nm, and to vary the time of deposition of Au (25 s, 10 s, 4 s, 2 s) to obtain a spacer with thicknesses around 11 nm, 5 nm, 2 nm and 1 nm for the samples HA_01, HA_02, HA_03 and HA_04 respectively. However, what it has been obtained is a mixture of the two materials and no clear layers have been observed, as can be seen in Figure 3.23 for HA_03, for instance. As the resolution of the SEM used is about 5 nm, it has not been expected to be able to clearly distinguish all the layers, but at least a clear interface Au/Fe at the bottom and Fe/Au at the top. For these reasons, the idea to build biocompatible magnetic nanowires has also been adopted, since they are also contrast agents for MRI [1, 2].

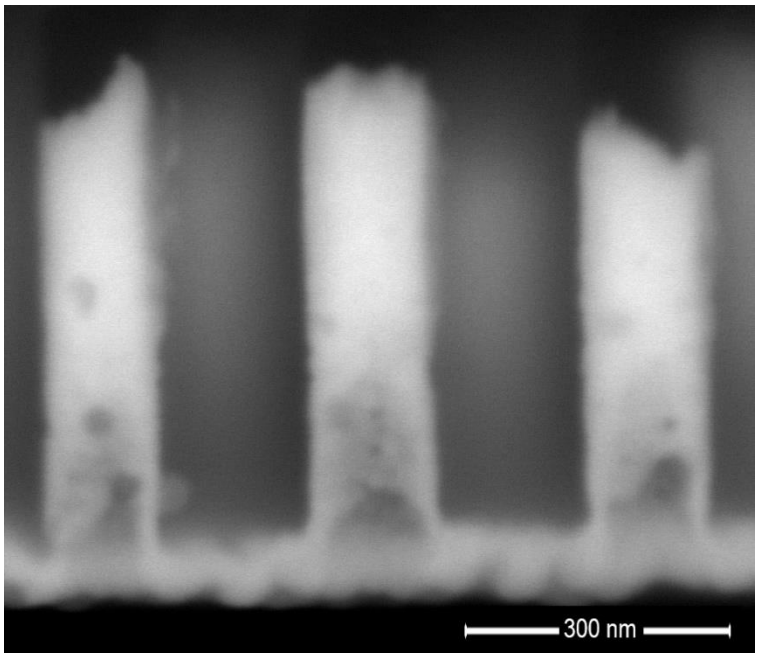

Figure 3.23: SEM image of HA_03.

The next step has been to find the corrects deposition times in order to be able to clearly distinguish the 5 deposited layers.

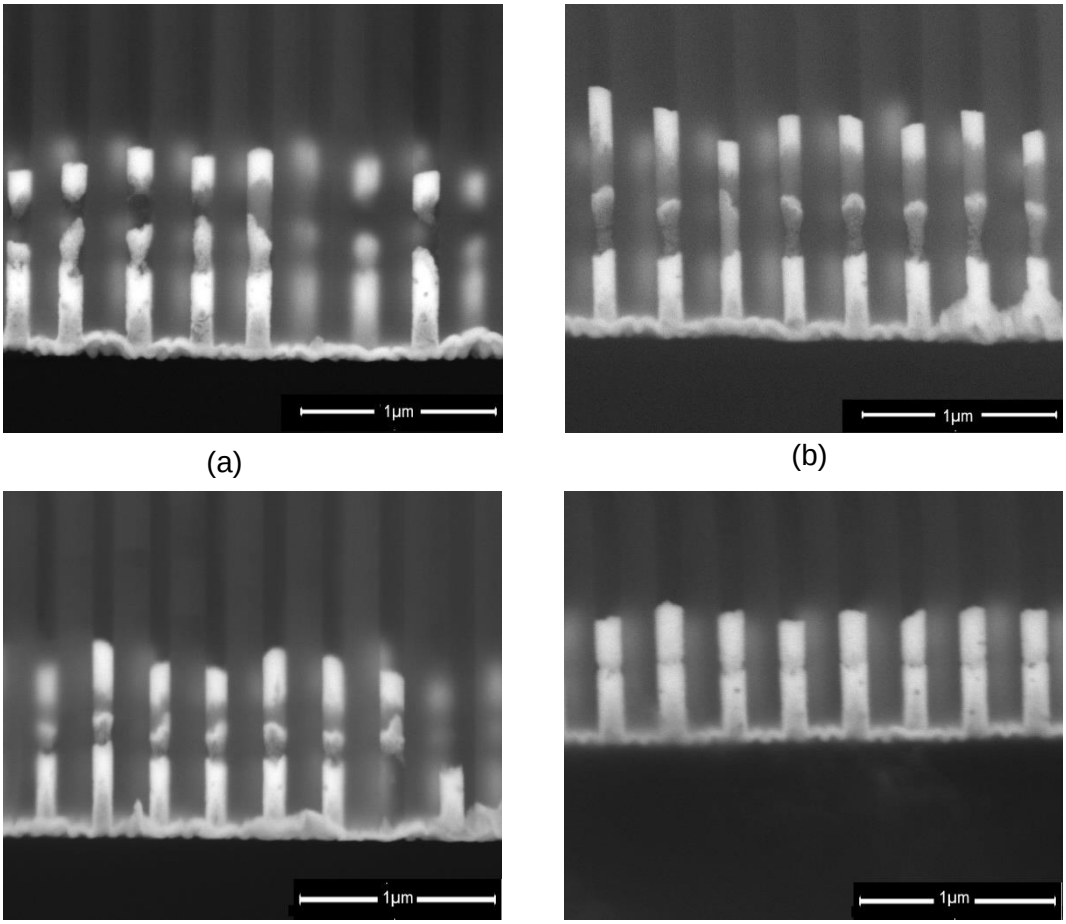

Figure 3.24: SEM images of (a) HA_05, (b) HA_06, (c) HA_07 and (d) HA_08.

Firstly, the Fe deposition time has been fixed to 60 s with Au deposition time at 60 s and then 30 s, samples HA_05 and HA_06, respectively. Secondly, the time of Fe deposition has been halved, setting the Au time, again, at 60 s and 30 s (HA_07 and HA_08). From Figure 3.24, besides in the case of sample HA_08, it can be seen that the 5 different layers are distinguishable, even if not perfectly homogeneous and flats; due to the resolution of the images, not all the segments' length have been able to be calculated accurately as shown in table 3.8, where the predicted lengths from electrodeposition rates are also reported. However, an estimation of the lengths through the deposited mass can be achieved, as presented in the next Table 3.11

To further improve the deposition of Fe, its solution has been kept at a temperature between 10 °C and 12 °C. The result is shown in figure 3.25, where is clear that the cooling down of the solution improves the deposition. From HA_09, all the sample has

been fabricated with the same time of depositions and, in the case of Fe, at a temperature between 10 °C and 12 °C.

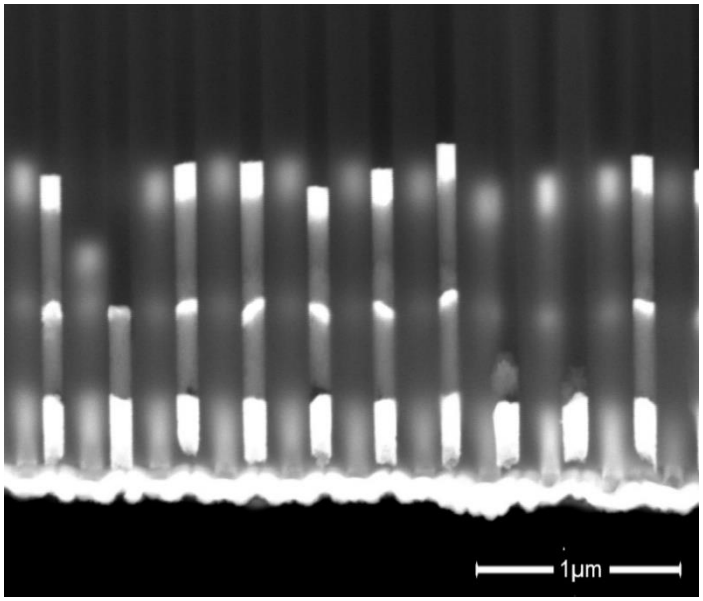

Figure 3.25: SEM image of HA_12.2.

In the first Au layer, the contribution of the sputtering has been taken in account (150nm) and subtracted at the extracted SEM value. Moreover, C1 and C2 stays for HA_Calibration1 and HA_Calibration2, respectively; in addition, the letters HA of the samples have been omitted. Samples HA_10/11/12/13 have not been considered as their values match the ones of HA_09, reported below.

	L_{Au1}(nm)		L_{Fe2}(nm)		L_{Au3}(nm)		L_{Fe4}(nm)		L_{Au5}(nm)		L_{NWs}(μm)	
	S	DR	S	DR	S	DR	S	DR	S	DR	S	DR
C1	130	130	650	650	130	130	-	-	-	-	0.91	0.91
C2	130	130	1300	1300	130	130	-	-	-	-	1.56	1.56
01	-	100	-	35	-	10	-	35	-	100	0.67	0.28
02	-	100	-	35	-	5	-	35	-	100	0.35	0.275
03	-	100	-	35	-	2	-	35	-	100	0.48	0.272
04	-	100	-	35	-	1	-	35	-	100	0.45	0.271
05	-	100	-	200	-	25	-	200	-	100	0.83	0.625
06	180	100	230	200	40	15	175	200	130	100	0.9	0.615
07	70	100	60	100	50	25	60	100	150	100	0.53	0.425
08	-	100	-	100	-	15	-	100	-	100	0.52	0.415
09	220	100	200	200	50	25	220	200	150	100	0.9	0.625

Table 3.8: Segments' lengths extracted from SEM images where possible (S) and calculated through the deposition rates (DR). The total length of the nanowires (NW) is also reported.

With the data extracted from the electrodeposition curves, it has been possible to predict the deposited mass and to determine, as an estimation, the total length of the nanowires.

The total area of the sample is $A = \pi(0.75/2)^2 cm^2$, but the effective area that counts towards electrodeposition depends on the porosity of the sample. With the anodization condition used, the porosity is about 3% [83], which gives and effective area of $A_{eff} = 0.013247\ cm^2$. The total number of nanowires per samples can be then estimated, simply

dividing the effective area with the area of the pore, which gives $\sim 5.62 \times 10^8$ nanowires. The average current density and the total charge have been extracted for each deposited layer, from the electrodeposition curves in Figure 3.20, as shown in table 3.9;

	j_{Au1} $(\frac{mA}{cm^2})$	j_{Fe2} $(\frac{mA}{cm^2})$	j_{Au3} $(\frac{mA}{cm^2})$	j_{Fe4} $(\frac{mA}{cm^2})$	j_{Au5} $(\frac{mA}{cm^2})$	Q_{Au1} (C)	Q_{Fe2} (C)	Q_{Au3} (C)	Q_{Fe4} (C)	Q_{Au5} (C)
C1	0.988	0.401	0.453	-	-	0.311	0.107	0.207	-	-
C2	1.097	0.447	0.433	-	-	0.359	0.189	0.243	-	-
01	1.052	0.953	1.048	0.951	0.394	0.315	0.014	0.038	0.014	0.140
02	1.247	1.065	1.423	1.130	0.473	0.333	0.015	0.027	0.015	0.154
03	1.103	1.243	2.209	1.098	0.548	0.315	0.017	0.019	0.016	0.169
04	1.141	1.297	2.729	1.052	0.596	0.330	0.018	0.017	0.015	0.180
05	1.205	0.650	0.932	0.761	0.453	0.317	0.046	0.087	0.052	0.153
06	0.957	0.788	1.591	0.786	0.391	0.269	0.050	0.064	0.052	0.145
07	0.919	0.823	0.662	0.784	0.338	0.261	0.028	0.065	0.026	0.138
08	1.073	0.946	1.176	0.889	0.435	0.320	0.034	0.056	0.032	0.221
09	0.710	0.661	1.148	0.640	0.267	0.237	0.043	0.083	0.044	0.111

Table 3.9: Current density and charge values for each deposited layer of each sample.

With the use of $\int_0^t Idt = zeN_A \frac{m}{M}$, the deposited mass has been calculated. In this formula, z is the number of valences electrons, e the charge, N_A is the Avogadro number, M the molar mass and m the deposited mass. After the calculation of the deposited mass, the length of the segments and of the nanowires can be estimated, assuming their shape is cylindrical. The results of these calculations are summarized in tables 3.9 and 3.10.

	m_{Au1}(mg)	m_{Fe2}(µg)	m_{Au3}(mg)	m_{Fe4}(µg)	m_{Au5}(mg)
C1	0.635	31.0	0.423	-	-
C2	0.733	54.7	0.496	-	-
01	0.643	4.1	0.077	4.1	0.286
02	0.680	4.3	0.055	4.3	0.314
03	0.643	4.9	0.039	4.6	0.345
04	0.673	5.2	0.035	4.3	0.367
05	0.647	13.3	0.178	15.0	0.312
06	0.550	14.5	0.131	15.0	0.296
07	0.533	8.1	0.133	7.5	0.282
08	0.653	9.8	0.114	9.3	0.451
09	0.484	12.4	0.169	12.7	0.227

Table 3.10: Calculated mass values for each deposited layer of each sample.

	L_{Au1}(µm)	L_{Fe2}(nm)	L_{Au3}(µm)	L_{Fe4}(nm)	L_{Au5}(µm)	L_{NWs}(µm)
C1	24.8	2970	16.5	-	-	44.3
C2	28.7	5240	19.4	-	-	53.3
01	25.1	393	3.0	390	11.2	40.1
02	26.6	412	2.1	410	12.3	41.8
03	25.1	470	1.5	440	13.5	41.0
04	26.3	498	1.4	420	14.3	42.9
05	25.3	1270	6.9	1400	12.2	47.1
06	21.5	1390	5.1	1400	11.6	41.0
07	20.8	777	5.2	719	11.0	38.5
08	25.5	940	4.4	891	17.6	49.3
09	19.0	1190	6.6	1220	8.8	36.8

Table 3.11: Calculated lengths values for each deposited layer of each sample.

The expected lengths, either for Fe and Au, obtained through calculations are clearly higher than the reported ones extrapolated from SEM images and expected from the deposition rates, as shown in Figure 3.26. This means that the electrodeposition process needs to be optimized and proves that this technique is not appropriate to deposit layers under a certain thickness and where nanometric control of the stack is needed.

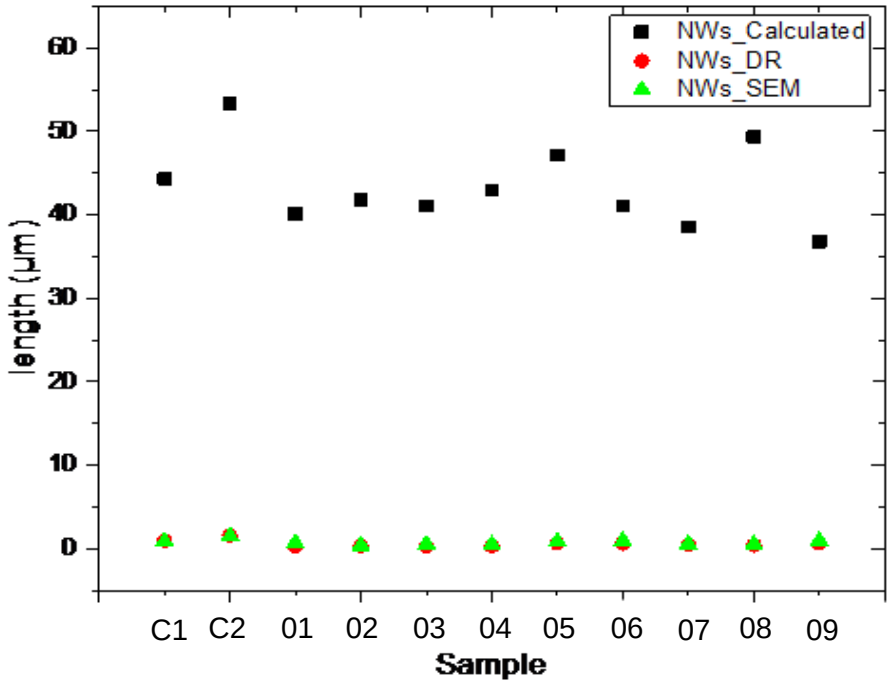

Figure 3.26: Comparison between calculated, extrapolated (SEM) and expected (DR) lengths of NWs.

3.2.2.2 X-Ray Diffraction (XRD)

A $\theta - 2\theta$ X-Ray diffraction analysis has been performed on the samples for a structural characterization. The scan and analysis of a sample, C1 for instance, is presented in Figure 3.27 and confirm the presence of Al, Au and Fe, as well as inferring that the Fe structure is body-centred cubic (BCC) with preferential growth in the (110) direction.

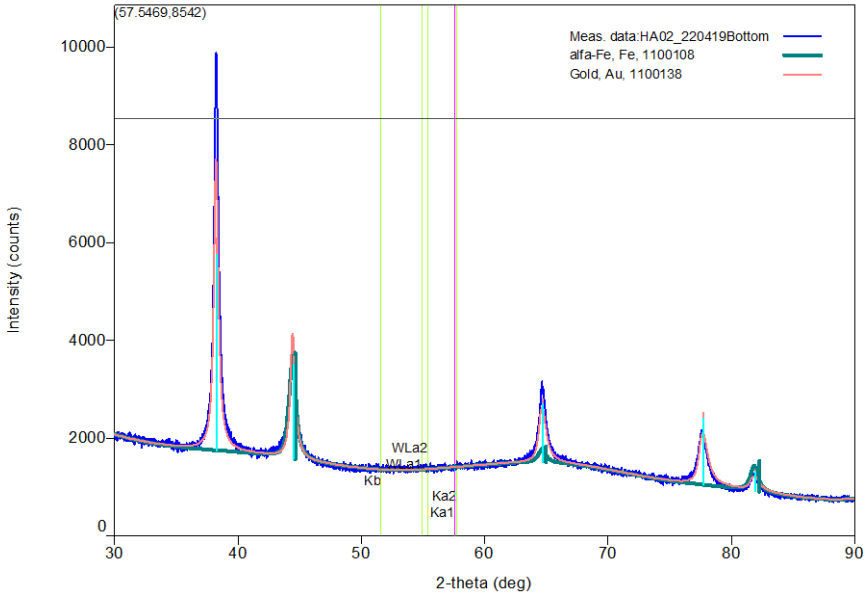

Figure 3.27: X-Ray diffraction analysis of sample C2.

The peaks attributed to Fe are overlapped with those of Au, which hinders the quantitative analysis and makes the determination of the grain size impossible.

3.2.3 Magnetic characterization

To access the magnetic properties of the nanowires, SQUID measurements have been performed, with the direction of the applied field parallel to the surface of the samples.

3.2.3.1 Superconductive Quantum Interference Device (SQUID)

The magnetic properties of these nanowires have been investigated with the use of the Superconductive Quantum Interference Device (SQUID). All the measurements have been acquired with the in-plane configuration and some of them are presented in the images below.

Figure 3.28 presents the comparison between the two samples that have been used as calibrators of the electrodeposition rates (HA_Calibration01 and HA_Calibration02).

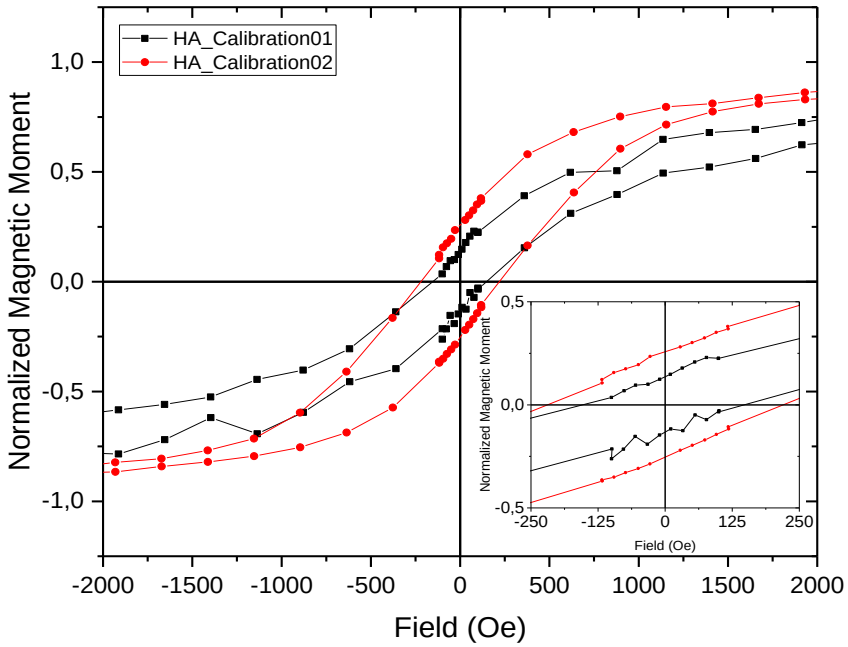

Figure 3.28: In-plane hysteresis loops of samples HA_Calibration1 and HA_Calibration2 (C1 and C2, respectively).

The hysteresis loops show the typical behaviour of a ferromagnet material, as expected due the considerable presence of iron. It can be observed that doubling the thickness of the ferromagnetic material (from C1 to C2) the magnetic moment when no

field is applied also doubles (from 13% to 26%), while the coercivity increases (from 150 Oe to 220 Oe).

To further investigate the changes in remanence and coercivity at lower Fe thicknesses, samples HA_05, HA_06, HA_07 and HA_08 have been compared, as shown in Figure 3.29.

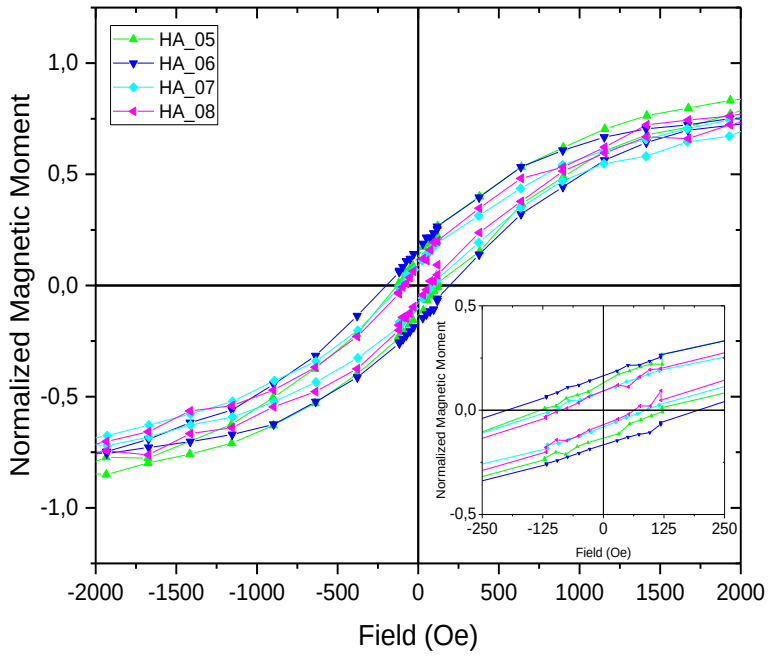

Figure 3.29: In-plane hysteresis loops of samples HA_05, HA_06, HA_07 and HA_08 (05,06,07 and 08, respectively).

From the image above some consideration can be extrapolated; firstly, as expected, samples 05 and 06 show larger values of coercivity and remanence, as the thicknesses of the Fe layers are doubled when compared to those of samples 07 and 08. In particular, it can be seen that the remanence value of sample 05 (13%) is exactly the double of the one of sample 07 (610.5%) and the same happens when comparing the values of sample 06 (17%) and 08 (8.5%), as represented in Figure 3.30 a; this fact can be explained as follows: both pair of samples have the same structure and the halve in remanence is due to the halve in the ferromagnetic layers, as previously observed, with the thickness of the Au layers fixed. Secondly, it can be observed that, for fixed thickness of Fe layers, an increase in the Au3 layer (spacer) lead to a decrease in the coercivity of the sample (Figure 3.30 b). This fact is evident when comparing samples 05/06 and 07/08 where, in both cases, the Au3 layer goes (theoretically) from 25 nm to 15 nm.

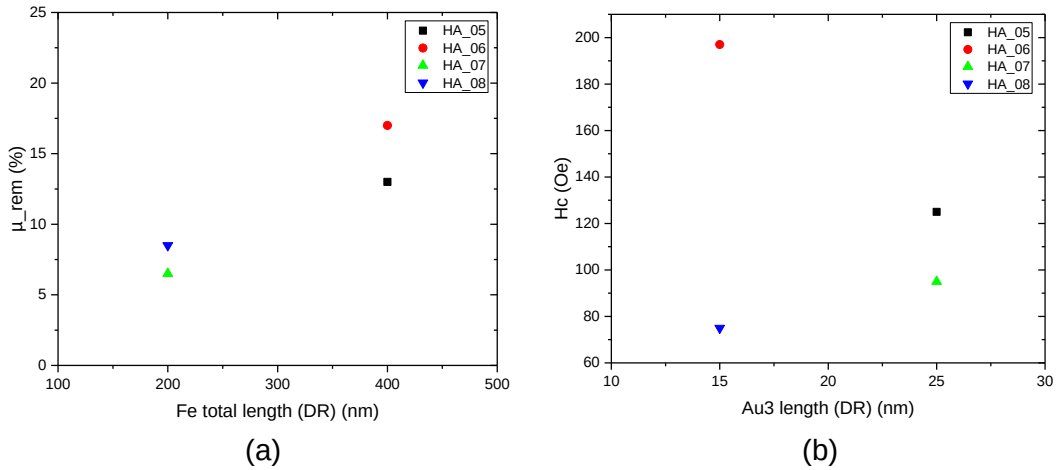

Figure 3.30: Comparison between (a) remanence as a function of total Fe thickness and (b) remanence as a function of Au spacer length of samples HA_05,06,07,08.

It can be concluded that the hysteresis loops, as expected, as strongly dependent on the thickness of the ferromagnetic materials used and are also influenced by the presence of nonmagnetic layers [76, 1].

Chapter 4

Final remarks and future work

The development and comprehension of different magnetic effects is one of the uttermost importance in the pursuit of novel solutions, namely as contrast agents in Magnetic Resonance Imaging. For this purpose, SAFs nanostructures have been fabricated and the antiferromagnetic coupling between ferromagnetic layers and its dependence on different materials, nonmagnetic spacer and buffer layer thicknesses have been studied. On the other side, the characteristics of segmented Au/Fe magnetic nanowires grown by template-assistant electrodeposition in PAA templates have been explored, as these nanostructures can be also be used for contrast enhancement.

Magnetron sputtered stacks (Batch1 and Batch 2) have been magnetically characterized by using a vibrating sample magnetometer (VSM), with the direction of the applied field parallel to the sample's plane and to the induced magnetic moment (acquired during deposition), in order to find the antiferromagnetic peak. The two batches mainly differed on the choice of the ferromagnetic layers (CoFeB and CoFe, respectively); for both batches a Ru nonmagnetic spacer has been used, and its thickness varied in order to achieve the desired magnetic behaviour. A weak antiferromagnetic coupling has been observed for spacer thickness of 4 Å and 8 Å in Batches 1 and 2, respectively.

Because of the need to use biocompatible materials, new stacks have been fabricated (Batch 3,4,5 and 6) by ion beam deposition and magnetically characterized with the help of the VSM. In this ensemble of samples, different combinations of buffer and spacer layers have been explored, while maintaining fixed the thicknesses of Fe ferromagnetic layers; the buffer layer, which is crucial for the chemical stability of the stack and for optimum nucleation of the ferromagnetic layers, has been varied between Ti/Au, Ti and Ru, while the material of the nonmagnetic spacer has been varied between Ti and Au, exploring a wide range thicknesses for each Batch, in order to find the antiferromagnetic coupling between the two iron layers. However, the shapes of hysteresis loops for such samples match the magnetic behaviour of a soft ferromagnet material, characterized by low coercivity values and high remanence field; from an accurate analysis of the curves it has been stated that Ti is not a good candidate to be used as nonmagnetic spacer to antiferromagnetically couple two Fe layers, which is in

agreement with the SAFs reported in literature, while in the case of the Au spacer it has been concluded that the expected antiferromagnetic peaks (1 nm, 2.5 nm), for such Fe thicknesses, have not been observed either because the film has not been epitaxially grown on single-crystal Fe(100) substrate or because the Au material has an intrinsic roughness that propagates along the structure, making the layers nonuniform thus affecting their magnetic interactions.

For the reasons discussed above, magnetron sputtered CoFe discs have been fabricated on a Si substrate previously patterned by interference lithography and fully characterized by SEM, EDS, VSM and MOKE. A layer of AlSiCu has been previously deposited to serve as sacrificial layer to further liberate the nanoparticles from bulk substrate. To release the discs, it has been used a solution of KOH 15% (optimized for Al removal) which in turn has unexpectedly damaged the SAF irreversibly. The chemical etching has still to be optimized, to obtain SAFs dispersed in solution to test cell viability and uptake for subsequent application in the magnetic resonance field. Moreover, new Fe-based stacks should be fabricated by using layer by layer deposition techniques, to have precise control over the layers' growth and ensure samples' uniformity. Such methods are essentials requirements to be able to find the antiferromagnetic coupling between two ferromagnetic iron-layers.

Through a bottom-up route, porous alumina templates have been fabricated by a two-step anodization process to further be electrodeposited to fabricate biocompatible Fe/Au synthetic antiferromagnets. From an early study it has been concluded that such nanoarchiteture, which imposes severe control over the deposition of the layers, could not been fabricated by a bottom-up approach, making this cost-effective technique suitable for the fabrication of segmented nanowires which can be used for the same purpose. The properties of Au/Fe NWs with different lengths have been accessed by using SEM and XRD techniques for the morphological characterization, while a SQUID have been exploited to explore their magnetic properties. It has been concluded that the electrodeposition process still must be optimized and, concerning the magnetic properties, the coercivity and remanence values for such nanostructures is strictly dependent on the thickness of the ferromagnetic layers as well as the length of the nonmagnetic material. It has followed the dissolution of the alumina template in order to disperse the NWs to, in future, further be functionalized and, by flow cytometry technique, test cell viability and cellular uptake with subsequent study on the relaxation time of the transverse magnetization of water protons in presence of such nanoparticles.

BIBLIOGRAPHY

[1] Manuel Banobre-Lopez, Cristina Bran, Carlos Rodriguez-Abreu, Juan Gallo, Manuel Vazquez and Jose Rivas, "A colloidally stable water dispersion of Ni nanowires as an efficient T2-MRI contrast agent," *Journal of Material Chemistry B,* vol. 5, pp. 3338-3347, 2017.

[2] Daniel Shore, Sylvie L. Pailloux, Jinjin Zhang, Thomas Gage, David J. Flannigan, Michael Garwood, Valerie C. Pierre and Bethanie J. H. Stadler, "Electrodeposited Fe and Fe-Au nanowires as MRI contrast agents," *Royal Society of Chemistry,* vol. 52, p. 12634, 2016.

[3] An-Hui Lu, E. L. Salabas, and Ferdi Schuth*, "Magnetic Nanoparticles: Synthesis, Protection, Funcionalization, and Application," *Angewandte Chemie,* vol. 46, pp. 1222-1244, 2007.

[4] Conroy Sun, Jerry S.H. Lee, Miqin Zhang, "Magnetic nanoparticles in MR imaging and drug delivery," *Advance Drug Delivery Reviews,* vol. 60, pp. 1252-1265, 2008.

[5] Vanessa Fernandes Cardoso, António Francesko, Clarisse Ribeiro, Manuel Bañobre-López,Pedro Martins,* and Senentxu Lanceros-Mendez, "Advances in Magnetic Nanoparticles for Biomedical Applications," *Adv. Healthcare Mater.,* vol. 7, p. 1700845, 2008.

[6] T. Vemulkar, R. Mansell, D. C. M. C. Petit, R. P. Cowburn, and M. S. Lesniak, "Highly tunable perpendicularly magnetized synthetic antiferromagnets for biotechnology applications," *Applied Physics Letters,* vol. 107, p. 012403, 2015.

[7] Q. A. Pankhurst, J. Connolly, S. K. Jones and J. Dobson, "Application of magnetic nanoparticles in biomedicine," *J. of Physics D: Applied Physics,* vol. 36, pp. R167-R181, 2003.

[8] Catherine C. Berry and Adam S. G. Curtis, "Functionalisation of magnetic nanoparticles for applications in biomedicine," *Journal of Physics D: Applied Physics,* vol. 36, pp. R198-R206, 2003.

[9] Suphia Parveen, MS, Ranjita Misra, MS, Sanjeeb K. Sahoo, PhD, “Nanoparticles: a boon to drug delivery, therapeutics, diagnostics and imaging,” *Nanomedicine: Nanotechnology, Biology, and Medicine,* vol. 8, pp. 147-166, 2012.

[10] Chenjie Xu, Shouheng Sun, “New forms of superparamagnetic nanoparticles for biomedical applications,” *Advanced Drug Delivery Reviews,* vol. 65, pp. 732-743, 2013.

[11] Yu Gao, Yi Liu and Chenjie Xu, “Magnetic Nanoparticles for Biomedical Applications: From Diagnosis to Treatment to Regeneration,” em *Engineering in Translational Medicine*.

[12] L. Peixoto, R. Magalhães, D. Navas, S. Moraes, C. Redondo, R. Morales, J. P. Araújo, and C. T. Sousa, “Vortex state: Review”.

[13] Ruben Van Roosbroeck, Willem Van Roy, Tim Stakenborg, Jesse Trekker, Antoine D'Hollander, Tom Dresselaers, Uwe Himmelreich, Jeroen Lammertyn, and Liesbet Lagae, “Synthetic Antiferromagnetic Nanoparticles as Potential Contrast Agents in MRI,” *American Chemical Society,* vol. 8, pp. 2269-2278, 2014.

[14] Jinwoo Cheon and Jae-Hyun Lee, “Synergically Integrated Nanopartciles as Multimodal Probes for Nanobiotechnology,” *Accounts of chemical research ,* vol. 41, pp. 1630-1640, 2008.

[15] Jae-Hyun Lee, Ji-wook Kim, and Jinwoo Cheon, “Magnetic Nanoparticles for Multi-Imaging and Drug delivery,” *Molecules and Cells,* vol. 35, pp. 274-284, 2013.

[16] Edina C. Wang and Andrew Z. Wang, “Nanoparticles and their applications in cells and molecular biology,” *Integrative Biology,* vol. 6, pp. 9-26, 2014.

[17] T. Iwaki, Y. Kakihara, T. Toda, M. Abdullah, K. Okuyama, J., “Preparation of high coercivity magnetic FePt nanoparticles by liquid process,” *Appl. Phys,* pp. 94, 6807, 2003.

[18] Chenjie Xu and Shouheng Sun, “Monodisperse magnetic nanoparticles for biomedical applications,” *Polymer International,* vol. 56, pp. 821-826, 2007.

[19] R. H. Kodama, “Magnetic nanoparticles,” *Journar of Magnetism and Magnetic Materials,* vol. 200, pp. 359-372, 1999.

[20] M. Respaud, J. M. Broto, H. Rakoto, A. R. Fert, L. Thomas, B. Barbara, M. Verelst, E. Snoeck, P. Lecante, A. Mosset, J. Osuna, T. Ould Ely, C. Amiens and B. Chaudret,

"Surface effects on the magnetic properties of ultrafine cobalt particles," *Physical Review B,* vol. 57, p. 2925, 1998.

[21] Nathaniel L. Rosi, Chad A. Mirkin, "Nanostructures in biodiagnostics," *Chemical Reviews,* vol. 105, pp. 1547-1562, 2005.

[22] Aldo Isaac Martinez-Banderas, Antonio Aires, Francisco J. Teran, Jose Efrain Perez, Jael F. Cadenas, Nouf Alsharif, Timothy Ravasi, Aitziber L. Cortajarena, and Jurgen Kosel, "Functionalized magnetic nanowires for chemica and magneto-mechanical induction of cancer cell death," *Scientific Reports,* vol. 6, p. 35786, 2016.

[23] De Wei Wong, Wei Liang Gan, Ning Liu, and Wen Slang Lew, "Magneto-actuated cell apoptosis by biaxial pulsed magnetic field," *Scientific Reports,* vol. 7, p. 10919, 2017.

[24] Ning Wang, "Review of cellular mechanotransduction," *Journal of Physics D: Applied Physics,* vol. 50, p. 233002, 2017.

[25] Selma Leulmi, Xavier Chauchet, Melissa Mocrette, Guillermo Ortiz, Helene Joisten, Philippe Sabon, Thierry Livache, Yanxia Hou, Marie Carriere, Stephane Lequien and Bernard Dieny, "Triggering the apoptosis of targeted human renal cancer cells by the vibration of anisotropic magnetic particles attached to the cell membrane," *Nanoscale,* vol. 7, p. 15904, 2015.

[26] Rhodri Mansell, Tarun Vemulkar, Dorothee C. M. C. Petit, Yu Cheng, Jason Murphy, Maciej S. Lesniak, and Russel P. Cowburn, "Magnetic particles with perpendicular anisotropy for mechanical cancer cell destruction," *Scientific Reports,* vol. 7, p. 4257, 2017.

[27] Brian D. Plouffe, Shashi K. Murthy, and Laura H. Lewis, "Fundamentals and application of magnetic particles in cell isolation and enrichment: a reviw," *Reports of Progress in Physics,* vol. 78, p. 016601, 2015.

[28] A. Hultgren, M. Tanase, C. S. Chen, G. J. Meyer, and D. H. Reich, "Cell manipulation using magnetic nanowires," *Journal of Applied Physics,* vol. 93, p. 7554, 2003.

[29] Anne Hultgren, Monica Tanase, Christopher S. Chen, and Daniel H. Reich, "High-Yeld Cell Separations Using Magnetic Nanowires," *IEEE Transaction of Magnetics,* vol. 40, p. 2988, 2004.

[30] Yurii P. Ivanov, Ahmed Alfadhel, Mohammed Al Nassar, Jose E. Perez, Manuel Vazquez, Andrey Chuvilin, and Jurgen Kosel, "Tunable magnetic nanowires for biomedical and harsh enviroment applications," *Scientific Reports,* vol. 6, p. 24189, 2016.

[31] Mingliang Zhang, Christopher M. Earhart, Chinchun Ooi, Robert J. Wilson, Mary Tang, and Shan X. Wang, "Functionalization of high moment magnetic nanodisks for cell manipulation and separation," *Nano Research,* vol. 6, pp. 745-751, 2013.

[32] Vadim Kuperman, "Magnetic resonance imaging-physical principles and applications".

[33] H. Shokrollahi, "Contrast agents for MRI," *Materials Science and Engineering ,* vol. C 33, pp. 4485-4497, 2013.

[34] Robert-Jan M. van Geuns, Piotr A. Wielopolski, Hein G. de Bruin, Benno J. Rensing, Peter M. A. van Ooijen, Marc Hulshoff, Matthijs Oudkerk, and Pim J. de Feyter, "Basic Principles of Magnetic Resonance Imaging," *Progress in Cariovascular Diseases,* vol. 42, pp. 149-156, 1999.

[35] Michael Hayden, Pierre-Jean Nacher, "History and physical principles of MRI," em *Magnetic Resonance Imaging Handbook*, 2016.

[36] Zhi-Pei Liang, Paul C. Lauterbur, Principles of Magnetic Resonance Imaging: A Signal Processing Perspective.

[37] Yu-Dong Xiao, Ramchandra Paudel, Jun Liu, Cong Ma, Zi-Shu Zhang and Shun-ke Zhou, "MRI contrast agents: Classification and application (Review)," *International Journal of Molecular Medicine,* vol. 38, pp. 1319-1326, 2016.

[38] J. Ramalho, R. C. Semelka, M. Ramalho, R. H. Nunes, M. AlObaidy, and M. Castillo, "Gadolinium-Base Contrast Agent Accumulation and Toxicity: An Update," *American J. of Neuroradiology,* vol. 37, pp. 1192-1198, 2016.

[39] Mark J. Bailey, Rob van der Weegen, Piper J. Klemm, Suzanne L. Baker, and Brett A. Helms, "Stealth Rare Earth Oxide Nanodiscs for Magnetic Resonance Imaging," *Advanced Healthcare Materials,* vol. 1, pp. 437-442, 2012.

[40] Vincent Jacques, Stephane Dumas, Wei-Chuan SUn, Jeffry S. Troughton, Matthew T. Greenfield and Peter Caravan, "High-Relaxivity Magnetic Resonance Imaging Contrast Agents Part 2," *Investigative Radiology,* vol. 45, pp. 613-624, 2010.

[41] Gurvinder Singh, Birgitte Hjelmeland McDonagh, Sjoerd Hak, Davide Peddis, Sulalit Bandopadhyay, Ioanna Sandvig, Alex Sandvig, and Wilhelm R. Glomm, "Synthesis of gadolinium oxide nanodisks and gadolinium doped iron oxide nanoparticles for MR contrast agents," *J. of Materials Chemistry B,* vol. 5, pp. 418-422, 2017.

[42] Serena A. Corr, Stephen J. Byrne, Renata Tekoriute, Carla J. Meledandri, Dermot F. Brougham, Marina Lynch, Christian Kerskens, Laurence O'Dwyer, and Yurii K. Gun'ko, "Linear Assemblies of Magnetic Nanoparticles as MRI Contrast Agents," *J. of American Chemical Society Communications,* vol. 130, pp. 4214-4215, 2008.

[43] Hyon Bin Na, Jung Hee Lee, Kwangjin An, Yong Il Park, Mihyun Park, In su Lee, Do-Hyun Nam, Sung Tae Kim, Seung-Hoon Kim, Sang-Wook Kim, Keun-Ho Lim, Ki-Soo Kim, Sun-Ok Kim, and Taeghwan Hyeon, "Developement of a T1 Contrast Agent for Magnetic Resonance Imaging Using MnO Nanoparticles," *Angewandte Chemie ,* vol. 119, pp. 5493-5497, 2007.

[44] Herbert R. Neves, Rafael A. Bini, Jeam H. O. Barbosa, Carlos E. G. Salmon, and Laudemire C. Varanda, "Dextran-Coated Antiferromagnetic MnO Nanoparticles for a T1-MRI Contrast Agent with High Colloidal stability," *Particle & Particle Systems Characterization ,* vol. 33, pp. 167-176, 2016.

[45] Yung-Kang Peng, Chien-Liang Liu, Hsieh-Chich Chen, Shang-Wei Chou, Wei-Hsuan Tseng, Yu-Jui Tseng, Chia-Cheng Kang, Jong-Kau Hsiao, and Pi-Tai Chou, "Antiferromagnetic Iron Nanocolloids: A New Generation in Vivo T1 MRI Contrast Agent," *J. of the American Chemical Society,* vol. 135, pp. 18621-18628, 2013.

[46] Quoc Lam Vuong, Pierre Gillis, Yves Gossuin, "Monte Carlo simulation and theory of proton NMR transverse relaxation induced by aggregation of magnetic particles used as MRI contrast agents," *Journal of Magnetic Resonance,* vol. 212, pp. 139-148, 2011.

[47] A.L. Koh, W. Hu, R.J. Wilson, S.X. Wang & R. Sinclair, "Preparation, structural and magnetic characterization of synthetc anti-ferromagnetic nanoparticles," *Philosophical Magazine,* vol. 88, pp. 4225-4241, 2008.

[48] B. D. Cullity, Introduction to Magnetic Materials.

[49] Wei Hu, Robert J. Wilson, AiLeen Koh, Aihua Fu, Anthony Z. Faranesh, Christopher M. Earhart, Sebastian J. Osterfeld, Shu-Jen Han, Liang Xu, Samira Guccione, Robert

Sinclair, and Shan X. Wang, "High-Moment Antiferromagnetic Nanoparticles with Tunable Magnetic Properties," *Advanced Materials,* vol. 20, pp. 1479-1483, 2008.

[50] Wei Hu, Robert J. Wilson, Christopher M. Earhart, Ai Leen Koh, Robert Sinclair, and Shan X. Wang, "Synthetic antiferromagnetic nanoparticles with tunable susceptibilities," *Applied Physics ,* vol. 105, p. 07B508, 2009.

[51] P. Bruno, "Theory of interlayer exchange interactions in magnetic multilayers," *J. of Physics: Condensed Matter,* vol. 11, p. 9403, 1999.

[52] P. Bruno and C. Chappert, "Oscillatory Coupling between Ferromagnetic Layers Separated by a Nonmagnetic Metal Spacer," *Physical Review Letters,* vol. 67, p. 2592, 1991.

[53] T. Courcier, H. Joisten, P. Sabon, S. Leulmi, T. Dietsch, J. Faure-Vincent, S. Auffret, and B. Dieny, "Tumbling motion yelding fast displacements of synthetic antiferromagnetic nanoparticles for biological applications," *Applied Physics Letters,* vol. 99, p. 093107, 2011.

[54] S. Leulmi, H. Joisten, T. Dietsch, C. Iss, M. Morcrette, S. Auffret, P. Sabon and B. Dieny, "Comparison of dispertion and actuation properties of vortex and synthetic antiferromagnetic particles for biotechnological applications," *Applied Physics Letters,* vol. 103, p. 132412, 2013.

[55] B. Dieny, J. P. Gavigan, and J. P. Rebouillat, "Magnetisation processes, hysteresis and finite-size effects in model multilayer systems of cubic or uniaxial anisotropy with antiferromagnetic coupling between adjacent ferromagnetic layers," *J. of Physics: Condensed Matter,* vol. 2, pp. 159-185, 1990.

[56] Michael Forrester and Feodor Kusmartsev, "The nano-mechanics and magnetic properties of high moment synthetic antiferromagnetic particles," *Physica Status Solidi,* vol. 211, pp. 884-889, 2014.

[57] S. S. P. Parkin, N. More, and K.P. Roche, "Oscillations in exchange coupling and magnetoresistance in metallic superlattice structures: Co/Ru, Co/Cr, and Fe/Cr," *Physical Review Letters,* vol. 64, p. 2304, 1989.

[58] B. Dieny, and J. P. Gavigan, "Minimum energy versus metastable magnetisation processes in antiferromagnetically coupled ferromagnetic multilayers," *J. of Physics: Condensed Matter,* vol. 2, p. 187, 1990.

[59] P. Bruno and C. Chappert, “Ruderman-Kittel theory of oscillatory interlayer exchange coupling,” *Physical Reviw B,* vol. 46, pp. 261-270, 1992.

[60] Nhiem Tran and Thomas J. Webster, “Magnetic nanoparticles: biomedical applications and challenges,” *J. of Materials Chemistry,* vol. 20, pp. 8760-8767, 2010.

[61] H. Joisten, T. Courcier, P. Balint, P. Sabon, J. Faure-Vincent, S. Auffret and B. Dieny, “Self-polarization phenomenon and control of dispersion of synthetic antiferromagnetic nanoparticles for biological applications,” *Applied Physics Letters,* vol. 97, p. 253112, 2010.

[62] Raluca M. Fratila, Sara Rivera-Fernandez and Jeus M. de la Fuente, “Shape matters: synthesis and biomedical applications of high aspect ratio magnetic nanomaterials,” *Nanoscale,* vol. 7, p. 8233, 2015.

[63] Elvin Blanco, Haifa Shen & Mauro Ferrari, “Principles of nanoparticles design for overcoming biological barriers to drug delivery,” *Nature Biotechnology,* vol. 33, pp. 941-951, 2015.

[64] Robert M. Metzger, Valery V. Konovalov, Ming Sun, Tao Xu, Giovanni Zangari, Bin Xu, Mourad Benakli, and W. D. Doyle, “Magnetic nanowires in Hexagonally Ordered Pores of Alumina,” *IEEE Transactions on Magnetics ,* vol. 36, pp. 30-35, 2000.

[65] C. T. Sousa, D. C. Leitao, M. P. Proenca, J. Ventura, A. M. Pereira, and J. P. Araujo, “Nanoporous alumina as templates for multifunctional applications,” *Applied Physics Reviews,* vol. 1, p. 031102, 2014.

[66] E. C. Stoner, F. R. S and E. P. Wohlfarth, A mechanism of magnetic hysteresis in heterogeneous alloys.

[67] E. H. Frei, S. Shtrikman, and D. Treves, “Critical Size and Nucleation Field of Ideal Ferromagnetic Particles,” *Physical Review,* vol. 106, p. 446, 1957.

[68] Anthony S. Arrott, Bretislav Heinrich, and Amikan Aharoni, “Point Singularities and Magnetization Reversal in Ideally soft Ferromagnetic Cylinders,” *IEEE Transaction on Magnetics,* vol. 15, p. 1228, 1979.

[69] G. J. Strijkers, J. H. J. Dalderop, M. A. A. Broeksteeg, H. J. M. Swagten, “Structure and magnetization of arrays of electrodeposited Co wires in anodic alumina,” *Journal of Applied Physics ,* vol. 86, p. 5141, 1999.

[70] R. Ferre and K. Ounadjela, J. M. George, L. Piraux and S. Dubois, "Magnetization processes in nickel and cobalt electrodeposited nanowires," *Physical Review B,* vol. 56, pp. 14066-14075, 1997.

[71] S. Pignard, G. Goglio, A. Radulescu, L. Piraux, S. Dubois, A. Declemy, and J. L. Duvail, "Study of the magnetization reversal in individual nickel nanowires," *Journal of Applied Physics,* vol. 87, p. 824, 2000.

[72] K. Nielsch, R. B. Wehrspohn, J. Barthel, J. Kirscher. U. Gosele, S. F. Fischer, and H. Kronmuller, "Hexagonally ordered 100nm periodic nickel nanowire arrays," *Applied Physics Letter,* vol. 79, p. 1360, 2001.

[73] Louis-Philippe Carignan, Mathieu Massicotte, Christophe Caloz, Arthur Yelon, and David Menard, "Magnetization Reversal in Arrays of Ni Nanowires With DIfferent Diameters," *IEEE Transactions on Magnetics,* vol. 45, pp. 4070-4073, 2009.

[74] Louis-Philippe Carignan, Christian Lacroix, Alexandre Ouimet, Mariana Ciureanu, Arthur Yelon, and David Menard, "Magnetic anisotropy in arrays of Ni, CoFeB, and Ni/Cu nanowires," *Journal of Applied Physics,* vol. 102, p. 023905, 2007.

[75] Suellen Moraes, David Navas, Fanny Beron, Mariana P. Proenca, Kleber R. Pirota, Celia T. Sousa and J. P. Araujo, "The Role of Cu Length on the Magnetic Behaviour of Fe/Cu Multi-Segmented Nanowires," *Nanomaterials,* vol. 8, p. 490, 2018.

[76] M. Susano, M. P. Proenca, S. Moraes, C. T. Sousa and J. P. Araujo, "Tuning the magnetic properties of multisegmented Ni/Cu electrodeposited nanowires with controllable Ni lengths," *Nanotechnology,* vol. 27, p. 335301, 2016.

[77] Semanti Pal, Susmita Saha, Debanjan Polley, Anjan Barman, "Magnetization reversal dynamics in Co nanowires with competing magnetic anisotropies," *Solid State Communications,* vol. 151, pp. 1994-1998, 2011.

[78] X. F. Qin, C. H. Deng, Y. Liu, X. J. Meng, J. Q. Zhang, F. Wang, and X. H. Xu, "Magnetization Reversal of High Aspect Ratio Iron Nanowires Grown by Electrodeposition," *IEEE Transactions on magnetics,* vol. 48, pp. 3137-3139, 2012.

[79] W. Wernsdorfer, B. Doudin, D. Mailly, K. Hasselbach, A. Benoit, J. Meier, J.-Ph. Ansermet and B. Barbara, "Nucleation of Magnetization Reversal in Individual Nanosized Nickel Wires," *Physical Review Letters,* vol. 77, pp. 1873-1876, 1996.

[80] Woo Lee, “The Anodization of Aluminium for Nanotechnology Applications,” *J. of the Minerals, Metals & Materials Society,* vol. 62, pp. 57-63, 2010.

[81] Sachiko Ono, Makiko Saito, Hidetaka Asoh, “Self-ordering of anodic porous alumina formed in organic acid electrolytes,” *Electrochimica Acta,* vol. 51, pp. 827-833, 2005.

[82] Feiyue Li, Lan Zhang, and Robert M. Metzger, “On the Growth of Highly Ordered Pores in Anodized Aluminium Oxide,” *Chemistry of Materials,* vol. 10, pp. 2470-2480, 1998.

[83] Woo Lee, Ran Ji, Ulrich Gosele and Kornelius Nielsch, “Fast fabrication of long-range ordered porous alumina membranes by hard anodization,” *Nature Materials,* vol. 5, pp. 741-747, 2006.

[84] Curtis T. Rueden, Johannes Schindelin, Mark C. Hiner, Barry E. DeZonia, Alison E. Walter, Ellen T. Arena, and Kevin W. Eliceiri, “ImageJ2: ImageJ for the next generation of scientific image data,” *BMC Bioinformatics,* vol. 18, p. 529, 2017.

[85] R. Lavrijsen, A. Fernandez-Pacheco, D. Petit, R. Mansell, J.H. Lee, and R.P. Cowbum, “Tuning the interlayer exchange coupling between single perpendicularly magnetized CoFeB layers,” *Applied Physics Letters,* vol. 100, p. 052411, 2012.

[86] Adel Bendjerad, Sebti Boukhtache, Abdelhamid Benhaya, Dominique Luneau, Seddik El Hak Abaidia, Kaddour Benyahia, “Modeling of Magnetic Properties of Iron Thin Films Deposited by RD Magnetron Sputtering using Preisach Model,” *Serbial Journal of Electrical Engineering,* vol. 13, pp. 229-238, 2016.

[87] P. Bruno, “Interlayer Exchange Interations in Magnetic Multilayers,” em *Magnetism: Molecules to Materials III Nanosized Magnetic Materials*.

[88] J. Unguris, R. J. Celotta, and D. T. Pierce, “Oscillatory exchange coupling in Fe/Au/Fe(100),” *Journal of Applied Physics,* vol. 75, p. 6437, 1994.

[89] S. R. J. Brueck, “Optical and interferometric lithography-nanotechnology enablers,” *Proceedings of the IEEE,* vol. 93, pp. 1704-1721, 2005.

[90] L. Z. W. J. S. Grzegorz D. Sulka, “Anodic Porous Alumina as a Template for Nanofabrication,” *Encyclopedia of Nanoscience and Nanotechnology,* vol. 11, pp. 261-329, 2016.